Zinc Aerosol Hydrolysis in a Transverse Jet Reactor

A Dissertation Submitted to the Faculty of the Graduate School

of the University of Minnesota By

Julia Frances Haltiwanger

In Partial Fulfillment of the Requirements for the Degree of

Doctor of Philosophy

Dr. Jane H. Davidson, Adviser

December, 2011

Acknowledgments

I would like to thank my adviser, Prof. Jane Davidson, whose insight, guidance, and feedback have been instrumental in all that I have done. I will always be grateful to her, and I expect that I will always aspire to be more like her: as a teacher, scholar, speaker, and writer.

I am also grateful to numerous other faculty across the University for their council, including Professors Peter McMurry and Sean Garrick in Mechanical Engineering and Professor Elizabeth Wilson at the Humphrey Institute of Public Affairs. For their advice and guidance on quantitative XRD analysis, I thank R. Curtis Haltiwanger at Cephalon in West Chester, PA; Jeffrey Nicolich at W. R. Grace in Cambridge, MA; and Dr. Maria Torija formerly at the University of Minnesota.

I would like to thank my fellow students in the Solar Lab, particularly Josh Quinell, Luke Venstrom, and Brandon Hathaway for stimulating discussions, helpful advice, and, most of all, their friendship and humor.

I worked on this project while funded by a National Science Foundation Graduate Research Fellowship, an Interdisciplinary Doctoral Fellowship through the University of Minnesota's Institute on the Environment, and a Doctoral Dissertation Fellowship through the University of Minnesota's Graduate School. The work was also funded by the University of Minnesota Initiative for Renewable Energy and the Environment. The XRD and SEM analyses were conducted in the Institute of Technology Characterization Facility, University of Minnesota, which receives partial support from NSF.

I am very grateful to my parents for their confidence in me and their support since day one. And finally, I thank my partner, Anne Gadwa Nicodemus, whose love, patience, and encouragement has been inexhaustible.

Abstract

Some of the major challenges—both technical and economic—of the Zn/ZnO two-step thermochemical hydrogen production cycle are investigated in this study. Technically, complete hydrolysis of Zn in the hydrogen production step remains a major barrier to implementation, and much attention has been given to Zn nano-scale reacting aerosols as a solution. Smaller particles favor faster reaction kinetics, and because they can be entrained and reacted in a gas flow, a continuous controllable process is possible. However, success of this continuous process depends on achieving high particle yields and high conversions in the aerosol, neither of which have yet been achieved in laboratory reactors.

The ability of a new reactor concept based on transverse jet fluid dynamics to control the flow field and rapidly cool the Zn vapor is investigated. In the transverse jet reactor, evaporated Zn entrained in an Ar carrier gas issues vertically into the horizontal tubular reactor through which cooler H_2O and Ar flow. Particles are formed in the presence of steam at $\sim 450\,K$. The objective of controlling the flow field is to keep Zn away from the walls, thereby reducing particle deposition in the reactor and increasing particle yields on the filter. A computational fluid dynamics (CFD) model indicates that the trajectory of the jet can be controlled so that the majority of the Zn mass is directed down the center of the reactor, not near the reactor walls. Furthermore, the model shows that quench rates of $2 \times 10^4\,K/s$ are achieved and reactants are well mixed. Experimentally, maximum particle yields of 93% of the mass entering the reactor are obtained.

Hydrolysis experiments are conducted in the transverse jet reactor at $418\,K$, $573\,K$, $603\,K$, and $713\,K$ to assess the mechanisms of particle growth and hydrolysis. Experiments are conducted with and without steam to assess the effect of the reacting gas on particle morphology. SEM images of particles collected on a filter downstream from the reaction zone indicate that particle growth is dominated by condensation, resulting in hexagonal particles generally with lengths across their hexagonal face of $300\,nm$ to $1\,\mu m$ in experiments with stream, and 1 to $3\,\mu m$ in experiments without steam. Furthermore, the SEM images indicate that in hydrolysis experiments, ZnO forms on the surface of particles early on, protecting them from re-evaporation.

Particle yield on the filter, Y, is defined as the fraction of the total mass entering

the reactor that is collected on a filter placed downstream of the reaction zone. Overall conversion, X, is measured by monitoring the H_2 content of the effluent gas throughout experiments with a gas chromatograph. Conversion of aerosol particles, Z, is the ZnO content (by mole) of particles collected from the downstream filter; it is measured by x-ray diffractometry with the internal standard calibration method. At all temperatures, particle yield remains high—generally 70 to 80% in hydrolysis experiments—and particle deposition on the walls of the reaction zone is eliminated for temperatures of $573\,K$ and above. However, the conversion in the aerosol is $< 7\%$ and decreases with reaction zone temperature. The overall conversion ranges from 11% at $418\,K$ to 49% at $713\,K$. The higher overall conversion than conversion in the aerosol is attributed to heterogeneous Zn vapor hydrolysis. Visual observation proves heterogeneous hydrolysis occurs on the reactor walls; it is inferred that the heterogeneous Zn vapor reaction also occurs on the surface of aerosol particles. In this study, high particle yields are achieved for the first time—an important step forward for the continuous aerosol process. However, complete conversion of the aerosol particles remains a major challenge.

In an economic and policy study of the Zn/ZnO cycle, the time frame for economic viability is assessed through the use of experience curves under minimal input, mid-range, and aggressive incentive policy scenarios. For the technology to become cost competitive, incentive policies that lead to early implementation of solar hydrogen plants will be necessary to allow the experience effect to draw down the price. Under such policies, a learning curve analysis suggests that hydrogen produced via the Zn/ZnO cycle could become economically viable between 2032 and 2069, depending on how aggressively the policies encourage the emerging technology. Thus, if the technical challenges are resolved, the Zn/ZnO cycle has the potential to be economically viable by mid-century if incentive policies—such as direct financial support, purchase guarantees, low interest rate loans, and tax breaks—are used to support initial projects.

Contents

List of Tables

List of Figures

Nomenclature

Roman Letters

a	radius of particle $[nm]$
$A_\circ$	pre-exponential factor in the Arrhenius expression $\left[\frac{mol}{cm^2 \cdot s}\right]$ or $\left[\frac{mol}{cm \cdot s}\right]$
A_{Zn}, A_{ZnO}	area of XRD Zn and ZnO peaks
C	concentration of the diffusing reactant in the shrinking core model $[/cm^3]$
D	reactor diameter $[mm]$
d	diameter
d^*	critical diameter for particle nucleation $[nm]$
D_e	diffusion coefficient for Zn diffusion through the ZnO shell
E_A	activation energy in the Arrhenius expression $\left[\frac{kJ}{mol}\right]$
G	Gibb's energy $\left[\frac{kJ}{mol}\right]$
H	enthalpy $\left[\frac{kJ}{mol}\right]$
k	reaction rate constant $\left[\frac{mol}{cm^2 \cdot s}\right]$ or $\left[\frac{mol}{cm \cdot s}\right]$
M	molar mass $\left[\frac{g}{mol}\right]$
m	mass $[g]$
mf	mass fraction
N	aerosol concentration $/cm^3$
n	number of moles $[mol]$
P	pressure
q	volumetric flow rate $\left[\frac{L}{min}\right]$ or $\left[\frac{cm^3}{min}\right]$
R	universal gas constant $\left[\frac{L \cdot atm}{K \cdot mol}\right]$
R	effective velocity ratio for a transverse jet

r reaction rate $\left[\frac{mol}{cm^2 s}\right]$

Re_d Reynolds number

S entropy $\left[\frac{kJ}{mol \cdot K}\right]$

S' saturation ratio

T temperature $[K]$

t time $[s]$ or $[min]$

u velocity

X overall conversion in the reactor

Y particle yield on the filter

y molar fraction

Z conversion in the aerosol

Greek Letters

α fractional conversion of aerosol particles

$\bar{\rho}$ molar density $\left[\frac{mol}{cm^3}\right]$

ρ density

τ residence time of aerosol particles

Subscripts

ave average

cf cross-flow

$core$ unreacted core in a reacting particle

d diffusion limited regime

eq equilibrium state

EZ evaporation zone

$full$ full conversion to ZnO

j jet

p an aerosol particle

PH pre-heat zone

$phase$ phase change

RZ	reaction zone
s	surface reaction regime
sat	saturation
0	initial

Chapter 1

Introduction and Motivation

We are living in an era of rising energy prices, exploding worldwide energy demand, rising temperatures due to increasing greenhouse gas emissions, and wars waged for control of non-renewable energy sources. At the same time, enough solar energy lands on less than 0.2% of the earth's surface to more than meet worldwide energy demands.[1] The challenge, however, is efficiently capturing and storing this abundant resource for use when and where it is needed. One intriguing approach for the efficient harvest and storage of solar energy is the use of high temperature concentrating solar plants to generate fuels such as hydrogen (H_2).

Theoretically, hydrogen can be produced using concentrated sunlight to thermally dissociate water (H_2O). However, the temperatures required to achieve a reasonable degree of dissociation ($> 3500K$) and the lack of effective techniques for avoiding recombination make it impractical. One intriguing approach that splits H_2O using solar energy and sidesteps these difficulties is a two-step Zn/ZnO thermochemical cycle [1, 2]. The first, endothermic step is the thermal dissociation of zinc oxide (ZnO) into zinc (Zn) and oxygen (O_2) ($\Delta_r H = 395 \frac{kJ}{mol}$ at $2340K$):

$$ZnO(s) \longrightarrow Zn(g) + \frac{1}{2}O_2(g). \tag{1.1}$$

This step is carried out in a reactor placed at the focal point of a solar concentrating system.

[1] Based on average daily insolation of $4.2kWh/m^2$, worldwide energy demand of $371MWh/day$, and 10% solar conversion efficiency.

It has been shown to be feasible in prototype reactors [3–6]. In the second, exothermic step, Zn is hydrolyzed with steam to produce ZnO and hydrogen (H_2) ($\Delta_r H = -104\frac{kJ}{mol}$ at $650K$):

$$Zn(s) + H_2O(g) \longrightarrow ZnO(s) + H_2(g) \tag{1.2}$$

This exothermic step can be carried out whether or not the sun is shining, whenever and wherever it is useful. Ideally, the product ZnO can be completely recycled back to the first step, so that the net effect is the splitting of water. Currently, the second step is a major barrier to implementation of the two-step Zn/ZnO cycle, and it is the focus of this study.

The technical challenge in the second step is to overcome the barrier posed by the formation of a ZnO layer on the surface of the Zn, through which the reactants must diffuse [7–11]. This diffusion limited reaction occurs much more slowly than the surface reaction [12, 13]. Much attention has been given to Zn nanoparticles as a solution to this problem. With their high specific surface area, much of the nanoparticle mass is on a surface, where the reaction happens readily. In addition, smaller particles favor faster reaction kinetics [14, 15], and because they can be entrained and reacted in a gas flow, a continuous controllable process is possible.

We currently have a limited understanding of the kinetics governing the hydrolysis of Zn particles in an aerosol. The hydrolysis of Zn particles has been studied thermogravimetrically in the temperature range 603 to $633\,K$ [13], and two reaction regimes were identified: an initial, fast reaction with the surface of the Zn particle, and a much slower, diffusion limited reaction. However, studies of the oxidation of other metal particles in an aerosol have found that kinetics determined via TGA can under predict the reaction in the aerosol by as much as an order of magnitude [16] and that kinetics improve with decreasing particle size [14]. A second avenue for hydrogen production in a reacting Zn aerosol has also been suggested: a low temperature, two stage reaction in the temperature range from 373 to $448\,K$ (Section 2.2.3) [17]. At these temperatures, $70\,nm$ single Zn nanoparticles reacted with H_2O to produce H_2 and $Zn(OH)_2$, as follows:

$$Zn(s) + 2H_2O(g) \rightarrow Zn(OH)_2(s) + H_2(g) \tag{1.3}$$

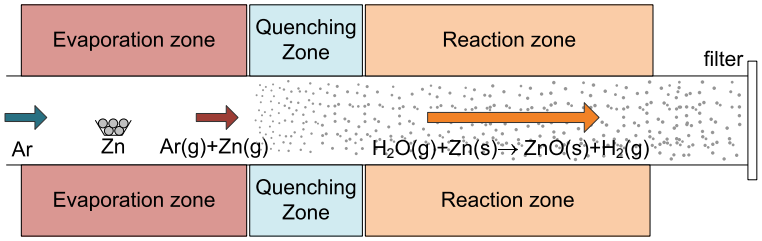

Figure 1.1: General schematic of a Zn nanoparticle and H_2O aerosol reactor.

The $Zn(OH)_2$ was then dissociated into ZnO and H_2O in the temperature range 423 to 523 K, making the net reaction identical to equation 1.2. In addition to hydrolysis of aerosol particles, the reaction can occur by a heterogeneous Zn vapor hydrolysis on solid surfaces, including the surface of aerosol particles [18]. These studies are discussed in more detail in Chapter 2.

Prior work on the Zn/ZnO aerosol process has been focused on using tubular reactors to create Zn particles via evaporation and condensation and react them with H_2O in an Ar carrier flow. Figure 1.1 provides a general schematic of the process. In the evaporation zone of the reactors, Zn is vaporized and entrained in an Ar (or other inert) carrier gas flow, which is then quenched (rapidly cooled). When Zn vapor falls below its saturation temperature, it nucleates and forms nanoparticles, which grow by coagulation and condensation. Coagulation will dominate if particle concentrations are high and Zn vapor concentrations are low, and condensation will dominate if much of the initial Zn vapor does not nucleate during the quenching process. The particles are entrained in the gas flow and they grow and ideally react with H_2O to form ZnO as they travel the length of the reactor.

The studies done to date on the hydrolysis of Zn aerosols [19–25] have failed to achieve high conversions to ZnO in the aerosol. Aerosol particles are collected on a downstream filter and analyzed, ex-situ, for ZnO content by x-ray diffraction (XRD). The ZnO content (by mass) measured in prior reactors ranges from 0% to 35%. As will be discussed later, quantitative XRD analysis is difficult to do accurately, and the traditional peak fitting methods of Rietveld and RIR consistently over-predict the ZnO content in known samples. Thus, the reported values of ZnO content on the filter may actually be over-predictions.

Low conversions to ZnO have disastrous effects on the overall efficiency of the Zn/ZnO thermochemical cycle. Thus, to determine whether the aerosol process is a viable option, we need a greater understanding of the mechanisms for particle growth and hydrolysis that dominates in an aerosol reactor and how that may contribute to low conversions.

Further, in the reactors to date, approximately 80% of the evaporated Zn mass is deposited on the walls of the reactor. If a significant majority of the Zn mass is deposited on the walls of the reactor, the process cannot be considered continuous. High levels of particle deposition on the walls of prior reactors have also hobbled our understanding of the aerosol process—if a majority of the mass (60 to 100%) is not in the aerosol, then conclusions about the aerosol process are necessarily confused by the upstream deposits. For example, if 80% of the Zn mass is deposited on the reactor walls, the size, and thus kinetics, of aerosol particles will be affected by the reduction in aerosol mass. Additionally, significant particle deposits on the wall artificially increase the H_2 production rate, as particles deposited on the wall have an effective residence time of the duration of an experiment, rather than the much shorter residence time of in flight particles. As a result, reported overall conversions (i.e. the total H_2 produced as a fraction of the theoretical maximum H_2 production) in prior studies are high (up to 95%) and not attributable to the aerosol process. All authors are careful to point out that these overall conversions are not due to aerosol reactions and they all attempt to accurately quantify the contribution of the aerosol. Still, high reported overall conversions obscure the hard truth: there is little reason to attempt an aerosol process if it is not continuous, so the rubrics that really matter are conversion in the aerosol and yield on the filter. To date, no set of experimental parameters in any reactor have achieved filter yields over 50% or aerosol conversions over 34%. Furthermore, no single experiment has achieved filter yields *and* aerosol conversions that are both over 25%.

There are three main technical objectives of this study: first, the design and implementation of a reactor that achieves high filter yields without sacrificing quench rates and mixing of the reactants; second, improved conversion in the aerosol; and third, characterizing the evolution of the aerosol as particles grow and react. An understanding of the mechanisms for particle growth and hydrolysis in the aerosol reactor are needed to evaluate the efficacy

of the aerosol hydrolysis process. The second objective, high conversions in the aerosol, is the most difficult to achieve. Prior work has covered a wide range of quench rates (from 400 to $10^6\,K/s$), residence times (0.4 to $7\,s$), and reaction temperatures (573 to $873\,K$), and none have reported ZnO contents of more than 35% (by mass) of particles collected on the filter. Given that the transitional peak-fitting methods for quantitative XRD, RIR and Rietveld, over predict the ZnO content of known samples, actual conversions are likely to be even lower than reported.

The difficulty in achieving high conversions of aerosol particles highlights the importance of the third technical objective: if high aerosol conversions are not attained, an understanding of the mechanisms that dominate particle growth and hydrolysis and result in low conversions is needed. As discussed above, there are three potential mechanisms for H_2 production in the aerosol reactor. At low temperature, a $Zn(OH)_2$ reaction has been observed for single, $70\,nm$ particles. At higher temperatures, Zn particles can react directly with steam in either a fast, surface reaction, or a much slower, diffusion limited reaction. Finally, if some Zn remains in the vapor phase in the aerosol reactor, it could react with steam on the surface of aerosol particles in via heterogeneous Zn vapor hydrolysis. Understanding which mechanism dominates in the aerosol reactor can help explain low conversions.

The prior work illustrates trade-offs between high quench rates, long residence times, yield, and conversion. Past reactors achieve relatively high residence times at the cost of high quench rates (or vice verse), or high overall conversions at the cost of filter yields. This points to apparent contradictions in the design goals for Zn aerosol hydrolysis reactors. A desire for sufficient particle residence times (to achieve complete conversion to ZnO) and the need to reduce or eliminate particle deposition on the walls of the reactor point to low Re_d flows, as turbulence is likely to be at least partially responsible for particle deposition on reactor walls. However, the required rapid quench of the Zn vapor in particle formation and the need to thoroughly mix the reactants point to high Re_d flows. Thus, reactor design is crucial in achieving any of the listed objectives, as the reactor will need to achieve high quench rates and mixing of the reactants in a flow field that avoids particle deposition on the reactor walls.

In addition to the technical objectives of this study, a fourth goal is an evaluation of the economic viability of the Zn/ZnO cycle, and the policy levers needed to make it economically competitive, assuming that all major technical issues are resolved. I will explore the level of carbon taxation necessary to make the cycle competitive with hydrogen production via methane reforming. In addition, the time frame for economic viability is assessed through the use of experience curves under minimal input, mid-range, and aggressive incentive policy scenarios.

A review of related literature appears in Chapter 2. The design of novel aerosol reactor based on the concept of transverse jets is presented in Chapter 3, and a series of experiments and corresponding numerical models used to assess the built reactor appear in Chapter 5. The goal of these experiments is to assess the success of the first technical objective: significant improvements in filter yields while maintaining quench rates of at least $10^4\,K/s$ and achieving well mixed reactants. In Chapter 6, a series of experiments designed to measure the hydrolysis in the transverse jet aerosol reactor and elucidate the mechanisms for growth and the reaction are presented. Experiments are conducted over a range of temperatures to assess the hydrolysis mechanism. First, experiments are conducted at temperatures favorable for the low temperature production of $Zn(OH)_2$. No evidence of such a reaction is found. Second, experiments, are conducted at temperatures that are both well below the melting point of Zn and cool enough that only a small fraction of the overall Zn mass would be in the vapor phase at equilibrium (573 to $603\,K$). Finally, Zn hydrolysis is measured at temperatures above both the melting point of Zn and the saturation temperature ($723\,K$).

Chapter 7 explores the economic viability of the Zn/ZnO cycle and the policy levers needed to make it competitive, assuming that all major technical issues are resolved. The time frame for economic viability is assessed through the use of experience curves under minimal input, mid-range, and aggressive incentive policy scenarios.

Chapter 2

Background

An understanding of the Zn aerosol hydrolysis process is built on a wide range of academic fields. In section 2.1, I review previous studies on the hydrolysis of Zn nanoparticles in an aerosol reactor [19–25]. These studies inform the reactor design in the present work and it is through these studies that the need to reduce particle deposition on reactor walls and gain better understanding of the mechanisms for hydrolysis have become apparent. In section 2.2, I review what is known about the reaction taking place in this process. First, I discuss the thermodynamics of solid Zn hydrolysis and of heterogeneous Zn vapor hydrolysis. Second, I discuss the kinetic studies on the hydrolysis of Zn, focusing on a thermogravimetric analysis (TGA) study of Zn hydrolysis at the nanoscale from $603\,K$ to $633\,K$ [13] (see section 2.2.2). This study determined kinetic expressions for a surface reaction regime and a diffusion limited regime. There is evidence to suggest that the kinetics of particles reacting in an aerosol is different from the kinetics measured using TGA [14–16, 24]. Thus, I also discuss kinetic studies on the oxidation of Zn and other metal nanoparticles in an aerosol [14, 15, 26] in section 2.2.3. These studies indicate that metal nanoparticles react faster in the aerosol than they do in a TGA crucible, and that temperatures above the metal melting point result in increased reaction rates. In section 2.3, I review one study on metal nanoparticle formation in a reacting gas [27], as well as studies on metal nanoparticle formation and growth in a non-reacting gas [28–43].

2.1 Prior Work

Using nanoparticles in the second step of the Zn/ZnO two-step solar thermochemical process has been investigated by several groups [19–25]. The experimental approach is very similar across these papers; key process parameters and results are summarized in Table 2.1. All experiments used tubular reactors to react Zn particles in an Ar gas flow with H_2O. In all but one case [24], the same reactor was used to create the Zn nanoparticles via evaporation and condensation. Funke et al. [24] fed commercial Zn powder into their aerosol reactor. Figure 1.1 provides a general schematic of the process. In the evaporation zone of the reactors, Zn was vaporized at $900 - 1300K$ and entrained in an Ar carrier gas flow. The $Ar/Zn(g)$ mixture was then quenched, either by mixing with a cooler inert gas/steam mixture or by transport through an unheated portion of the reactor. When Zn vapor falls below its saturation temperature, it nucleates and forms nanoparticles. In some reactors, the Zn particles were formed first, and subsequently reacted with steam [21, 24]. In other reactors, the particle formation and hydrolysis occurred simultaneously [19, 20, 23, 25]. In all cases, the goal was Zn particle conversion to ZnO in the aerosol.

At the exit of the reactors, glass fiber filters were used to collect aerosol particles for post-analysis by x-ray diffraction (XRD), and/or electron microscopy. A gas chromatograph (GC) or mass spectrometer was used to measure the H_2 component of the effluent gas in order to determine overall conversion, X:

$$X = \frac{n_{H_2}}{n_{H_2,theoretical}} \tag{2.1}$$

where n_{H_2} is the total number of moles of hydrogen produced during the experiment and $n_{H_2,theoretical}$, the maximum possible H_2 production, is equal to the moles of Zn evaporated, $n_{Zn,0}$. Most studies reported the particle yield on the filter, Y:

$$Y = \frac{m_{Zn/ZnO,filter}}{m_{Zn,0}} \tag{2.2}$$

where $m_{Zn/ZnO}$ is the combined mass of Zn and ZnO on the filter and $m_{Zn,0}$ is the mass of Zn that enters the reactor. The particle yield is the fraction of the evaporated Zn that is collected on the filter. Most studies used XRD measurements of the particles on the filter

Table 2.1: Summary of main parameters and results for previous work in zinc hydrolysis in aerosol reactors.

	Wegner et al. (2006) and Weiss et al. (2005)	Ernst et al. (2006)	Abu Hamed et al. (2007a)	Abu Hamed et al. (2009)	Funke et al. (2008)	Melchior et al. (2009)
T_{evap}[K]	923, 1023, 1073	1263	1023	1023	N/A	$1123 - 1273$
evaporation rate [mol/min]	not reported	7.5×10^{-4}	1.3×10^{-4}	1.3×10^{-4}	Zn feed rate:	$1.4 - 9.5 \times 10^{-4}$
duration [minutes]	$15 - 20$	$60 - 70$	30	$90 - 120$	70	130
quench rate $[K/s]$	not reported	400	1000	1000	N/A	$2 \times 10^4 - 10^6$
T_{RZ} $[K]$	$600 - 1000$	$573 - 873$, $923 - 1273$	$600 - 750$	$630 - 730$	$653 - 813$	$573 - 873$
τ_{avg} $[sec]$	$0.5 - 1.5$	$5 - 7$	0.5	$0.4 - 0.6$	0.6	$0.8 - 7$
y_{H_2O}		25%	6.3%	$21.3 - 29.9\%$	0.5%	$1.6 - 12.9\%$
n_{H_2O}/n_{Zn}	$1.8 - 36$	30	87	348	3.3	$19 - 132$
X	$45 - 70\%$	$60 - 90\%$	$51 - 56\%$	$61 - 79\%$	27%	$60 - 95\%$
Y, Yield on filter	not reported	not reported	$9 - 14\%$	$9 - 12\%$	$10 - 30\%$	$10 - 52\%$
Z, Composition on filter (ZnO % by mass)	0%	$13 - 17\%$	0%	$22 - 34\%$	$5 - 23\%$	$3 - 22\%$

to obtain the composition of the filter particles by weight. The assumption that particles did not continue to react on the filter allowed the groups to take the filter XRD composition results to be indicative of the particle conversion in the aerosol, α. Recent experiments at the University of Minnesota demonstrate that at filter temperatures below $380\,K$, that assumption is valid. At filter temperatures of $465\,K$ and above, particles continue to react at a very slow conversion rate [44]. Thus, in general, the composition of the particles on the filter, Z, can be used to determine the conversion in the aerosol. Z is defined as

$$Z = \frac{n_{ZnO}}{n_{Zn,0}}, \tag{2.3}$$

where n_{ZnO} is the number of moles of ZnO in an aerosol particle or in a collection of aerosol particles, and $n_{Zn,0}$ is the total initial number of moles in the same particle or collection of particles. In some studies, Z is also reported in terms of ZnO content by mass. The aerosol conversion, Z, differs from the overall conversion, X; X accounts for all H_2 produced, while Z refers only to the conversion in the aerosol. As will be discussed later, quantitative XRD analysis is difficult to do accurately, and the traditional peak fitting methods of Rietveld and RIR consistently over-predict the ZnO content in a sample. Thus, the reported ZnO concentrations on the filter may actually be over-predictions.

These previous studies have reported overall conversions of up to 95%. However, most of the hydrogen produced in past reactors is due to the hydrolysis of particles deposited on the reactor walls over the course of the experiment. In the reactors to date, 50 to 91% of the evaporated Zn mass was deposited on the walls of the reactor. These particles sit in the reactor at elevated temperatures for the duration of the experiment—experimental duration therefore becomes an important determinant of the overall conversion, X. The particles deposited on the walls in the hottest part of the reactor are generally completely converted to ZnO. Farther downstream in the reactors, the temperatures are cooler, and the extent of conversion of the deposited particles decreases accordingly. However, the main benefit of the aerosol process is that it can be continuous, so the real measures of success are conversion in the aerosol, Z, and yield, Y. The ZnO content (by mass) measured in prior reactors ranges from 0% to 35% by RIR and Rietveld methods. These low conversions

indicate that the studies done to date on the hydrolysis of Zn nano-aerosols [19–25] have failed to achieve high conversions to ZnO in the aerosol.

While the overall process is similar across these experiments, there were differences in key process parameters. The values of these parameters are listed in Table 2.1. They include the evaporation temperature, T_{EZ}; the evaporation rate; the experimental duration; the quench rate, the reaction zone temperature, T_{RZ}; the molar fraction of H_2O in the Ar/H_2O gas mixture, y_{H_2O}; and the molar ratio of H_2O to Zn, $n_{H_2O} : n_{Zn}$.

Weiss et al. [19] and Wegner et al. [20] studied the simultaneous formation and hydrolysis of Zn nanoparticles at temperatures at and just below the saturation temperature of Zn. They found that the ZnO content of particle deposits on the reactor wall decreased with decreasing temperature and distance along the reactor—from pure ZnO in the hottest part of their reactor ($T \simeq 1000K$) to pure Zn on the filter ($T \simeq 300K$). The temperature in the section with pure ZnO was above the saturation temperature of Zn and resulted in difficult to remove deposits. Thus the reaction in that section was assumed to be heterogeneous Zn vapor hydrolysis. They achieved hydrogen conversions of 60% (on average), which were entirely attributed to reactions with particles deposited on the reactor wall or to the heterogeneous Zn vapor reaction. The average gas residence time in their reactor was 0.5 to $1.5\,sec$. The particles collected from the walls of the reactor near the end of the heated reaction zone were filamentary nanowires with wire diameters of approximately $0.5\,\mu m$.

Ernst et al. [21] followed up on these initial papers with a new reactor that increased the particle residence time from $\sim 1\,sec$ [19, 20] to $5 - 7\,sec$ and separated particle formation from hydrolysis. Particles were formed in a cooling zone by flowing Zn gas through a $17cm$ unheated portion of the reactor. This quench method resulted in a relatively low quench rate ($\sim 400\frac{K}{s}$) which likely led to larger particles than formed in other reactors. The particles then flowed into the reaction zone where they reacted with steam. They achieved 70% conversion, only 4% of which was attributed to conversion of particles in the aerosol. The majority of the conversion was due to reaction of material deposited on the reactor walls coupled with relatively long experimental durations ($60 - 70\,min$). Particles collected on the filter were hexagonal particles about $0.5\,\mu m$ across the hexagonal face.

Initial studies at the University of Minnesota achieved overall conversions of 88 to 96% at temperatures above the saturation temperature of Zn [45]. That the ZnO on the reactor walls was strongly adhered to the walls indicates that hydrolysis occurred by heterogeneous Zn vapor hydrolysis, as in previous work [19, 20]. This study was followed with studies of a tubular reactor and quenching device in which quenching Ar and H_2O gas flows generated Zn nanoparticles and simultaneously reacted them with steam [23, 25]. Three co-axial multi-inlet jets were used to mix the $Zn(g)$ with the quench gases. The innermost jet was the Ar carrier gas with Zn gas, the middle ring jet contained an Ar/H_2O mixture, and the outermost jet was pure Ar. Computational fluid dynamic modeling and a set of three experiments were used to evaluate the quench device and reactor with different flow conditions [25].

The extent of conversion of reactor wall deposits and of particles collected on the downstream filter were measured by XRD analysis. The authors observed that the ZnO content of particles deposited on the walls decreased with decreasing temperature in the reactor, and concluded that hydrolysis is favored at temperatures above $650\,K$. Conversions of almost 100% were observed near the quench ring, again by heterogeneous Zn vapor hydrolysis, while conversions of 22 to 34% were measured for particles collected on the downstream filter (using RIR). In addition, this work pointed to the competing effects of the quench rate and the residence time. Higher quench rates favor smaller particles and therefore faster reaction kinetics. But the high flow rates required to achieve high quench rates lead to shorter residence times, and therefore less time for particles to react in the aerosol. SEM images of filter samples reveal filamentary nanowires, with wire diameters of approximately $100\,nm$.

Funke et al [24] studied the hydrolysis of Zn by feeding commercial solid Zn particles (with average diameter of $158nm$ and initial oxygen content of 1%) into their reactor instead of generating the particles in-situ. The average gas residence time, τ_{avg}, was $0.6\,s$. Based on the Zn particle feed rate and the measured H_2 production rate, the reported overall conversion was 27%. Particles deposited on the reactor wall were completely oxidized due to extended exposure to water vapor at reaction zone temperatures. Ten to 30% of the

particles were collected on a filter at the end of the reactor. They studied the process for $653\,K < T_{RZ} < 813\,K$ and found an approximately linear increase in aerosol conversion, Z, with temperature, from $\sim 7\%$ ZnO at $653\,K$ to $\sim 25\%$ ZnO at $813\,K$. They also conducted a kinetic study of Zn nanoparticle hydrolysis (discussed in greater detail in section 2.2.2), and compared the measured aerosol conversion to that predicted by their kinetic model for corresponding residence times and reactor temperatures. They found that measured aerosol conversions were significantly higher than the kinetic model predicted, especially at lower temperatures. They attribute the difference to increased heat and mass transfer in the aerosol.

Melchior et al. [22] studied the effect of quench rate, evaporation rate, and reaction zone temperature on overall conversion, X, particle yield on the filter, Y, and the composition of particles collected on the filter, Z. They used a tubular aerosol reactor with residence times from 0.8 to 7 sec and reaction temperatures from 573 to $873\,K$. They found that increasing the quench rate from $2 \times 10^4 K/s$ to $10^6 K/s$ resulted in higher conversions measured on the filter, higher particle yield and lower overall conversion. The lower overall conversion is attributed to the higher particle yield at the filter—the bulk of the H_2 produced during the experiments is due to the conversion of particles deposited on the reactor walls, so reductions in particle wall losses lead to reductions in overall conversion. Pure ZnO by heterogeneous Zn vapor hydrolysis was observed in the quench section. They attribute the increase in particle conversion on the filter to the smaller particles formed at higher quench rates. Low evaporation rates lead to smaller crystallite size (determined by XRD), and slight increases in overall particle conversion, yield, and ZnO content on the filter. Increased reaction zone temperatures result in larger crystallite sizes, but the ZnO content on the filter was significantly higher at temperatures above the melting point of Zn. Particles collected on the filter in experiments with the lowest quench rate studied ($2 \times 10^4\,K/s$) corresponding to the longest residence time ($7\,s$), were hexagonal Zn crystals, approximately $300\,nm$ to $2\,\mu m$ across the hexagonal face. In contrast, particles collected on the filter in experiments with the maximum quench rate, corresponding to the shortest residence time ($0.8\,s$), were primarily filamentary Zn nanowires ($\sim 200\,nm$ in diameter) mixed with some hexagonal

particles ($\sim 1\,\mu m$).

None of the prior studies make a conclusive argument that they have successfully reacted nanoparticles in the aerosol to a significant extent. The majority of hydrogen yields are attributed to the reaction of particles deposited on the walls of the heated reactor or heterogeneous Zn vapor hydrolysis in the quenching sections. Thus, an aerosol reactor with increased yields and either increased aerosol conversions or a better understanding of hydrolysis in the aerosol reactor is needed.

2.2 The Reaction

2.2.1 Thermodynamic Considerations

The chemical reactions that enable the conversion of solar energy into hydrogen fuel are the key to this process. In this study, I focus on the second step:

$$Zn + H_2O \rightarrow ZnO + H_2, \tag{2.4}$$

Thus, I present the basic thermodynamics of the reaction for solid and liquid and Zn. The change in enthalpy of a reaction, $\triangle_r H$, can be calculated based on the standard enthalpies of the products and the reactants at a given temperature as [46]

$$\triangle_r H = H^o[ZnO] + H^o[H_2] - H^o[Zn] - H^o[H_2O]. \tag{2.5}$$

At $650K$, $\triangle_r H$ for hydrolysis of solid Zn is $-104.10\frac{kJ}{mol}$. The change in enthalpy of the reaction varies only slightly with temperature. Similarly, the change in entropy in a reaction is

$$\triangle_r S = S^o[ZnO] + S^o[H_2] - S^o[Zn] - S^o[H_2O]. \tag{2.6}$$

At $650K$, $\triangle_r S$ for hydrolysis of solid Zn is $-0.046\frac{kJ}{mol \cdot K}$.

The Gibbs energy represents the compromise between the tendency of a system to decrease its enthalpy and increase its entropy. The Gibbs free energy, $\Delta_r G$, is a measure of the spontaneity of a reaction at a given temperature, where $\triangle_r G < 0$ indicates that a reaction

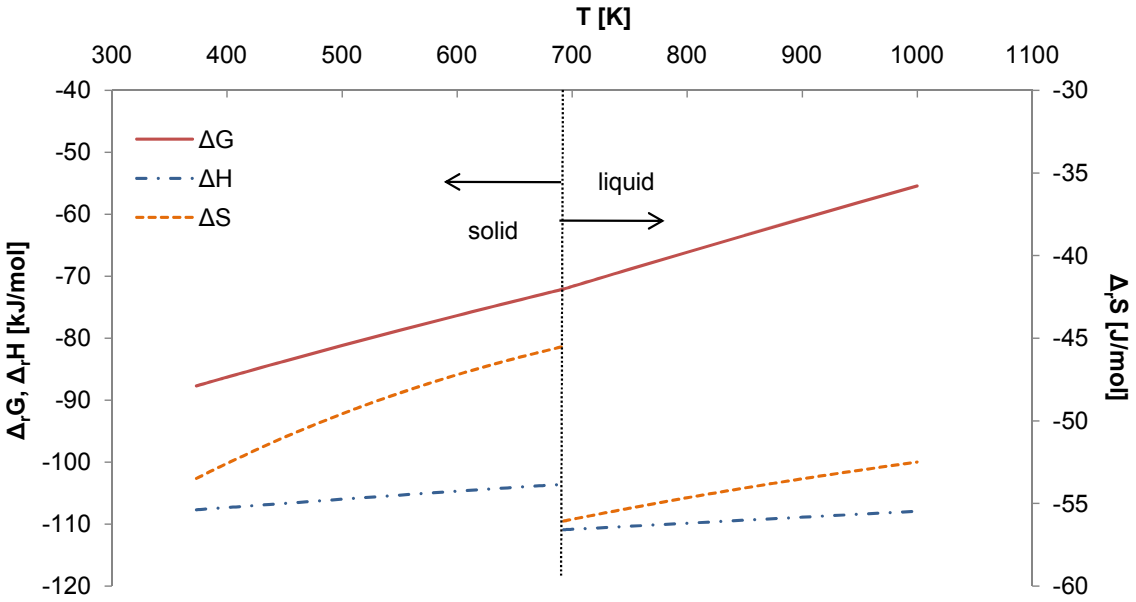

Figure 2.1: Change in Gibbs energy for Zn hydrolysis for solid and liquid Zn.

occurs spontaneously. The Gibbs free energy is

$$\triangle_r G = \triangle_r H - T\triangle_r S. \tag{2.7}$$

At $650K$, $\triangle_r G$ for hydrolysis of solid Zn is $-74.05\frac{kJ}{mol}$. The Gibbs free energy of this reaction for solid and liquid Zn is plotted with $\Delta_r H$ and $\Delta_r S$ against temperature in Figure 2.1. The Gibbs free energy is continuous across solid and liquid Zn particles, as can be seen in Figure 2.1, due to the entropy and enthalpy balancing each other out in the phase change:

$$\Delta_{phase} S = \frac{\Delta_{phase} H}{T}. \tag{2.8}$$

Because $\Delta_r G < 0$ for the temperatures investigated, the reaction is thermodynamically favorable at the temperatures relevant to this study ($500\,K < T_{reactor} < 750\,K$).

The thermodynamics of heterogeneous Zn vapor hydrolysis is also of interest. A Gibbs free energy minimization is used to determine the concentrations of Zn, ZnO, H_2 and all other potential products at chemical equilibrium for a mixture that initially contains $y_{Zn} = 10^{-5}$, $y_{H_2O} = 0.12$ and y_{Ar} for the balance [47]. At temperatures above $500\,K$, the concentration of solid ZnO at chemical equilibrium is above 9.995×10^{-6}; the balance at lower temperatures is $Zn(OH)_2(s)$. Figure 2.2 shows ZnO production as a fraction of

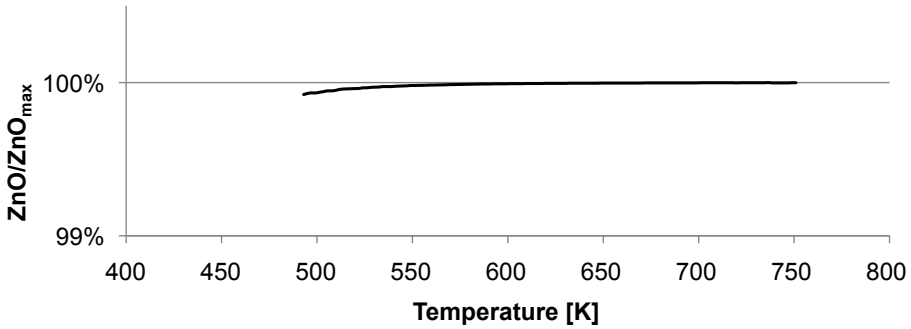

Figure 2.2: ZnO production as a fraction of the theoretical maximum ZnO production at chemical equilibrium for $490\,K \leq T \leq 750\,K$.

the theoretical maximum (i.e. the initial y_{Zn}) at chemical equilibrium for $490\,K \leq T \leq 750\,K$. The heterogeneous Zn vapor reaction is also thermodynamically favorable in the temperatures relevant to this study.

2.2.2 Kinetics

Many studies have documented the effect of the passivating ZnO layer that forms on the surface of oxidizing Zn and results in the reaction becoming diffusion limited. The hydrolysis of bulk or even micron sized Zn is limited by the formation of a passivating ZnO surface layer.The kinetics for the surface reaction of $1\,cm$ diameter Zn disks in nitrogen (N_2) have been measured and analyzed [8, 9] for temperatures from $294K$ to $323K$ with relative humidities of 30 to 95 percent. At these temperatures the product is found to be a hydrated zinc oxide ($(ZnO)_nOH$). Increased temperature and relative humidity results in a greater extent of reaction. Berman and Epstein [10] analyzed the hydrolysis of $Zn(l)$ by bubbling an Ar and steam mixture through a Zn melt at temperatures between 723 and $773K$. They observed ZnO crusts that formed around the steam bubbles and slowed the rate of reaction as diffusion through the ZnO crust became the limiting step in the reaction. Delalu et al. [7] investigated $50-700\mu m$ Zn particles in air or oxygen with 0 to 50% relative humidity above the Zn melting temperature. They found that even at temperatures above the melting point of Zn, partially oxidized particles do not coalesce due to the $ZnO(s)$ layer on the particle surface. They also observed the slow, diffusion limited reaction that occurs after the surface

is fully converted to ZnO. Weidenkaff et al. [11] performed a thermogravimetric study of hydrolysis of Zn particles with a mean diameter of $10\mu m$, and found that 98% pure Zn with finely dispersed ZnO impurities reacts faster than commercial Zn of 99% purity. In addition, reaction temperatures above the melting point of Zn increased the reaction rate. However, the formation of the ZnO layer on the surface prevented the reaction from reaching completion in their study.

In addition to the investigations of bulk and micron-sized Zn, there have been several studies on the kinetics of Zn nanoparticles reacting with steam. Vishnevetsky and Epstein [12] studied the hydrolysis of Zn powder produced in the solar carbothermal reduction of ZnO (2 to $3\,\mu m$ conglomerates of 200 to $500\,nm$ primary particles) and that of commercial Zn ($< 10\,\mu m$). They observed three phases of hydrolysis as they slowly increased the temperature of their reactor. Below $573\,K$ they observed no hydrogen production. When the temperature of their reactor reached $573\,K$, they began to observe a small amount of hydrogen production. At and above $673\,K$ they observed a fast reaction as the surface of the particles hydrolyzed at these favorable temperatures. This fast reaction was followed by a slow, diffusion limited reaction. They also found that if the surface reaction is initiated at $793\,K$ rather than $673\,K$, the hydrogen production rate is doubled. Finally, at $833\,K$ hydrogen conversion for the solar Zn was more than three times that of the commercial powder. The difference was attributed to the difference in the primary particle size of the powder.

Ernst et al. [13] used isothermal thermogravimetric analysis (TGA), in which an H_2O/Ar mixture was introduced after temperatures had stabilized, to measure the hydrolysis rate of Zn particles ($d_p = 164nm$) at $603K$ to $633K$. They operated at atmospheric pressure and with $0.1 \leq y_{H_2O} \leq 0.5$. The reaction was characterized by two phases: an initial fast surface reaction followed by a slower reaction dependent on the diffusion of the reactants through the ZnO layer. They based their understanding of the process on the Wegner theory of metal oxidation, which stipulates that initially there is a constant concentration of Zn^{2+} ions in the particle. The initial surface reaction depletes the Zn ions at the surface and leads to a Zn ion concentration gradient in the ZnO layer.

In the surface reaction regime, Ernst et al. [13] assumed the kinetics to be first order with respect to Zn. The authors explored different reaction orders with respect to steam, and determined that a half order dependency provided the best correlation of the data:

$$r_s = k_s \cdot y_{H_2O}^{0.5}, \tag{2.9}$$

where r_s $\left[\frac{mol}{cm^2 s}\right]$ is the surface regime reaction rate and k_s, the surface regime reaction constant, is described by the general Arrhenius expression,

$$k_s = A_o \cdot e^{(-E_A/RT)}. \tag{2.10}$$

In these expressions T is the temperature, R is the universal gas constant, A_o is the pre-exponential factor and was found to be $2 \times 10^{-5}\,\frac{mol}{cm^2 s}$, and E_A is the activation energy and was found to be $42.8 \pm 7.4\,\frac{kJ}{mol}$.

In the diffusion limited regime, Ernst et al. [13] argued that the diffusing species is Zn^{2+} ions, which diffuse outward from the core of the particle after surface Zn^{2+} ions are depleted in the initial surface reaction. They found no dependence of reaction rate on the molar fraction of steam, y_{H_2O}, and provide that result as further evidence that the reaction is limited by the rate of diffusion of Zn ions. They report that the Arrhenius parameters for the diffusion limited regime are $A_{o,d} = 3 \times 10^{-12}\,\frac{mol}{cm \cdot s}$ and $E_{A,d} = 42.9 \pm 6.5\,\frac{kJ}{mol}$ for

$$r_d = A_{o,d} \cdot e^{(-E_{A,d}/RT)}. \tag{2.11}$$

Funke et al. [24] used non-isothermal TGA to determine the kinetic parameters for the hydrolysis of Zn nanoparticles ($d_{avg} = 158\,nm$). They conducted all experiments at a water concentration of $y_{H_2O} = 1.8\%$. They fit their TGA data to

$$\frac{d\alpha}{dt} = A_o e^{-E_A/RT} \cdot f(\alpha), \tag{2.12}$$

where $\alpha$is the fractional conversion and $f(\alpha)$ is an empirical depletion term. The function that best fits the TGA data is $f(a) = (1-\alpha)^n$, with $E_A = 132 \pm 27\,\frac{kJ}{mol}$, $A_0 = (5.6 \pm 0.3) \times 10^9\,min^{-1}$, and $n = 1.73$. Unfortunately, because $f(a) = (1-\alpha)^n$ has no physical interpretation, these Arrhenius parameters cannot be extended beyond the particle size and

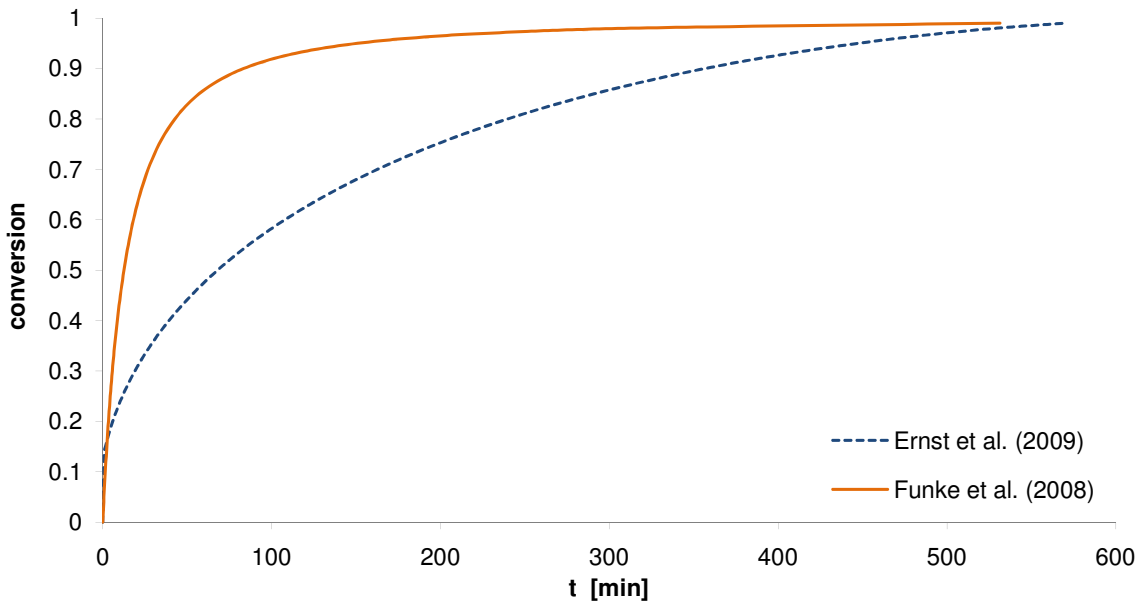

Figure 2.3: Conversion as a function of time, as predicted by Ernst et al. (2009) and Funke et al. (2008).

y_{H_2O} used in their study. In addition, their model does not account for the initial faster surface reaction regime.

The results of Ernst et al. [13] and Funke et al. [24] are compared by applying the values of d_{avg} and y_{H_2O} from Funke et al. [24] to the kinetics presented by Ernst et al. [13]. Figure 2.3 shows Zn conversion as a function of time predicted by Ernst et al. [13] and Funke et al. [24] at $T = 633\,K$, $y_{H_2O} = 1.8\%$, and $d_p = 158\,nm$. The two models predict similar times for complete conversion ($t = 570\,min$ for Ernst et al. and $t = 531\,min$ for Funke et al.), as well as similar times for conversion less than 20%, but very different times for $20\% < \alpha < 98\%$. In this range, Ernst et al. [13] predicts much longer times for conversion. For example Ernst et al. [13] predicts that the particle will be 80% reacted at $240\,min$, compared to $42\,min$ predicted by Funke et al. [24]. See Appendix A for the process used to make this comparison.

Clarke and Fray [18] studied $Zn(v)$ hydrolysis at temperatures above the saturation temperature of Zn—between 781 and $1124K$. They found that $ZnO(s)$ formed on the wall

in a chemical vapor deposition reaction. For $781\,K$ to $1107\,K$, the reaction rate is

$$r = \left[C + C_2(P_{H_2})^{1/2}\right] \cdot (P_{Zn} - P_{Zn,eq}) \tag{2.13}$$

where C_1 and C_2 vary with temperature. At $781\,K$, the lowest temperature for which C_1 and C_2 are reported, they are $3.64 \times 10^{-5}\, moles/(cm^2 \cdot s \cdot atm)$ and $2.91 \times 10^{-5}\, moles/(cm^2 \cdot s \cdot atm^{3/2})$, respectively. The temperatures studied do not overlap with temperatures studied for particle hydrolysis kinetics and are significantly higher then the temperatures in the present study. Further, P_{Zn} in aerosol reactors with some remaining Zn vapor are likely to be much lower than those in Clarke and Fray's work. Thus, their reaction rate can't be extrapolated for comparison with particle hydrolysis experiments or directly related to the present work. However, ZnO by heterogeneous Zn vapor hydrolysis has been observed in Zn hydrolysis reactors when $T_{RZ} > T_{sat}$ [21, 45] and on portions of the walls in aerosol reactors, especially in the Zn vapor quenching sections [22, 25].

2.2.3 Reaction in the Aerosol

Ma and Zachariah [17] explore the kinetics of Zn nanoparticle hydrolysis for the temperature range $373-523\,K$. In this temperature range, they observe a two step hydrolysis reaction. At temperatures below $423\,K$, the Zn nanoparticles react with steam to produce zinc hydroxide ($Zn(OH)_2$) as

$$Zn + 2H_2O \rightarrow Zn(OH)_2 + H_2 \tag{2.14}$$

Above $423 - 438\,K$ the $Zn(OH)_2$ begins to decompose to Zn and H_2O as

$$Zn(OH)_2 \rightarrow ZnO + H_2O \tag{2.15}$$

The authors generate nanoparticles via evaporation and condensation and pass them through a DMA which selects by size, resulting in mono-disperse aerosol of $70\,nm$ particles. This mono-disperse aerosol is mixed with argon and steam and passed through an isothermal furnace where it reacts with the steam. After exiting the furnace, particle mass distribution is measured using an aerosol particle mass analyzer (APM), which determines mass based on the relative strengths of electrostatic and centrifugal forces on the aerosol

particles. With a molar concentration of steam of 15%, they observed increasing mass for temperatures from 373 to 423 K, corresponding to the production of $Zn(OH)_2$. Hydrolysis furnace temperatures from 423 to 498 K resulted in decreasing mass, as the decomposition of $Zn(OH)_2$ began to outpace its formation.

Plotting their measurements of mass change rates against temperature in Arrhenius plots, they find that the formation of $Zn(OH)_2$ in the experimental temperature range has an activation energy of $24 \pm 2\, kJ/mol$. This activation energy is significantly lower than that measured by Ernst et al. [13] and Funke et al. [24] for the formation of ZnO at higher temperatures in a TGA. The overall kinetics of the reaction measured by Ma and Zachariah [17] for 70 nm particles is

$$r = Ay^n e^{(-E_A/RT)} \tag{2.16}$$

where $A = 0.012\, fg/nm^2 \cdot s$, $n = 0.9 \pm 0.1$, and $E_A = 24 \pm 2\, kJ/mol$.

While this study indicates an interesting lower temperature avenue for hydrogen production, it does not provide insight into the higher temperature direct Zn hydrolysis reaction. The authors mention, but do not discuss, material loss due to Zn evaporation at higher temperatures. Presumably, this Zn evaporation prevented them from studying the kinetics of Zn hydrolysis at temperatures above 500 K. However, they use the same experimental apparatus to study the oxidation of aerosol Zn nanoparticles at temperatures from 500 to 773 K [26]. They explore the oxidation of mono-disperse aerosols of 50, 70, and 100 nm particles using the aerosol particle mass analyzer described above. The smaller particles have faster reaction kinetics and complete conversion to ZnO is achieved at lower temperatures than for the larger particles. In addition, for all particle sizes, they observe two temperature regimes—at temperatures above approximately 625 K the activation energy is 20 to 30% lower than that at temperatures below approximately 625 K.

Because there are no data on the hydrolysis of Zn nanoparticles in an aerosol in the temperature range of focus in this study, it is instructive to investigate studies of the oxidation of other metal nano-scale aerosols, especially in comparison with TGA studies. Using a single-particle mass spectrometer (SPMS), Mahadevan et al. [16] analyzed the elemental composition of individual aerosol particles and used the technique to study the kinetics of

thermal decomposition of metal nitrate aerosols (aluminum, calcium, silver, and strontium). The SPMS uses a laser to reduce individual particles to atomic ions, which are measured by a mass spectrometer. This stoichiometric information allowed the group to determine the reaction rate and Arrhenius constants for the process, which they compared to those obtained using traditional thermogravimetric analysis (TGA). Reaction rates determined in the aerosol phase by the SPMS are approximately an order of magnitude higher than the reaction rates determined by TGA. In addition, the TGA results varied with the mass of the sample analyzed. Mahadevan et al. [16] attributed this difference to effects of heat and mass transfer that occur in the TGA but are different in the aerosol reaction. However, they do not state the particle size analyzed in the TGA (only total mass analyzed), so it is unclear whether or not the kinetic differences are due in part to the size of the material being studied (i.e. nanoscale vs. bulk material).

In Park et al. [14] and Rai et al. [15], the same group studied the kinetics of aluminum nanoparticle oxidation and the effect of particle size from 298 to $1373K$. For 30 to $150nm$ particles, the activation energy decreased with decreasing particle size by a factor of ~ 5 between particles $< 50\,nm$ and particles of diameter $100 - 150\,nm$ [14]. The rate limiting step in the oxidation of Al in air was diffusion. The aerosol reaction was again different from reaction measured with TGA. TEM images and particle density measurements of the reacted particles [15] revealed that they were hollow, indicating that Al must diffuse out through the aluminum oxide (AlO_2) shell in addition to or instead of oxygen diffusing in through the oxidized shell. The authors conclude that the reaction takes place in two regimes. Below the melting point of Al the reaction occurs more slowly and is limited by diffusion of oxygen through the shell. At and above the melting point of Al, both Al and O_2 diffuse through the oxide shell resulting in an enhanced oxidation rate. The authors offered a number of explanations about the two regimes. First, when the Al core melts, the density changes, resulting in an expansion of the core. However, the oxide shell remains solid and its expansion is negligible. Thus, the oxide shell is in tension and the liquid core in compression. The steep pressure gradient that results is offered as one mechanism for increased diffusion of Al through the AlO_2 shell, and thus increased reaction rate. In addition, they argue that

the liquid Al is more mobile and thus more likely to diffuse outward than solid Al.

Though these studies do not offer information specific to Zn nanoparticle hydrolysis, they do offer very important insights into the reaction of metal nano-aerosols. The TGA analysis discussed in section 2.2.2 [13, 24] may underestimate the reaction rate that occurs in an aerosol. In addition, the reaction zones in previous studies of Zn nanoparticle hydrolysis were generally kept to temperatures below the melting point of Zn to reduce particle growth and sintering. However, as with aluminum and its oxide, the melting point of Zn ($693\,K$) is significantly less than the melting point of ZnO ($2248\,K$), indicating that reaction temperatures above the melting point of Zn may also result in much faster reaction rates. This inference is also supported by the increased particle conversion measured in Melchior et al. [22].

2.3 Nanoparticle Evolution

In the evaporation/condensation process the metal precursor material, evaporated and carried through a reactor by an inert gas, undergoes rapid controlled quenching. In the quenching process, evaporated metal atoms lose kinetic energy through collisions with inert-gas atoms, leading to a high degree of supersaturation (defined by the saturation ratio, S', the ratio of monomer concentration to the monomer concentration at saturation). The critical cluster size (d^*) is the size at which the evaporation rate and the condensation rate are balanced. Monomer clusters with diameter equal to or greater than the critical diameter form stable particles. Because d^* is inversely proportional to $\ln S'$, when the metal vapor suddenly reaches high degrees of supersaturation, the corresponding critical diameter becomes very small. A nearly instantaneous "nucleation event" occurs as a result [28]. Because the degree of supersaturation achieved determines the primary particle size, process parameters that result in higher saturation ratios lead to smaller primary particles. Fast quench rates result in higher saturation ratio peak values and the formation of smaller particles [28–36]. In addition, reduced concentration of the metal vapor results in fewer particles, as less mass is available for nucleation.

Further growth by condensation, coagulation, and coalescence follows nucleation. Condensation occurs as remaining vapor condenses on the surface of the nucleated nanoparticles. Particle growth is dominated by condensation when particle concentrations are low and few collisions occur. Growth by coagulation occurs when two nuclei meet due to a process such as Brownian motion and are joined, and thus is the dominant growth mechanism at high particle concentrations. The rate of coagulation is strongly dependent on the particle concentration, so reduced evaporation rate (and thus reduced concentrations) lead to less growth by coagulation. When particles coalesce (or sinter), the species of the two nuclei diffuse into one another. At temperatures low enough that coalescence is negligibly slow compared to coagulation, loose agglomerates with open structures are formed [34, 37]. These structures retain the small crystalline grain size of the primary particles and thus relatively high specific surface areas. When temperatures are high enough that particles coalesce faster than they coagulate (generally at and above the melting point of the particle material), larger primary particles are generally produced, and the grain size grows [34, 38], resulting in a reduction of the specific surface area.

Both experimental [29, 39] and analytical [30] work show that particle diameter increases with increasing system pressure and inert gas molecular weight. Both higher system pressure and molecular weight impede the diffusion of the particles and vapor molecules away from each other, creating a region of higher growth by coagulation and condensation [29, 34]. This effect may be partially reduced by the use of higher inert gas flow rates, which rapidly remove particles from regions of high concentration [35]. Higher quench rates also result in a reduction in particle coalescence and a corresponding increase in specific surface area [40]. Growth by coagulation depends strongly on the concentration of particles in the reactor, which can be reduced through the use of lower evaporation rates. Longer residence times and higher system temperatures also result in greater particle growth.

One study has been conducted on the effect of a reacting gas on the size distribution of metal nanoparticles [27]. In this study, Ag nanoparticles were formed in pure helium (He) and in a He and O_2 mixture. Particles formed in He ranged in size from 15 to 180 nm, with a mean particle size of 75 nm. Particles formed in the presence of O_2 were smaller—ranging

from 10 to 120 nm, with a mean particle diameter of 44 nm. In addition, Brunauer, Emmett and Teller (BET) analysis showed that the presence of O_2 had a significant effect on the specific surface area of the particles, increasing it to 24 m^2/g from 6.5 m^2/g. The reduced size and increased surface area was attributed to the formation of oxide shells on the surface of particles, which reduced growth by coalescence [27].

2.3.1 Analytical studies of nanoparticle growth

A number of models have been used to characterize the growth of metal nanoparticles in the evaporation/condensation process [28, 31, 42, 43], and the most relevant results are discussed above. In addition, Panda and Pratsinis [30] used a simple model of particle nucleation, condensation, and coagulation in an aerosol reactor during an evaporation/condensation process at non-isothermal conditions to study the effect of process parameters on Al particle size. Their model is consistent with their empirical data, as well as other, more complex models.

Ernst [41] used a one dimensional model to study mono-disperse particle size evolution by nucleation, condensation, coagulation, diffusive and thermophoretic effects at non-isothermal conditions. Essentially, his study expands the model developed by Panda and Pratsinis [30] to include vapor and particle losses by deposition on the reactor walls due to diffusion and thermophoresis, and applies it to the study of Zn nanoparticles. He found that Zn vapor deposition on the walls is dominated by diffusion and occurs primarily before and during nucleation, while particle deposition on the reactor walls is dominated by thermophoresis when temperature gradients are present. In addition, he concluded that coagulation plays a significantly smaller role in particle growth than condensation. He also found that particle growth takes place below the melting point of zinc and results in hexagonal particles.

Chapter 3

Reactor Design

The general goals for a reactor that both synthesizes and reacts Zn particles with steam can be contradictory. On the one hand, the required rapid quench of the Zn vapor in particle formation, generally achieved by rapidly mixing the Zn vapor with a cooler gas, and the need to thoroughly mix the reactants point to high Re_d flows. On the other hand, the need maximize yields on the filter by reducing or eliminating particle deposition on the walls of the reactor also point to low Re_d flows, as turbulence is a likely contributor to deposition on the wall. Long residence times (for greater conversion to ZnO) are another reactor design goal. Increased residence time is achieved through decreased velocity at the diameters and lengths reasonable in laboratory scale aerosol reactors, again resulting in low Re_d flows. To meet these goals, a $76\,mm$ diameter tubular reactor that incorporates a transverse jet, or jet in a cross flow, was designed. Transverse jets are known to have enhanced mixing via carefully studied vortical structures.

One of the most familiar examples of transverse jets is the hot CO_2 and water vapor that emerges from a smokestack into a breeze. As the CO_2 and water vapor exit the smoke stack, they are rapidly cooled by the free stream air. The water vapor condenses into water droplets—the white billowing clouds, or "smoke," that observers can see. Initially, the jet flows upward, but eventually it bends into the direction of the breeze. The jet trajectory depends on the relative velocities and densities of the smokestack gasses and free stream air. Though the length scales and Reynolds numbers are very different in the Zn aerosol reactor,

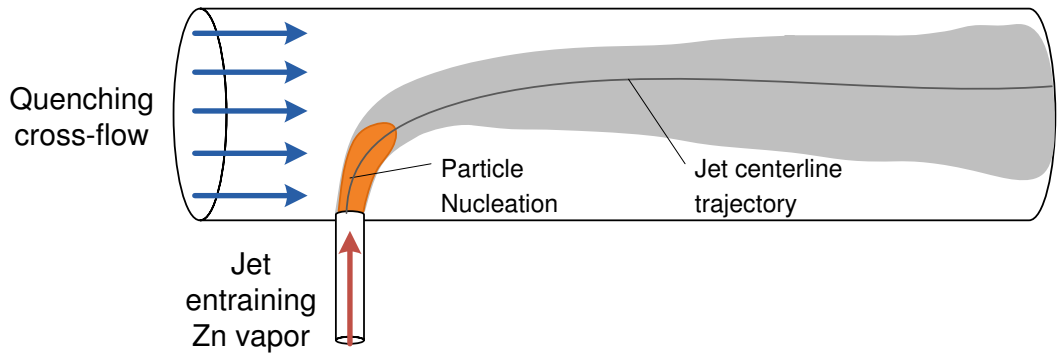

Figure 3.1: Conceptual drawing of the transverse jet Zn hydrolysis reactor.

the concept is the similar. In the experimental reactor, shown conceptually in Figure 3.1, the evaporated Zn is entrained in a vertical flow of argon through a pipe of diameter, d_j. The cooler, quenching mixture of Ar and H_2O flows through a perpendicular pipe. As the Zn vapor enters the quench flow pipe, it is cooled rapidly by the quenching cross-flow, thereby condensing into nano-scale particles.

The relative velocities of the jet and quenching cross-flow fluids can be tuned to ensure that the jet has enough momentum to enter into the center of the pipe, but not so much that it impinges on the wall of the tubular reactor. In this manner, a transverse jet reactor has the potential to produce Zn nanoparticles while mitigating one significant problem that has plagued Zn aerosol hydrolysis reactors: deposition of Zn and/or ZnO on the walls of the reactor. Particle deposition in the walls undermines the viability of a continuous process (a major potential advantages of an aerosol approach), affects the aerosol process by removing the majority of the mass from the aerosol, and results in overall hydrogen production rates much higher than can be attributed to reaction in the aerosol. By controlling the effective velocity ratio we can potentially keep the majority of the Zn particles away from the walls of the reactor.

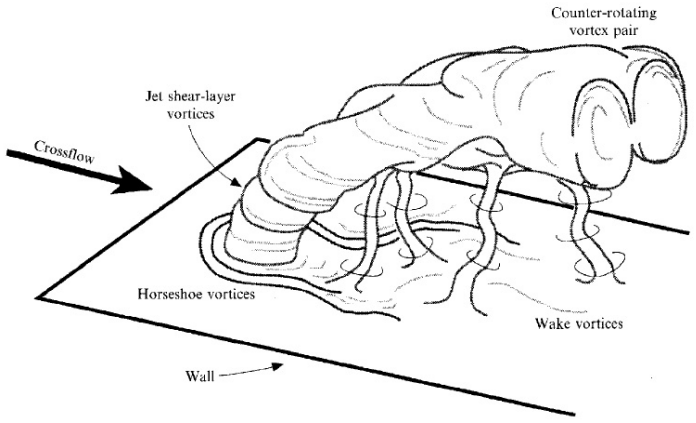

Figure 3.2: Sketch of a transverse jet and the four types of vortical structures characteristic of such jets. The counter-rotating vortex pair is the dominant feature. Vortices also form at the jet shear layer, around the upstream edge of the jet on the wall (i.e. horseshoe vortices), and in the wake of the jet, extending from the wall to the jet. The sketch is taken directly from Fric and Roshko (1994).

3.1 Transverse Jets

Traverse jet flow fields are characterized by a jet issuing transverse to the primary fluid stream-wise direction (termed the cross-flow), which is subsequently deflected, curving in the direction of the free stream, as depicted in Figure 3.2. Transverse jets have been studied both experimentally [48–52] and analytically [53–56]. Though some researchers consider jets of a variety of cross-sectional shapes, this discussion is limited to circular jets. Near the jet inlet, the cross flow moves around the circular jet in much the same way as flow around a solid cylinder, resulting in a high pressure region just upstream of the jet [56]. As in flow around a cylinder, there are stagnation points upstream and downstream and minimum pressures at the lateral edges, resulting in the jet taking on an oval shape slightly downstream of its entry point. On the lateral edges of the jet, shearing between the jet and the cross-flow results in a kidney shaped cross-section and, farther downstream, in a counter-rotating vortex pair (CRVP) [53]. The counter-rotating vortex pair is the dominant feature of transverse jets, and is a the primary mechanism for mixing between the jet and the cross-flow [52, 53, 57, 58].

In addition to the counter-rotating vortex pair, three other vortical structures charac-

terize transverse jets. All four features of transverse jets are depicted in Figure 3.2. Second to the CRVP, the ring like vortices at the jet shear layer contribute the most to mixing. At high Reynolds numbers ($3800 \leq Re_d \leq 11400$), these vortices result from Kelvin-Helmholtz instability, as in a free jet [52]. At low Reynolds numbers ($Re_d \backsimeq 100$), the instability mechanism that leads to the formation of the jet shear layer vortices has been postulated to be dominated by the curvature of the jet and instabilities in the CRVP [57]. At all Reynolds numbers, instabilities in the CRVP and the ring-like jet shear layer vortices result in mixing between cross-flow and jet mass [52, 53, 57, 58]. The horseshoe vortex forms on the upstream edge of the jet at the wall due to the adverse pressure gradient that exists just upstream of the jet on the wall [52, 59]. Finally, so called wake vortices originate in the laminar boundary layer of the wall in the wake of the jet. Fric and Roshko (1994) argue that the flow around the jet results in an adverse pressure gradient on the wall, on the downstream lateral edges of the jet, and that this adverse pressure gradient results in "separation events" in the wall boundary layer which then become the wake vortices [52]. The horseshoe and wake vortices are relatively weak compared to the CRVP [53].

The trajectory of a jet in cross-flow is influenced primarily by the effective velocity ratio

$$R = \left[\frac{\rho_j \bar{u}_j^2}{\rho_{cf} \bar{u}_{cf}^2}\right]^{\frac{1}{2}} \tag{3.1}$$

where $\bar{u}_j$ is the average jet velocity, $\bar{u}_{cf}$ is the average cross-flow velocity, ρ_j is the jet fluid density, and ρ_{cf} is the cross-flow fluid density. When the density of the fluids in the jet and the cross-flow are identical, the effective velocity ratio, R, simplifies to the ratio of the average speed of the jet to that of the cross-flow. The trajectory of the jet is strongly dependent on R—a higher value of R corresponds to a jet with a higher kinetic energy relative to the cross-flow. Thus, increases in R will result in jets that penetrate farther into the cross stream before being deflected. In addition, the velocity profiles of both the jet and the cross-flow can significantly affect the jet trajectory. Numerous studies have been done to develop empirical expressions for the jet trajectory, normalized by d_j or Rd_j, many of which are summarized in [53]. The expression for jet trajectory normalized by Rd_j is

$$\frac{y}{Rd_j} = A\left(\frac{x}{Rd_j}\right)^B \tag{3.2}$$

where empirical results fit $1.2 \leq A \leq 2.6$ and $0.28 \leq B \leq 0.34$. The range of empirical values for A and B result in a wide range of predicted jet trajectories for any given R and d_j—Rd_j scaling does not sufficiently characterize jet trajectory.

Muppidi and Mahesh [56] attribute the failure of scaling with Rd_j to the fact that the parameter does not contain information about the cross-flow and jet velocity profiles. They demonstrate that the cross-flow boundary layer thickness and the jet velocity profile influence the jet trajectory. Qualitatively, they found that a thin cross-flow boundary layer results in the jet penetrating deeper into the cross-flow than when the boundary layer is thick, because the thinner boundary layer has more momentum close to the jet exit. Similarly, a jet with a parabolic velocity profile penetrates farther into the cross-flow than a jet with a turbulent velocity profile. The deeper penetration of the jet with the parabolic velocity profile is attributed to the higher momentum at the center of the jet [56]. They developed a trajectory scaling that incorporates the velocity profiles of the jet and the cross-flow. Their expression is

$$\frac{y}{Rd} = A' \left(\frac{x}{Rd}\right)^{0.32} \left(\frac{h}{d}\right)^{0.15} \tag{3.3}$$

where h parametrizes the relative inertia of the jet and the cross-flow and takes into account both the jet velocity profile and the shape and thickness of the cross-flow boundary layer. This parameter is defined by

$$\int_0^h d_j \left(\frac{u_{cf}(y)}{u_\infty}\right)^2 dy = 0.05 R^2 \pi \frac{d_e^2}{4} \tag{3.4}$$

in which d_e is an effective jet diameter, defined such that

$$\rho_j \int_A u_j^2 dA = \frac{\pi d_e^2}{4} \overline{u_j}^2 \tag{3.5}$$

where $\overline{u}_j$ is the mean velocity of the jet. For a parabolic velocity profile, $\frac{d_e}{d_j} = 1.15$, while for a mean-turbulent velocity profile, $\frac{d_e}{d_j} = 1.09$. Using this new trajectory scaling they are able to make all their simulation data collapse for $A' \simeq 1.6$[1].

In practice in the transverse jet reactor, the cross-flow velocity profile is quite different from the boundary layer and free-steam velocity of flow over a plate used above. In the

[1]This value for A' was determined by fitting their collapsed data to equation 3.3; they do not give a value for A'

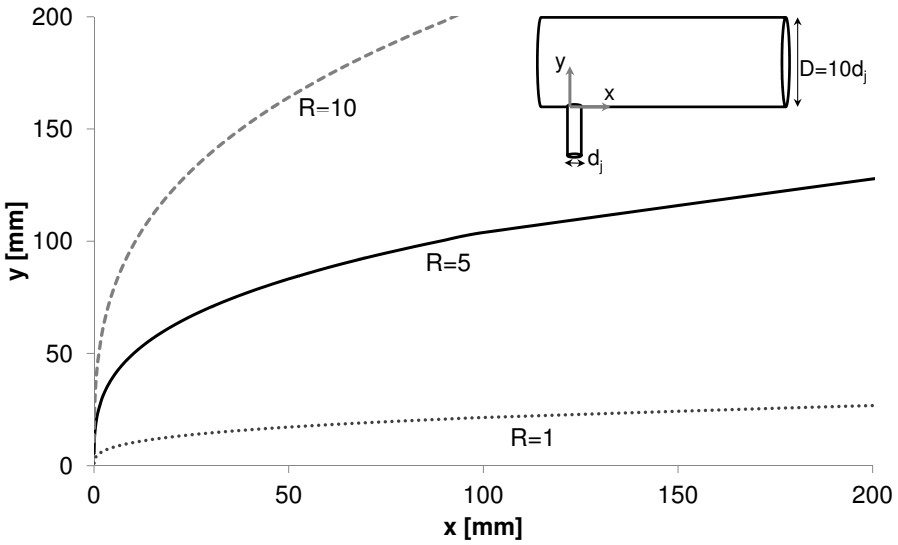

Figure 3.3: Predicted jet trajectories for $R = 1$, 5, and 10, assuming $d_j = 10\,mm$, $\frac{d_e}{d_j} = 1.15$ (parabolic velocity profile), and a uniform cross-flow velocity profile, with inset schematic sketch of a transverse jet tubular reactor.

transverse jet reactor, the velocity profile is likely to be a partially developed laminar velocity profile for flow through a pipe. The development length is unknown in the design phase, so for the sake of estimation, a uniform velocity profile is assumed for the cross-flow:

$$u_{cf}(y) = u_\infty \tag{3.6}$$

In this case, Equation 3.4 simplifies to

$$\frac{h}{d} = 0.05R^2\frac{\pi}{4}\left(\frac{d_e}{d_j}\right)^2 \tag{3.7}$$

Equations 3.3 through 3.7 are used to predict approximate jet trajectories in the experimental reactor for $R = 1$, 5, and 10, assuming $d_j = 10\,mm$, $\frac{d_e}{d_j} = 1.15$ (parabolic velocity profile); the results are shown in Figure 3.3 with a sketch of the reactor concept. In Figure 3.3, y is the penetration distance into the free stream, with $y = 0$ at the jet inlet, and x is the axial distance downstream of the jet inlet. When $R = 1$, the jet trajectory remains very near the wall—even at $x = 200\,mm$, the jet has only penetrated $27\,mm$ into the free stream. In a tubular reactor, as depicted in the inset in Figure 3.3, significant particle deposition on the bottom part of the reactor in the region downstream of the jet entrance is

anticipated for such a low R. On the other hand, when $R = 10$, the predicted jet trajectory indicates that the jet would penetrate much farther into the free stream before bending in the direction of the cross-flow. In fact, the jet begins to bend at approximately $x = 20\,mm$, at which point the jet has already penetrated over $120\,mm$ into the cross-flow. A reactor diameter, D, of $\sim 10 d_j$ is anticipated—$D = 100\,mm$ for the assumptions used here. Thus, significant particle deposition on the top part of the tubular reactor is anticipated for a jet with $R = 10$, due to the jet impinging on the upper part of the reactor. A jet with $R = 5$ has a predicted trajectory that balances the need to penetrate far enough into the cross-flow to get the jet mass (i.e. Zn) away from the bottom part of the reactor, to avoid deposition there, with the need for a relatively rapid bend into the direction of the cross-flow, to avoid impingement on the upper part of the reactor. Thus, further analysis will be based on a reactor with $d_j = 10\,mm$, $D = 10 d_j$, and $R \approx 5$.

3.2 Simulation Details

A numerical simulation of the flow field is used to predict the jet quenching rates and mixing between the jet and cross-flow fluids. High quench rates are essential for the formation of small particles, so a key result of the simulations is the temperature along jet streamlines. Based on past work, a quench rate of at least $1000\,K/s$ is desired [19–25]. Direct numerical simulations are generally required to capture the small scale instabilities and vortical structures of transverse jets [53–56]. The FLUENT computational fluid dynamics (CFD) [60] simulations presented here are Reynolds Averaged Navier Stokes (RANS) simulations, and are not able to capture those details. However, all four types of vortical structures have been observed experimentally, even at very low Reynolds numbers ($Re_d \backsimeq 100$) [57]. Thus, this numerical simulation can be understood to provide a conservative estimate of the mixing rate between the jet and cross-flow fluids because it only captures the CRVP and the high pressure region upstream of the jet. The degree of mixing in the experimental reactor is likely to be higher than modeled. The simulation is carried out in two stages using the FLUENT software. In the first stage, a steady simulation is used to prove grid independence

of the solution. The second stage of the simulation employs a transient model. Results from this final stage of the simulation are used to predict the quench rates along jet streamlines and assess the mixing between jet and cross-flow fluids.

The modeling domain is depicted in Figure 3.4. The simulation domain consists of a $100\,mm$ diameter, $400\,mm$ long cylinder with a $10\,mm$ diameter circular opening $200\,mm$ from each end, at $x = 0\,mm$. The quenching flow of argon and steam is assumed to enter the reactor with a uniform velocity profile, a mass flow rate of $3.63 \times 10^{-4}\,kg/s$, and temperature of $473\,K$. A likely molar fraction of steam of $y_{H_2O} = 0.3$ is assumed and the temperature dependent properties of the quenching fluid are set by mass-weighted mixing laws. At these conditions, $Re_D = 145$, based on the assumed velocity and temperature and the reactor diameter. The hot jet that enters at $x = 0\,cm$ is modeled as pure Ar entering with a uniform velocity profile and a temperature of $1000\,K$. Zinc is neglected from the jet because the anticipated molar fractions of Zn in the jet are very low ($y_{Zn} \approx 10^{-3}$). The mass flow rate in the jet is $1.5 \times 10^{-5}\,kg/s$, corresponding to $Re_{d_j} = 34$. The jet enters the reactor at a 90° angle to the main flow through a circular opening.

In the first stage of modeling, the mesh was generated through a series of refinements. In FLUENT, when a region undergoes adaptation, the distance between each node is approximately halved, resulting in over twice as many nodes, faces that are approximately a quarter

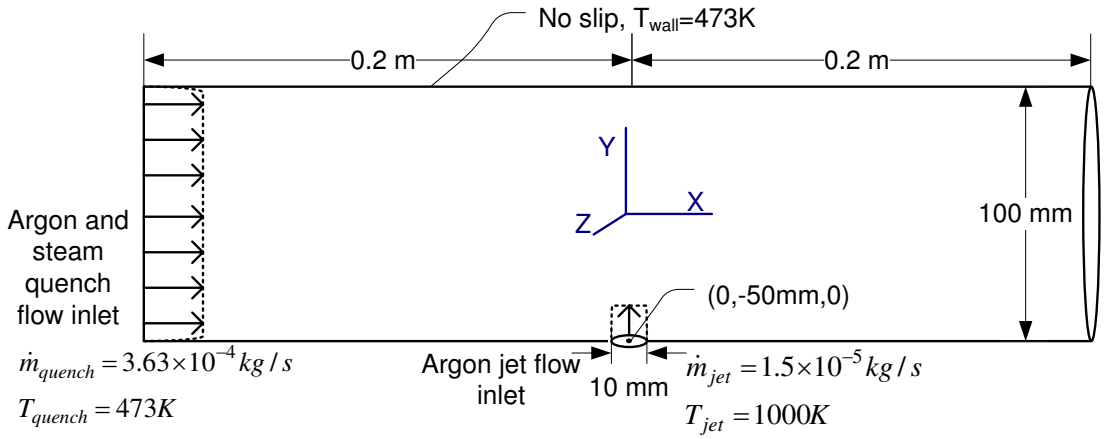

Figure 3.4: Schematic of the modeling domain and boundary conditions for the transverse jet reactor.

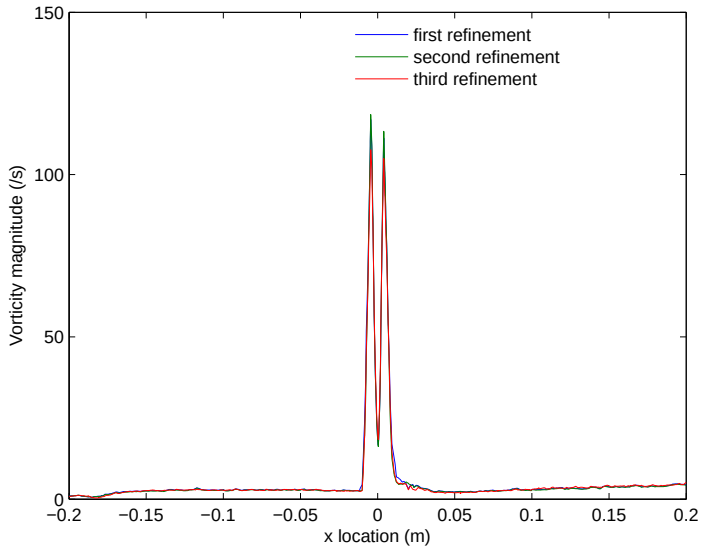

Figure 3.5: Vorticity data for three different meshes along the line $10\,mm$ from the bottom of the reactor in the plane of symmetry.

of their previous size, and volumes that are approximately an eighth of their original size. In the grid refinements, volumes for refinement are chosen based either on distance from the wall boundary or on contours of constant jet mass fraction. The initial unstructured mesh had 100731 nodes, spaced relatively evenly throughout the modeling domain. The first refinement was over the region $3\,mm$ from the wall and where the jet mass fraction was greater than or equal to 0.2, resulting in a mesh with 413349 nodes. The second refinement was carried out over the region $5\,mm$ from the wall and where the jet mass fraction was greater than or equal to 0.05, resulting in a mesh with 691799 nodes. The third refinement was carried out over the entire domain and resulted in a mesh with 839930 nodes. Vorticity, velocity, mass fraction, and temperature results were compared across the three levels of refinement and the solution was found to be independent of the grid within 6%. Velocity, jet mass fraction, and temperature data are key results in this simulation, so the grid independence of these data is essential. Vorticity data is more likely than velocity or mass fraction data to change with the mesh; it is shown for each of the three levels of refinement along the line $10\,mm$ from the bottom of the reactor in the plane of symmetry in Figure 3.5 . The grid independent solutions in this stage of modeling indicate that $R = 5.6$, corresponding

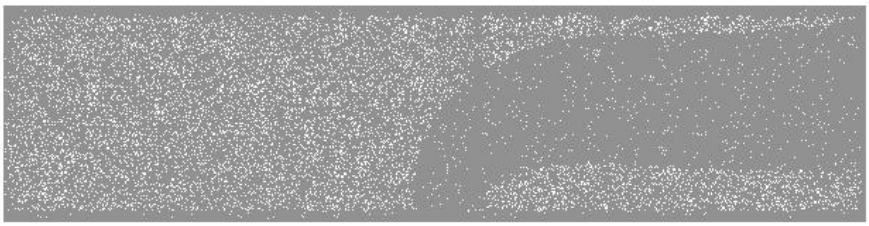

Figure 3.6: The plane of symmetry of the unstructured mesh with 691799 nodes used for the second stage of simulations.

to a jet mass flow rate of $1.5 \times 10^{-5}\, kg/s$, results in a jet trajectory approximately down the center of the reactor.Thus, in the second, transient, stage of modeling, $R = 5.6$ and the mesh generated after the second refinement is used. The mesh is shown in Figure 3.6 for the symmetry plane.

In the second stage of modeling, the transient, laminar, three-dimensional, and species transport models are applied to the governing conservation equations of mass, momentum, and energy. The Reynolds number of the jet is 34 and that of the cross-flow is 145, based on the respective inlet temperature and velocity assumptions and diameters (note that uniform velocity profiles are assumed for both inlets). The species transport model is used to model the mixing of the jet gas with the main reactor flow. Particle nucleation is not modeled. The boundary conditions are as described above. The solutions are considered converged when the residuals of continuity and velocity parameters are less than 10^{-4}, the species residual is 10^{-12}, and the energy residual is 10^{-8}.

Calculated parameters such as temperature, velocity, jet mass fraction, and pressure do not change appreciably after $t = 8\, s$, which is carried out until $t = 15\, s$. Figure 3.7 shows the jet mass fraction as a function of pathline distance along a pathline originating at the center of the jet for 8, 12 and 15 seconds into the transient simulation.

3.3 Results

The results of the transient simulation of the transverse jet reactor are presented here. The simulation domain consists of a $100\, mm$ diameter, $400\, mm$ long cylinder with a $10\, mm$

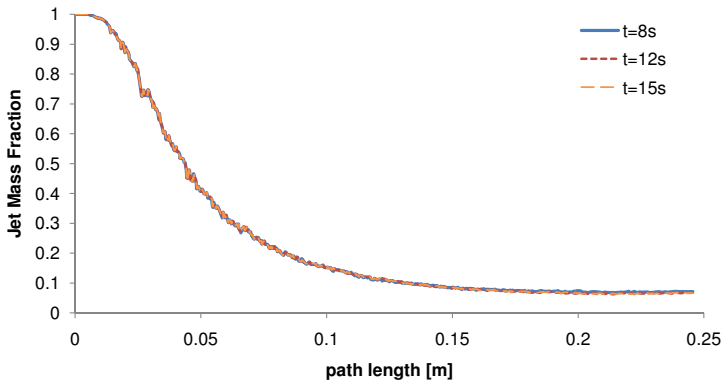

Figure 3.7: Jet mass fraction as a function of pathline distance along a pathline originating at the center of the jet for 8, 12 and 15 seconds into the transient simulation.

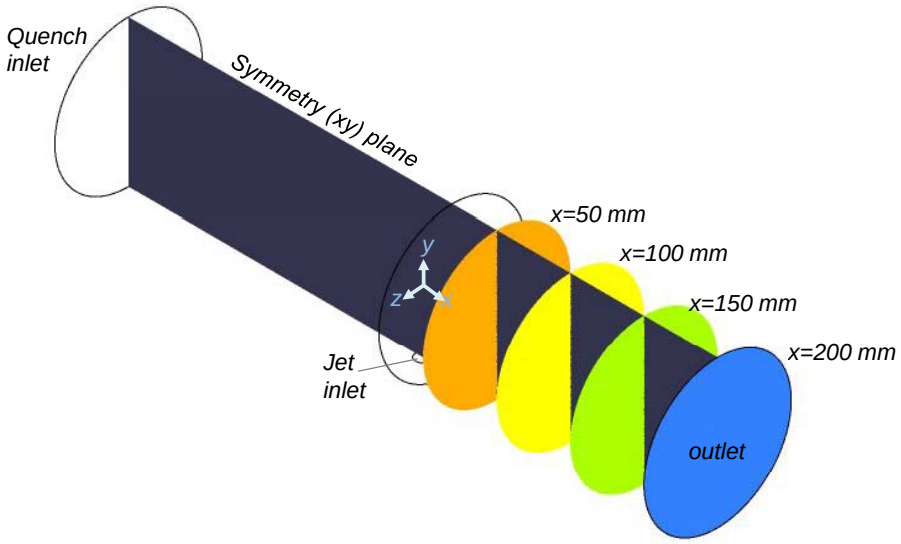

Figure 3.8: The symmetry plane, and cross-sectional planes at $x = 50, 100, 150$, and $200\,mm$.

diameter circular opening $200\,mm$ from each end, at $x = 0\,mm$ (refer to Figure 3.4). Because the jet enters the reactor perpendicular to the cross-flow from a single location, the flow in the reactor is not axi-symmetric. Isobars, isotherms, contours of constant jet mass fraction, and contours of constant vorticity are presented on the plane of symmetry (i.e. the xy plane, on either side of which the flow is the same) and on planes perpendicular to the axis of the reactor (i.e. plans of constant x). These planes are shown in the modeling domain in Figure 3.8. The model captures the counter rotating vortex pair (CRVP), the dominant feature

of transverse jets. The results indicate that quench rates on the order of $10^4\,K/s$ can be achieved, even at the $Re_D = 145$. Further, the numerical results indicate that the reactants are well mixed—the peak value of the fraction of mass originating from the jet is less than 20% for $x \geq 50\,mm$ and less than 10% for $x \geq 150\,mm$. These results are presented in more detail below.

As discussed previously, the most defining feature of a jet in cross flow is the CRVP [52]. Another feature of jets in cross-flow is the high pressure region on the upstream side of the jet [56]. These features are illustrated in Figure 3.9 (CRVP) and Figure 3.10 (pressure). Figure 3.9(a) shows pathlines originating from the jet inlet (blue pathlines) and the cross-flow inlet (red, orange, yellow and light green pathlines). The counter rotating vortex pair can be clearly seen in the swirling pattern of the jet pathlines. The entrained cross-flow gas is evidenced by the yellow and light green cross-flow pathlines inside and surrounding the blue jet pathlines. Figure 3.9(b) shows contours of constant axial vorticity at cross-sections of the reactor at $x = 30\,mm$ and $x = 50\,mm$ (i.e. downstream of the center of the jet inlet). At $30mm$ downstream, the absolute magnitude of axial vorticity peaks at $13\,s^{-1}$, and by $50\,mm$ the peak vorticity has decreased to $10\,s^{-1}$. The counter rotation of the vortex pair is indicated by negative and positive values of the vorticity. It is expected that the CRVP drives the mixing that allows for the rapid drop in temperature as the jet and cross-flow gasses mix. The smaller scale vortical structures common to all transverse jets–the jet shear layer vortices, the horseshoe vortex, and the wall vortices–are not captured in this simulation.

Figure 3.11 shows contours of constant jet mass fraction in (a) the symmetry plane and (b) cross-sections of the reactor at axial locations 50, 100, 150, and $200\,mm$ downstream of the jet inlet. The jet trajectory can be seen in the contours of jet mass fraction. The jet mass is not near the wall until it is very diffuse (jet mass fraction of $\sim 5\%$ at $x = 160\,mm$), thereby potentially reducing particle deposition on the walls. The entrainment of cross-flow mass into the jet is visible in the contours of jet mass fraction. By $150\,mm$ downstream of the jet entrance, the maximum concentration of jet mass is 10%–this maximum value is located in the center of the CRVP. The jet grows in width and height as it entrains the

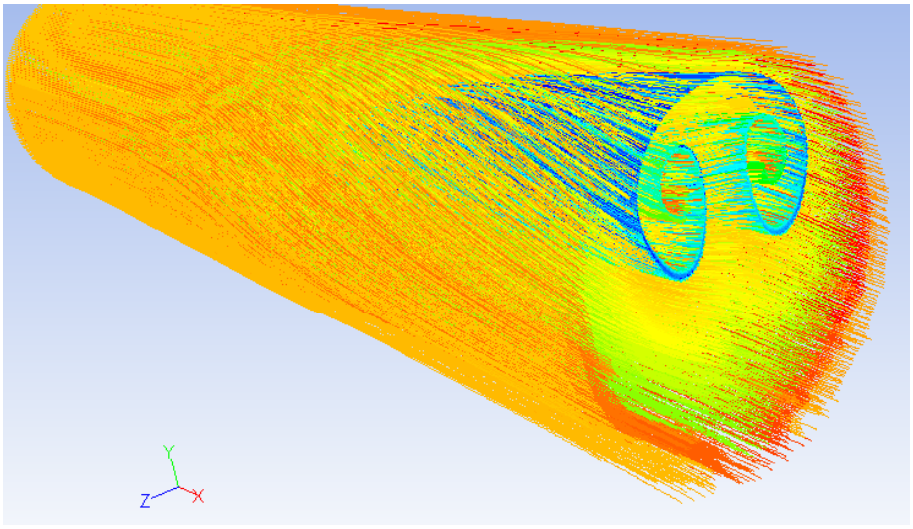

(a)

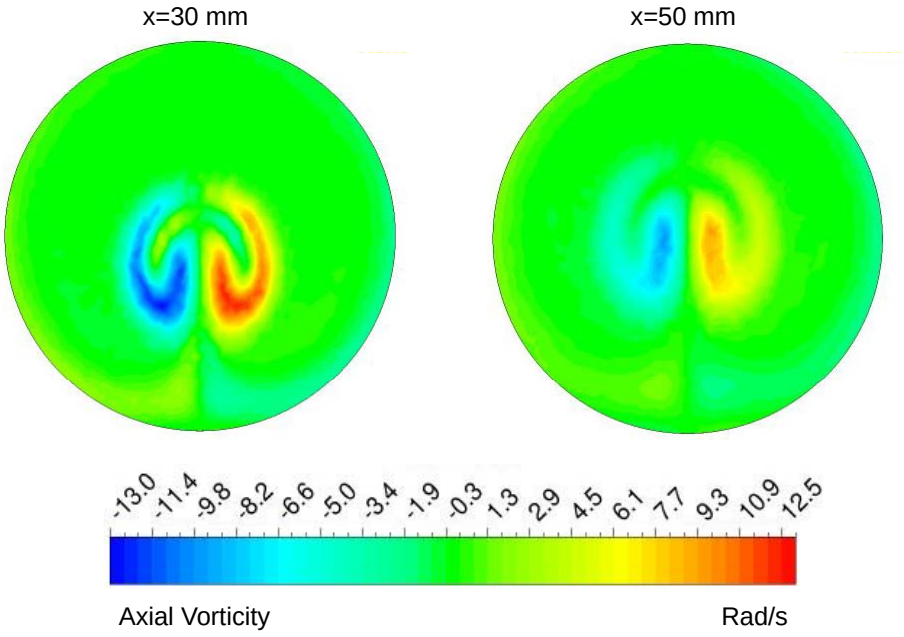

(b)

Figure 3.9: (a)Pathlines generated from the jet inlet (blues) and quench flow inlet (reds, oranges, and yellows). The blue swirl is formed by the counter rotating vortex pair that entrains the cross-flow gas, as can be seen in the warmer colored streamlines surrounding and inside of the swirl. (b) Axial vorticity on cross-sections of the reactor at $x = 30$ and $50\,mm$.

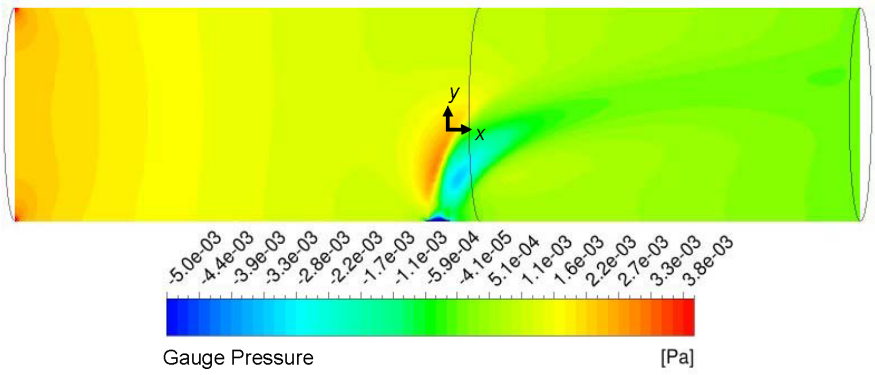

Figure 3.10: Isobars at $t = 15\,s$. The high pressure region on the upstream edge of the jet is a trait of transverse jets.

cross-flow gas. Initially $10\,mm$ in diameter, by $x = 150\,mm$, the jet width, where the jet boundary is defined here by the jet mass fraction of 5%, is approximately $60\,mm$.

Nanoparticle formation is expected when the temperature of the Zn vapor rapidly falls below its saturation temperature at rates on the order of 10^3 to $10^4\,K/s$ [28, 30]. At the expected molar concentration of Zn in the evaporation zone ($y_{Zn} = 5.5 \times 10^{-3}$), the saturation temperature is $824\,K$. Isotherms are shown in Figure 3.12 for the symmetry plane at $15\,s$ into the transient simulation. Qualitatively, Figure 3.12 illustrates the steep temperature gradients near the jet inlet. Isotherms are not shown for the cross-sectional planes at $x = 50$, 100, 150, and $200\,mm$ because the temperatures at those locations are nearly uniform. At the cross-sectional plane defined by $x = 50\,mm$, $T \leq 496\,K$ for all locations in that plane; by $x = 200\,mm$, $T = 476 \pm 3\,K$ at all locations on the plane. Gas temperature along a pathline originating at the center of the jet decreases from $1000\,K$ to $700\,K$ about $11\,mm$ along the pathline, at a residence time of $34\,ms$. After a pathline distance of $30\,mm$ (corresponding to a residence time of $0.1\,s$) the temperature at the center of the jet has dropped to $550\,K$—this is approximately the point at which the jet begins to bend into the direction of the cross-flow. The average quench rate is calculated as the linear $\Delta T/\Delta t$ for the first $10\,ms$ along each pathline. The average quench rate calculated for a pathline generated from the center of the jet inlet is approximately $10000\,K/s$, while the quench rate at the edge of the jet is approximately $30000\,K/s$. Temperature is shown

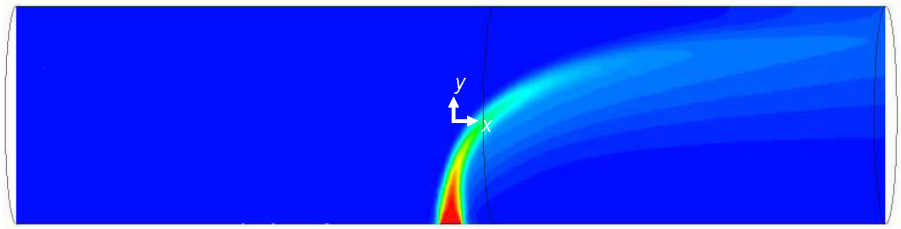

(a)

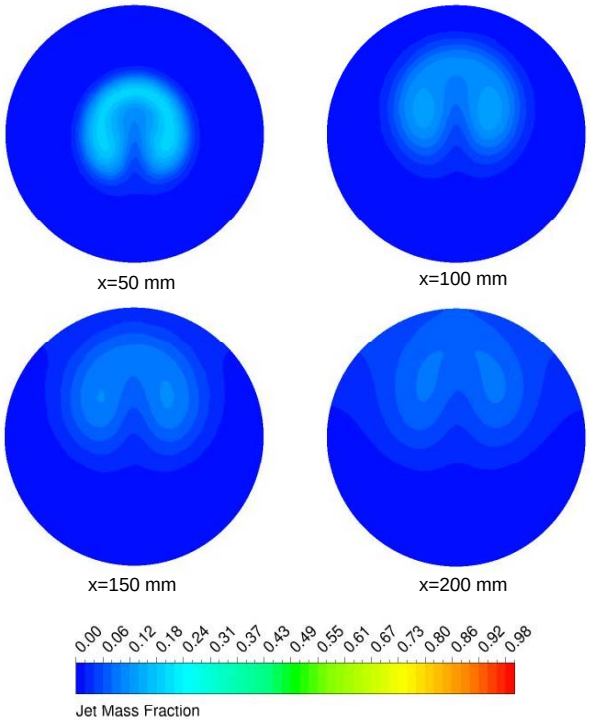

(b)

Figure 3.11: Contours of constant jet mass fraction $t = 15\,s$ (a) in the symmetry plane of the modeled reactor (i.e. the xy plane at $z = 0$) and (b) in cross-sections of the reactor 50, 100, 150, and 200 mm downstream from the jet inlet.

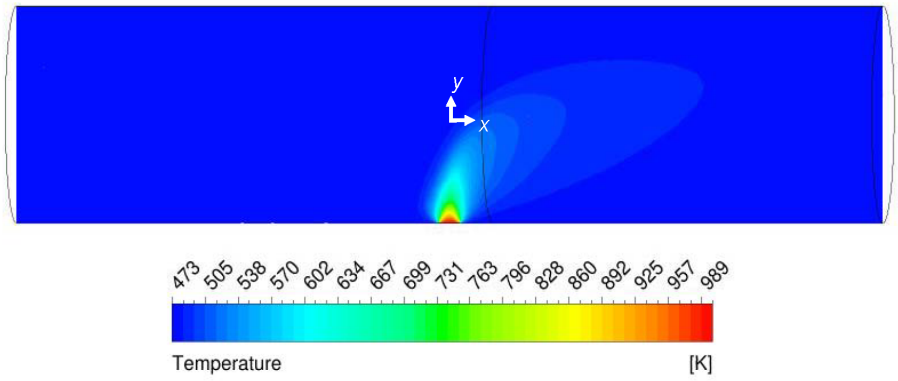

Figure 3.12: Contours of constant temperature in the symmetry plane at $15s$ into the transient simulation.

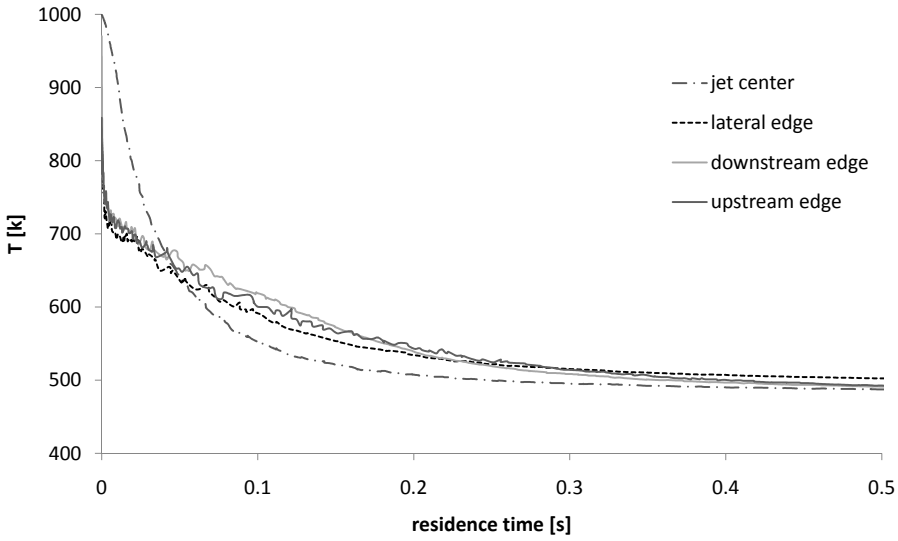

Figure 3.13: Temperature along a streamline originating at the center of the jet, and the upstream, downstream, and lateral edges of the jet.

vs residence residence time in Figure 3.13 for the first $0.5\,s$ of gas residence time along pathlines originating from the jet center, lateral most point, upstream point, and downstream point. The quench rates in the modeled reactor are generally higher than those in prior Zn nanoparticle aerosol reactors, which ranged from $400\,K/s$ to $10^6\,K/s$ [19–25], all of which reported nanoparticle production.

3.4 Conclusion

The results preceding numerical model indicate that a transverse jet reactor has good potential to balance the competing reactor design goals of directing Zn mass away from reactor walls, and achieving quench rates on the order of $10^4\,K/s$ and well mixed reactants. The model captured the counter-rotating vortex pair–the dominant feature of transverse jets. Therefore, an experimental reactor based on these modeling results was built. It is presented in detail in the following chapter.

Chapter 4

Experimental Method

4.1 Experimental Apparatus

4.1.1 The Reactor

The transverse jet reactor and instrumentation are depicted in schematic form in Figure 4.1. The reactor consists of five sections: the pre-heat zone, the evaporation zone (vertical section), the mixing zone, the reaction zone, and the cooling zone. The cross-flow, or the quenching mixture of Ar and H_2O, flows through the pre-heat zone and into the mixing zone. The jet Ar flows through the evaporation zone, where it entrains the evaporating Zn vapor, and into the mixing zone through a $7.6\,mm$ quartz tube. The origin of the coordinate system used to describe this reactor is defined as the center of the jet where it enters the mixing zone. Experiments are conducted in one of two configurations. In configuration A, the mixing zone is $0.23\,m$ long and the cooling zone is $0.29\,m$ long; in configuration B, the mixing zone is $0.29\,m$ long and the cooling zone is $0.23\,m$ long. The axial locations of the boundaries between the pre-heat, mixing, reaction, and cooling zones in the two configurations are listed in Table 4.1.

The purpose of the pre-heat zone is, first, to heat the quenching mixture of Ar and H_2O above the saturation temperature of H_2O and, second, to create a nearly uniform velocity profile at the inlet of the mixing zone. Steam is generated by passing water through $0.4\,m$ of $3\,mm$ o.d. copper tubing, heated by a tape heater to the set point for the pre-

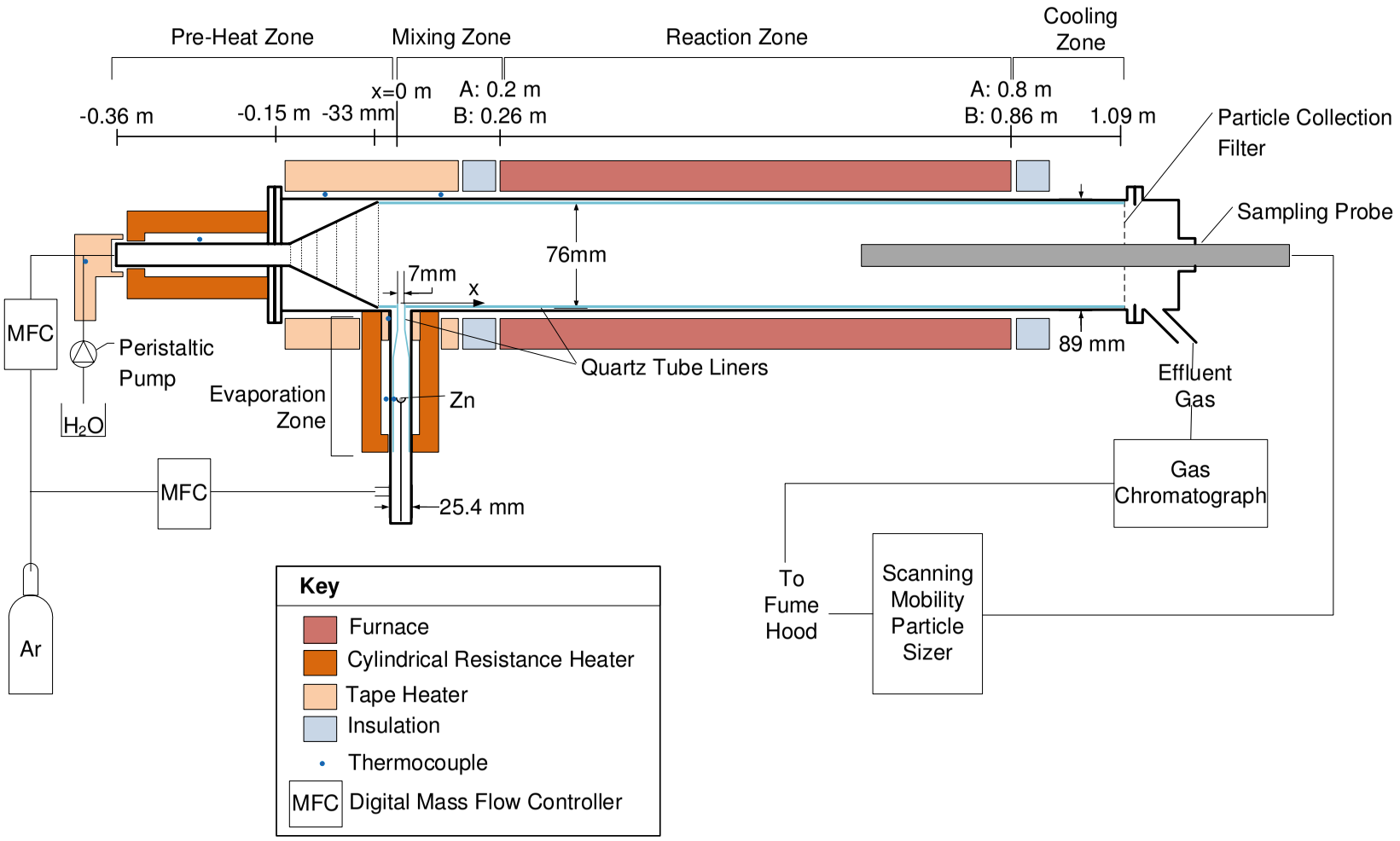

Figure 4.1: Schematic of the jet in cross-flow reactor (not to scale), including the pre-heat zone, mixing zone, Zn evaporation zone, reaction zone, and particle collection zone. Two experimental configurations, A and B, are used; their respective boundaries between the mixing, reaction and cooling zones indicated as A and B.

Table 4.1: Axial locations of the start and end of the mixing, reaction, and particle collection zones in configurations A and B.

	End of pre-heat/Start of Mixing Zone	End of Mixing/Start of Reaction Zone	End of Reaction/Start of Particle Collection Zone	Filter Location
A	$-0.033\,m$	$0.2\,m$	$0.8\,m$	$1.09\,m$
B	$-0.033\,m$	0.26	$0.86\,m$	$1.09\,m$

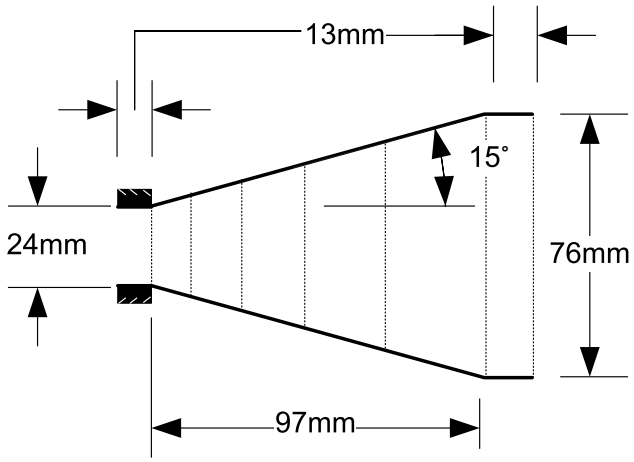

Figure 4.2: Schematic of the screen-filled wide angle diffuser.

heat zone, T_{PH} (generally $125°C$). Both the steam and argon enter the pre-heat pipe, a $25.4\,mm$ o.d. stainless steal tube, through a $6\,mm$ diameter opening. At $0.2\,m$, the pre-heat pipe is long enough to ensure that the Ar and H_2O jet has spread sufficiently to fill the pre-heat pipe before its exit [61]. The pre-heat pipe is heated to T_{PH} by a $152\,mm$ long cylindrical ceramic resistance heater. The final element of the pre-heat section is a screen-filled wide angle diffuser. The quenching mixture of Ar and H_2O flow from the pre-heat pipe into the diffuser, shown schematically in Figure 4.2. Due to the wide growth angle (15°), screens are used to avoid separation in the flow. The first screen in the diffuser (placed at the inlet) has a diameter of $23\,mm$ and the sixth screen, at the diffuser outlet $97\,mm$ downstream, has a diameter of $76\,mm$. A seventh screen, also with a diameter of $76\,mm$, is placed $13\,mm$ downstream from the last screen in the diffuser. Fluid dynamics simulations

of the diffuser predict that the velocity profile of the fluid exiting the seventh screen is very nearly uniform. See Appendix B for details on the design and modeling of the wide-angle screen-filled diffuser. The diffuser is housed inside an air-tight outer stainless steel tube. The outside wall is heated to a set temperature, T_1, with a tape heater (TH1 in Figure 4.3). The flow exits the seventh screen $33\,mm$ upstream of the evaporation zone jet inlet.

The evaporation zone consists of an outer, air-tight nickel alloy (Inconel 625) pipe (o.d. $= 25.4\,mm$ and i.d. $= 22\,mm$) and a fused quartz liner through which the carrier Ar and the evaporated Zn flows. The outer metal shell is designed to reduce oxygen leaks into the reactor, while the quartz liner enables observations of Zn deposition at the conclusion of an experiment. It is shown in greater detail in Figure 4.3. The majority of the quartz liner is $18\,mm$ i.d. ($20\,mm$ o.d.) until it tapers to $7\,mm$ i.d. ($9\,mm$ o.d.) just below where it enters the mixing zone. The Inconel tube consists of two parts: the upper part is welded to the stainless steal reactor shell and ends at $y = -0.4\,m$. The quartz liner ends at the same location ($y = -0.4\,m$). The lower part is 76 mm long and is sealed at the bottom ($y = -0.476\,m$). An ultra-torr vacuum fitting connects the two parts. The Zn is contained in a quartz crucible and held in the evaporation zone at $y = -0.19\,m$. Ar flows into the evaporation zone through a $6.3\,mm$ o.d. stainless steal tube located at $y = -0.466\,m$ ($10\,mm$ from the bottom). The Ar entrains the evaporating Zn as it flows past the crucible.The evaporation rate was measured for $750\,K \leq T_{EZ} \leq 1173\,K$ and Ar flow rates from $100\,mL/min$ to $1\,L/min$. The data showed no dependence on flow rate for $750\,K \leq T_{EZ} \leq 1100\,K$, and the temperature dependence is described by

$$\dot{m}_{Zn}(T) = 1.694 \times 10^{-8} \exp(0.01262 \cdot T_{EZ}) \tag{4.1}$$

See Appendix C for more details. A thermocouple located next to the crucible containing the evaporating Zn records the evaporation temperature. A second thermocouple on the outside of the outer Inconel wall is used to control the ceramic cylindrical heater, $305\,mm$ in length, which maintains the temperature in the evaporation zone. A tape heater (TH2 in Figure 4.3) is used to keep the wall temperature at the jet inlet, T_2, above $885\,K$ ($607°C$), as conduction from the evaporation zone to the cooler mixing zone walls would otherwise

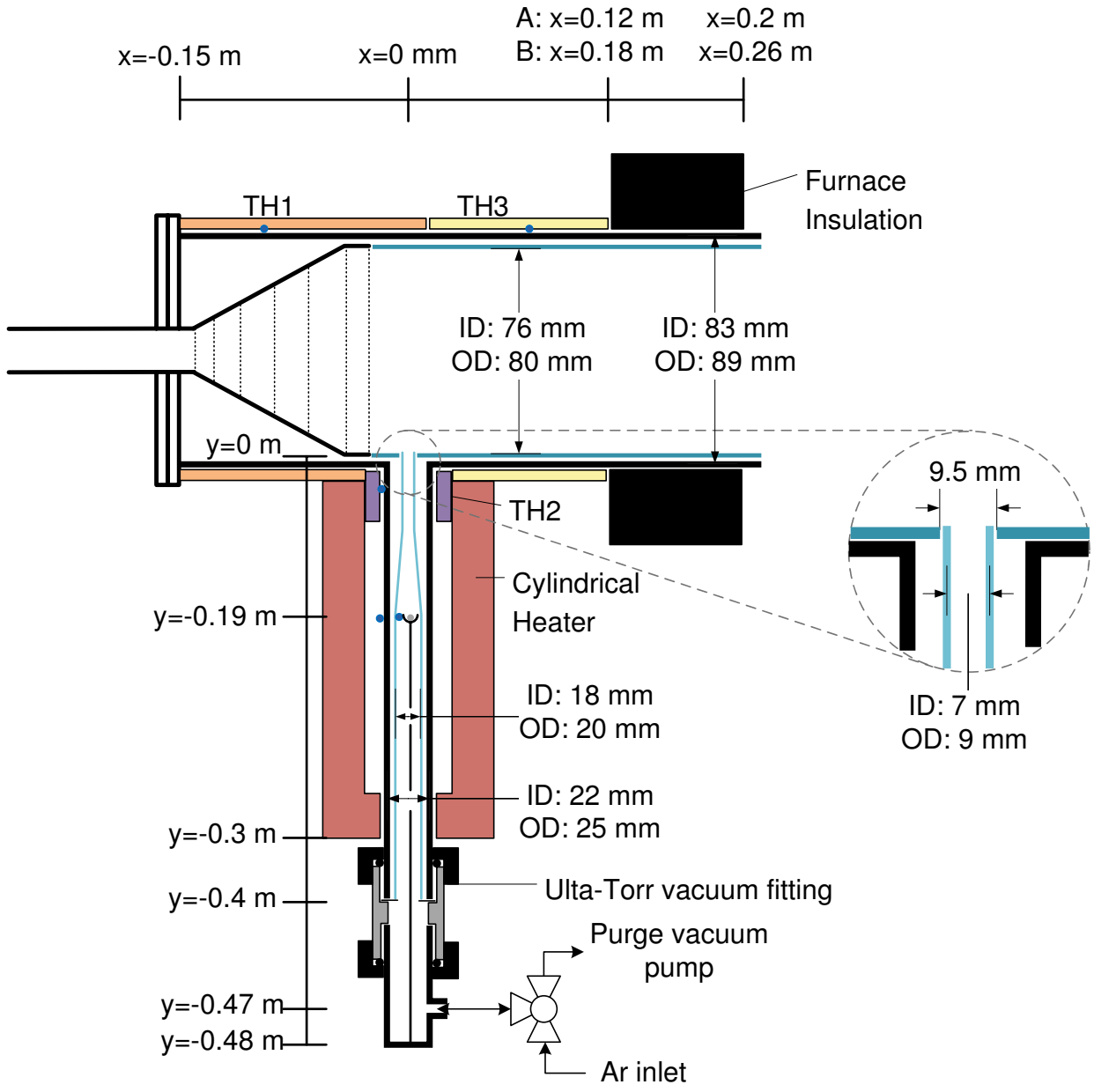

Figure 4.3: Detailed schematic of the mixing and evaporation zones (not to scale). The blue dots represent thermocouple junction locations, TH1 (orange) is the tape heater used to control the wall temperature around the diffuser in the pre-heat section, upstream of the jet entrance. TH2 (purple) is the tape heater used to control the jet inlet temperature. TH3 (yellow) is the tape heater used to control the wall temperature downstream of the jet entrance, in the mixing zone.

result in temperatures below the saturation temperature of Zn.

The mixing, reaction, and particle collection zones all consist of an outer, air-tight stainless steel shell ($89\,mm$ o.d., $83\,mm$ i.d.) and an inner fused quartz liner ($80\,mm$ o.d., $76\,mm$ i.d.). As in the evaporation zone, the combination of the steal outer shell with the quartz liner allows for vacuum tight seals while still enabling observations of deposits on the reactor walls. The mixing zone is the most novel, and in many respects the most important, part of the reactor—it is here that the transverse jet issues into the quenching cross-flow. The purpose of the mixing zone is achieve the rapid quench necessary for particle formation and to mix the reactants via the vortical structures of the transverse jet. In the mixing zone, the tip of the $7\,mm$ i.d., $9\,mm$ o.d. jet nozzle is situated inside a $9.5\,mm$ hole in the reactor quartz tube liner. The mixing zone is depicted in greater detail in Figure 4.3. The hot Ar and Zn jet enters into the quenching Ar and H_2O cross-flow and is rapidly cooled, initiating particle nucleation and growth. From the start of the mixing zone ($x = -33\,mm$) to $x = 0.12\,m$ in configuration A and $x = 0.2\,m$ in configuration B, the outer wall is well insulated. The wall temperature at $x = 70\,mm$, T_3, is monitored with a thermocouple, as shown in Figure 4.3. From $0.12 \leq x \leq 0.2\,m$ in configuration A and $0.2 \leq x \leq 0.28$ in configuration B, the mixing zone sits inside one of the insulated vestibule ends of the reaction zone furnace. These reactor vestibules hold the $89\,mm$ stainless steal shell in place in the reactor.

The reaction zone is so named because in this part of the reactor the aerosol is heated to temperatures desirable for Zn particle hydrolysis. It begins at the end of the insulated vestibule ($x = 0.2\,m$ in configuration A and $0.26\,m$ in configuration B) and is heated by a Carbolite HZS 12/600, three zone hinged tube furnace. The reaction zone ends at the start of the second insulated furnace vestibule ($x = 0.8\,m$ in configuration A and $0.86\,m$ in configuration B). The purpose of the cooling zone is to allow the aerosol to cool before particles are collected on the downstream filter, thereby avoiding further reaction of particles collected on the filter [44]. The walls of cooling zone are identical to the mixing reaction zones (stainless steal outer shell with a quartz liner), but instead of being heated, as in the reaction zone, the outer stainless steal shell is exposed to room temperature air. Particles are collected on a glass fiber filter placed $1.09\,m$ downstream from the jet entrance.

Experiments are defined primarily by the effective velocity ratio, R, the molar fraction of steam in the reactor, y_{H_2O}, and the average reaction zone temperature, T_{RZ}. In practice, R and y_{H_2O} depend on the flow rates of the Ar quench gas, the H_2O quench gas, and the Ar jet issuing from the evaporation zone, q_{Ar}, q_{H_2O}, and q_j, respectively. The flow rates of the q_{Ar}, q_{H_2O}, and q_j are controlled independently. Additionally, R depends on the density, and thus the temperature and composition, of the cross-flow and the jet. In calculating the effective velocity ratio for a given experiment, the temperatures of the cross-flow and the jet are assumed to be the set point temperature of the final section of pre-heat zone, T_1, and the set temperature of the evaporation zone, T_{EZ}, respectively. In almost every experiment, q_j is set to $0.35\,SLPM$, and q_{Ar} and q_{H_2O} are set to achieve the desired R and y_{H_2O} at the anticipated quench and jet gas temperatures. The nominal reaction zone temperature is defined as the average axial centerline temperature in the reaction zone. The reaction zone temperature depends primarily on the set temperature of the reactor furnace.

4.1.2 Control and Monitoring

All temperature measurements are carried out using Chromel Alumel (type K) thermocouples, and temperatures are monitored and recorded using National Instruments data acquisition and control chassis and modules (type SCXI) and a custom Labview program. A thermocouple is placed at the mid-point of each part of the pre-heat and mixing zones heated by a separate tape heater or ceramic heater. The wall temperatures under the three tape heaters are held at their set temperature by manually adjusting the voltage applied across the tape heater with a Variac auto-transformer. The temperatures in the evaporation zone and the pre-heat pipe, both of which are heated by ceramic resistance heaters, are controlled via a Labview subroutine that automatically turns each heater on or off (via solid state relays) when the measured temperature is below or above the set-point temperature, respectively. This method of temperature control results in an extremely stable temperature inside the evaporation zone, as measured by the thermocouple placed next to the crucible. The reaction zone is heated by a Carbolite HZS 12/600, three zone, hinged tube furnace. The three zones in the furnace are $0.15\,m$, $0.3\,m$, and $0.15\,m$ long, and are separately monitored via type

K thermocouples and controlled via a Carbolite 301 PID (proportional–integral–derivative) temperature controller. Temperatures in the outer, $0.15\,m$ long zones are set relative to the main, center zone. The flow rates of argon through the evaporation zone and the mixing zone are monitored and controlled using MKS digital mass flow controllers (MKS 1179A and 2159B). The mass flow meters are calibrated using a Gilibrator 2 calibration system (Synsodyne, Inc., accuracy of $\pm 1\%$). The flow rate of steam into the mixing zone is controlled with a peristaltic pump (Isamatec EW-78017, accuracy $0.1 \mu L/min$). The effluent gas is monitored for Nitrogen (N_2), oxygen (O_2) and H_2 using an in-line gas chromatograph (GC, Agilent 6890). The H_2 peak area is correlated to the H_2 molar fraction, y_{H_2}, using calibration samples with known H_2 concentrations. The uncertainty in GC measurements are dominated by scatter in the data—at the low Zn concentrations in this study, even maximum H_2 production would result in very small H_2 peaks in the GC. With the very small peaks, the scatter in measured peak area is significant. Mass is measured with a digital mass balance (Sartorius, accuracy $3 \times 10^{-4}\,g$).

4.1.3 Aerosol Sampling

Accurate sampling of the aerosol in-situ is a tremendous challenge. Because of the nature of the heated cylindrical reactor and the desire to sample at various axial locations, the sampling probe must enter the reactor from its end, and be moved axially in the reactor, rather than be inserted through the wall of the reactor. The ideal sampling probe would have no particle losses between when then sample is taken and when it reaches the nano-SMPS and would completely halt particle growth and reaction. The high temperatures and high anticipated concentrations of the aerosol ($\sim 10^8/cm^3$) make this is a difficult task to achieve. However, rapid dilution and cooling of the aerosol can be used to inhibit particle growth, further reaction, and losses to the probe wall.

I use an ejection dilution probe that can be moved axially in the reactor during experiments (shown in Figure 4.4). Ejection diluters operate by simultaneously drawing and diluting a sample from the aerosol. A dilution gas flows at high speed through a narrow annulus, resulting in a pressure drop that draws the aerosol sample in through the nozzle.

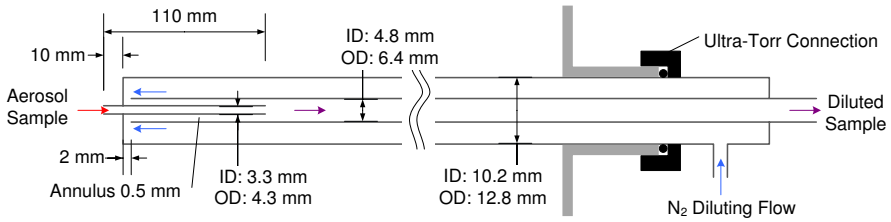

Figure 4.4: A schematic of the ejector diluter probe, which can be moved to different axial locations during the experiment.

The probe consists of three concentric stainless steel tubes—the innermost tube is $0.11\,m$ long with a $4.3\,mm$ o.d., the middle tube is $1.1\,m$ long with a $6.4\,mm$ o.d., and the outermost tube is $1\,m$ long with a $12.8\,mm$ o.d.. The diluting N_2 flows through the annulus between the outermost and middle sized pipes until it reaches the front end of the probe, where it bends around the middle pipe through a $2\,mm$ wide gap and then flows at high speed through the $0.5\,mm$ wide, $98\,mm$ long annulus between middle and the innermost tubes. The resulting pressure drop pulls aerosol through the innermost tube–it exits into the middle tube where it mixes with the diluting N_2. The diluted aerosol sample flows out of the reactor through the middle tube and is sent to the Scanning Mobility Particle Sizer (SMPS). Attached to the end of the reactor by an Ultra-Torr swage-lok fitting, the ejection diluter probe can be slid to different axial locations when the Ultra-torr fitting is loosened, and secured in place by tightening the fitting. A second dilution can be achieved as needed using a commercial ejection diluter positioned at the end of the probe, outside of the reactor. The precise dilution ratio is determined by measuring the N_2 composition (i.e. the dilution gas composition) in the gas exiting the probe using a Raman Laser Gas Analyzer (RLGA, $\pm 0.0025 \cdot measurement$). The probe has been verified with a known aerosol distribution for particles from $10\,nm$ to $200\,nm$. Calculations of expected penetration efficiencies in the probe inlet are over 98% for particles up to $1\,\mu m$. See Appendix D for more details on the verification of the probe and penetration efficiency calculations.

The SMPS consists of a Po-210 aerosol neutralizer, a nanoscale Differential Mobility Analyzer (DMA, laboratory made) and an ultrafine Condensation Particle Counter (CPC, TSI 3010). The DMA selectively sorts particles based on the the electrical mobility of the

particle. The mobility of a particle represents the balance of an electric force and drag force experienced by a particle in an electric field. The DMA consists of two concentric cylinders. An electric field is created by applying voltage to the inner cylinder while the outer cylinder is grounded. A sheath flow of clean air and the aerosol sample flow through the annular space between the cylinders. Particles are singly charged before entering the DMA where they experience the electric field. The electric field is controlled by changing the voltage applied to the center cylinder. At a given voltage, only particles of a given mobility exit the DMA, and the size of these particles is given in terms of an equivalent diameter–the diameter of a spherical particle of unit density with that mobility [62]. The SMPS scans through a range of voltages, allowing for sampling of particles with equivalent mobility diameters from $7\,nm$ to $230\,nm$. Thus, the SMPS provides data on particle size distribution and concentration. The sorted particles enter the CPC which counts the particles. As the aerosol enters the CPC, the flow is saturated with n-butyl alcohol. It is then cooled, leading to supersaturation that results in the alcohol condensing on the particles, causing them to grow to $\sim 10\,\mu m$ [62]. At this size, they can be counted optically based on light transmission or scattering [63]. The SMPS scans through a range of voltages, allowing for sampling of a range of particle mobilities, providing data on particle size distribution and concentration.

4.2 Experimental Method

At the start of each experiment, the masses of the quartz evaporation tube liner, crucible, Zn pellets (99% purity), and filter are recorded. Air is purged from the reactor by sealing the reactor and alternately using a vacuum to draw gas out of the reactor (to 10" Hg) and then refilling the reactor with Ar (to $3\,psi$). The cycle is repeated seven times before the jet and quench Ar flow rates are set to their nominal values and gas is allowed to flow through the reactor. The reactor pressure is held slightly above atmospheric ($\sim 1\,psi$) to impede infiltration of air into the reactor. The pre-heat, mixing, and reaction zone heaters are all turned on and temperatures in those zones are allowed to stabilize, a process that takes approximately 1.5 hr. The continuous flow of Ar through the reactor during this time serves

to sweep any remaining air out of the reactor. After the purging process, the GC measures no N_2 or O_2 in the effluent stream. Once the temperatures have stabilized, the evaporation zone heater is turned on. A wall temperature set point of $1003\,K$ ($730°C$) results in $T_{EZ} = 1000\,K$ ($727°C$). The evaporation rate at this temperature is $5.27 \times 10^{-3}\,g/min$. When the evaporation zone temperature reaches $1000\,K$, the peristaltic water pump is turned on and steam is added to the quenching flow.

The hydrogen content of the effluent gas is measured with the GC. The hydrogen production rate, $\dot{n}_{H_2}$ can be derived from the definition of y_{H_2}:

$$y_{H_2} = \frac{\dot{n}_{H_2}}{\dot{n}_{H_2} + \dot{n}_{Ar_2}} \tag{4.2}$$

where $\dot{n}_{Ar}$ is the molar flow rate of Ar. The maximum $\dot{n}_{H_2}$ possible is equal to $\dot{n}_{Zn}$, or the evaporation rate in moles. Thus, the instantaneous conversion, X', is

$$X' = \frac{\dot{n}_{H_2}}{\dot{n}_{Zn}} \tag{4.3}$$

and the overall conversion, X, is

$$X = \frac{\sum_{i=1}^{t_{final}} \dot{n}_{H_2,i} \Delta t_i}{n_{Zn,0}} \tag{4.4}$$

where $n_{Zn,0}$ is the total moles of evaporated Zn, Δt_i is the time step associated with the measured hydrogen production rate, and the numerator is the time-weighted sum of the hydrogen production rate. GC measurements are recorded every $1.3\,min$.

In aerosol sampling experiments, the aerosol is sampled with the ejection dilution probe (ED probe) and its size distribution and concentration are measured with the SPMS. As mentioned above, the dilution gas composition is monitored with an RLGA. Aerosol measurements are taken before the evaporation zone heater is turned on to ensure that the starting, baseline measurements in the reactor are zero. SMPS scans are taken continuously during the temperature ramp of of the evaporation zone. Once the evaporation zone reaches a steady temperature, several scans are taken to ensure that the measured distributions and concentration are steady with time. Next, the probe is moved to different sampling locations in the reactor by loosening the vacuum fitting that holds the probe in place and sliding the

probe in or out of the reactor. Because loosening the vacuum fitting changes the pressure in the reactor, which in turn affects the probe sampling rate and dilution ratio, SMPS scans at the new location are initiated only after the dilution gas composition returns to its steady value, as measured by the RLGA. At each location, several scans are taken (each containing an up and down scan of the DMA voltage range), again to ensure that steady behavior is being captured (or identify if the behavior is not steady).

Measured concentrations are converted to pre-dilution concentrations, N, by

$$N = N_d \frac{1}{1 - \frac{1}{f_{N_2}}} \tag{4.5}$$

where N_d is the diluted concentration (as measured by the SMPS) and f_{N_2} is the N_2 fraction of the gas by volume.

At the conclusion of each experiment, the masses of the evaporation tube, crucible, and filter are recorded. Kim wipes are used to clean the particles from the wall of the cooling zone and mixing zone. The mass of theses wipes are measured before and after cleaning to determine the approximate mass of the depositions in each section. Comparing the final and initial mass measurements, we get the total mass of Zn evaporated ($\Delta m_{crucible+Zn}$), the mass of any Zn that condensed on the evaporation tube wall (at its tip), the mass collected on the filter, and mass deposited on the walls of the mixing and cooling zones.

The success of the transverse jet reactor at reducing particle deposition on the wall of the reactor is best described by the yield, Y, defined as the fraction of the mass entering the reactor that reaches the filter or particle collection zone. Some Zn condenses on the tip of the evaporation tube, Δm_{tube}, and never enters the reactor. Thus, the yield is

$$Y = \frac{\Delta m_{filter} + \Delta m_{collection}}{\Delta m_{crucible+Zn} - \Delta m_{tube}} \tag{4.6}$$

Defined this way, the yield measures how well the flow field in the reactor delivers mass from the jet inlet to the filter.

4.2.1 X-Ray Diffractometry

The filter deposits are collected for analysis by XRD (Bruker-AXS D5005 Diffractometer) and scanning electron microscopy (Hitachi S- 900 FEG-SEM). To obtain accurate measure-

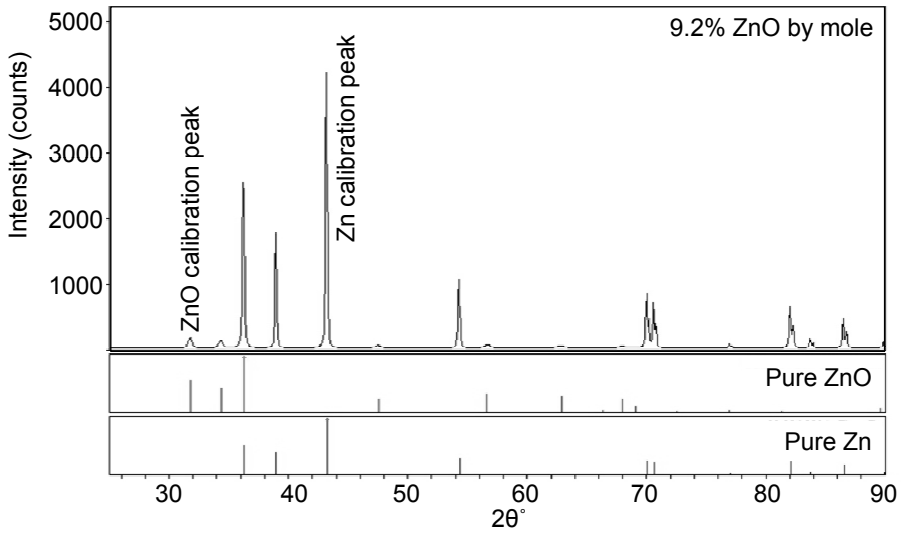

Figure 4.5: XRD spectrum for the calibration sample that is 9% ZnO by mole, compared to the pure Zn and ZnO spectra.

ments of ZnO at the low concentrations expected at the filter, we use the internal standard method [64] to calibrate the XRD using samples of known concentration. The primary Zn peak ($2\theta = 43.3°$) and the second largest ZnO peak ($2\theta = 31.8°$) of the XRD spectrum (see Figure 4.5) are used for the calibration because they are the largest peaks attributable solely to Zn and ZnO, respectively. The analysis is completed using long dwell times ($10\,s$) at each 2θ step to obtain high signal to noise ratios. This approach allows for clear detection of the ZnO peak even at very low concentrations ($> 1\%$). The calibration uses the ratio of the area under the ZnO peak to the area under the Zn peak. Peak area is chosen because it is relatively robust across most crystallite sizes.

The calibration samples are prepared in our laboratory by packed bed conversion of Zn particles created in the transverse jet aerosol reactor. These particles are generated in the transverse jet reactor without steam and are collected from the filter after the reactor has cooled. An initial XRD peak measurement is taken to ensure that there is no ZnO peak prior to oxidation. The mass of the calibration samples are recorded and then a sample is loaded into a packed bed reactor. With $300\,sccm$ of Ar flowing over the sample, the reactor temperature is allowed to stabilize at $623\,K$. At that point, the Ar flow is reduced to $150\,sccm$ and $150\,sccm$ of carbon dioxide, CO_2, is added to the flow. The molar

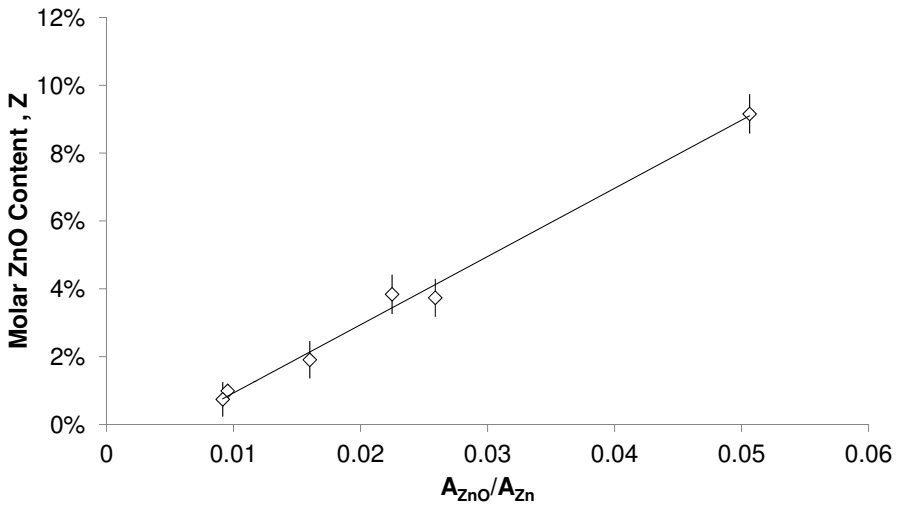

Figure 4.6: Calibration curve for quantitative XRD analysis of ZnO molar composition.

concentration of CO in the effluent gas is measured at $1\,s$ intervals using the RLGA. Due to the stoichiometry of the reaction ($Zn + CO_2 \longrightarrow ZnO + CO$), the molar production of ZnO is equal to the molar production of CO. Thus, the total molar conversion to ZnO is determined using equations 4.2-4.4, for CO instead of H_2. Carbon dioxide was used as the oxidizer in these experiments because we can obtain more accurate measurements of the flow rate of CO_2 than the flow rate of H_2O, and thus more accuracy in the conversion values. These calibration samples with known ZnO molar conversions were then analyzed via XRD as described above. The data and regression curve are shown inFigure 4.6. The resulting calibration is

$$Z = 201.14\frac{A_{ZnO}}{A_{An}} - 1.09 \tag{4.7}$$

where Z is the molar conversion in percent and the uncertainty in Z is $\pm 0.58\%$ (absolute). A_{ZnO} and A_{Zn} are are the areas under the ZnO peak and Zn peak, respectively. The calibration is for $0.5\% \leq Z \leq 10\%$. The internal standard method was chosen over the RIR and Rietveld methods because both of these more conventional peak-fitting methods over-predict the ZnO content of known samples. At the maximum level of refinement achieved using the Rietveld and RIR fitted patterns, the height and area of all peaks attributed exclusively to Zn are under-predicted. In fact, RIR and Rietveld predict $20 - 50\%$ ZnO in a calibration sample that is 10% ZnO (more details are provided in Appendix E).

Chapter 5

Assessing the Transverse Jet Reactor

5.1 Introduction

In Chapter 3, preliminary modeling results were presented indicating that the transverse jet reactor can achieve rapid quenching of the Zn vapor, well mixed reactants, and be used to maximize particle yields on the filter. In this chapter, the success of the transverse jet reactor at achieving these three objectives is demonstrated through a series of experiments and matching numerical models over $3.04 \leq R \leq 12.15$ for $y_{H_2O} = 0$ and 0.12. In this case, the domain and boundary conditions of the numerical models are chosen to closely approximate the experiments.

In addition to the three objectives that the transverse jet reactor is expected to address, a successful Zn aerosol hydrolysis reactor needs an average residence time long enough for complete conversion of Zn particles to ZnO. Unfortunately, accurately predicting the residence time needed for complete conversion is not possible, as our current understanding of the kinetics of Zn hydrolysis in an aerosol is limited (see Section 2.2.2). If used to estimate required residence times for complete conversion, the kinetic expressions derived via TGA predict that over $500\,min$ are needed. Even the times required for 10% conversion—$38\,s$ by Ernst et al. [13] and $94\,s$ by Funke et al. [24]—are very difficult to achieve in laboratory scale reactors. Average gas residence times in the transverse jet reactor range from $12\,s$ to $16\,s$ for the experiments discussed in this chapter. See Appendix F for the calculations used to

estimate residence times. These residence times are unlikely to be sufficient for complete or near complete conversion.

5.2 Method

5.2.1 Experimental Method

Experiments over a range of values of effective velocity ratios, R, were conducted to assess the hypothesis that R can be tuned to maximize reactor particle yield and that a high quench rate can be achieved in a transverse jet reactor, even at low Reynolds numbers ($172 \leq Re_D \leq 349$). Experiments were conducted without steam and with $y_{H_2O} \approx 0.12$. These experiments are listed in Table 5.1. The experimental apparatus and general experimental method are discussed in detail in Chapter 4.

All experiments are conducted in configuration A (see Figure6.1).. The temperatures in the pre-heating zone are set to $T_{PH} = 398K$ ($125°C$) and $T_1 = 423K$ ($150°C$). Because one objective of these experiments is to assess the effect of R on the filter yield, Y (Equation 4.6), the reaction zone furnace temperatures are set with the goal of maintaining the reaction zone temperature between $398K$ and $423K$, to reduce temperature gradient effects on particle trajectory. To that end, the primary, middle zone of the reaction zone furnace is set to $418K$ ($145°C$), with the upstream furnace zone set to $10K$ below the primary zone and the downstream zone set to $40K$ above the primary zone. The centerline temperature for flow rates matching experiment 4 gradually decreases from $435\,K$ to $383\,K$ over the length of the reaction zone, as shown in Figure 5.1 . The tape heater at the tip of the evaporation zone heats that area to $T_2 = 885K$ ($612°C$). The mixing zone wall temperature, T_3, is $485K$ ($212°C$) for all experiments. The temperature just downstream of the filter varies slightly by experiment, between $333 - 343K$ ($60 - 70°C$).

The jet flow rate (through the evaporation zone) is $0.35\,L/min$, STP in all but experiments 1 and 9, in which the flow rates were $1\,L/min$ and $0.25\,L/min$, respectively. The quench flow rate of Ar ranges from $10\,L/min$ to $19.1\,L/min$, STP to achieve different values of R. The flow rate of H_2O is set so that $y_{H_2O} \approx 0.12$ for each experiment with steam.

Table 5.1: Experimental Series 1: Effect of effective velocity ratio, R, on particle yield.

	R	y_{H_2O}	Ar quench flow rate $[L/min]$	jet flow rate $[L/min]$	$Re_{d_{jet}}$	$Re_{D_{quench}}$	y_{Zn} in evaporation zone	T_{sat}
1	12.15	0	15	1	90.1	258.7	1.93×10^{-3}	$780\,K$
2	6.38	0	10	0.35	31.5	172.5	5.5×10^{-3}	$827\,K$
3	5.81	0.12	10	0.35	31.5	183.1	5.5×10^{-3}	$827\,K$
4	4.91	0	13	0.35	31.5	224.2	5.5×10^{-3}	$827\,K$
5	4.49	0	14.2	0.35	31.5	244.9	5.5×10^{-3}	$827\,K$
6	4.50	0.11	13	0.35	31.5	236.7	5.5×10^{-3}	$827\,K$
7	4.25	0	15	0.35	31.5	258.7	5.5×10^{-3}	$827\,K$
8	4.24	0.12	13.7	0.35	31.5	250.8	5.5×10^{-3}	$827\,K$
9	3.04	0	15	0.25	22.5	258.7	7.69×10^{-3}	$843\,K$
10	3.04	0.12	19.1	0.35	31.5	349.6	5.5×10^{-3}	$827\,K$

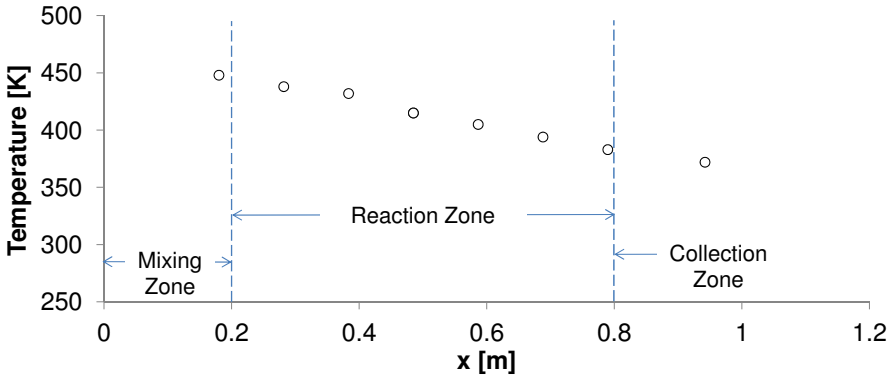

Figure 5.1: Centerline temperature measurements in the transverse jet reactor for conditions matching experiment 4.

At the expected evaporation rate of $5.27 \times 10^{-3}\, g/min$, the molar fraction of Zn, y_{Zn}, is 5.50×10^{-3} in the evaporation zone for experiments 2-8 and 10, corresponding to a saturation temperature, T_{sat}, of $827\, K$. Because of the different jet Ar flow rates in experiments 1 and 9, y_{Zn} and T_{sat} are different in those experiments—they are listed in Table 5.1. In the reactor, the molar fraction of Zn (in any phase) ranges from 8.79×10^{-5} to 1.65×10^{-4}. Approximately $0.5\, g$ of Zn is placed in the crucible at the start of each experiment and subsequently evaporated. No aerosol sampling is conducted in this set of experiments; the change in mass of the filter, the measured mass on the walls of the mixing, particle collection, and reaction zones, and the deposition patterns in the reactor are the primary results.

5.2.2 Numerical Method

A computational fluid dynamics model of the mixing zone aids in the evaluation and understanding of the reactor performance, especially the mixing of the reactants. In contrast to the numerical model described in Chapter 3, which was used in the design phase prior to building the reactor, the domain and boundary conditions in this model are set to closely approximate experimental conditions in the mixing zone of the transverse jet reactor. Experiments 3, 6, 8, and 10 are modeled, corresponding to $R = 5.81$, 4.50, 4.24, and 3.04, respectively. The modeling domain is depicted in Figure 5.2. It consists of a $76\, mm$ diameter, $163\, mm$ long cylinder (the mixing zone) and a $7\, mm$ diameter, $40\, mm$ long cylinder

(evaporation zone) that intersects the mixing zone cylinder $33\,mm$ downstream of the inlet to the mixing zone. This corresponds to the $33\,mm$ between the diffuser outlet and the jet inlet in the experimental reactor. The coordinate system origin is at the center of the jet inlet to the mixing zone. The quenching flow is assumed to enter the mixing zone with a uniform velocity profile, (as expected at the diffuser outlet) at a temperature of $423\,K$ (T_1). A uniform velocity profile is also assumed at the inlet of the evaporation zone, $40\,mm$ upstream of the jet inlet into the mixing zone. The entrance length (for fully developed laminar flow) is $13\,mm$ for all four experiments. The evaporation zone inlet temperature is set to $1050\,K$, while the evaporation wall temperature varies linearly from $1050\,K$ at $y = -40\,mm$ to $880\,K$ at $y = 0$, (where the jet enters the mixing zone). These temperatures correspond to measured gas and wall temperatures at $y = -40\,mm$ and $y = 0$ in the experimental reactor. The mixing zone wall temperature is assumed to be uniform at $485\,K$ (corresponding to the measured value of T_3). The mass flow rate at the mixing zone inlet inlet varies to correspond with physical experiments 3, 6, 8, and 10 (see Table 5.1). A wire-frame outline of the domain is shown in Figure 5.3, with planes and lines that will be used throughout the

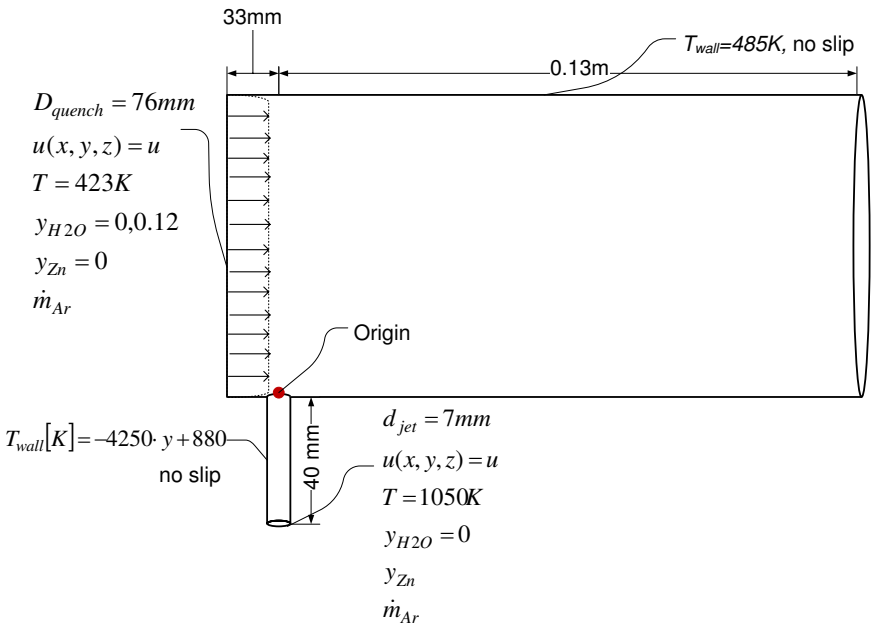

Figure 5.2: Schematic of the modeling domain for the transverse jet reactor, including boundary conditions.

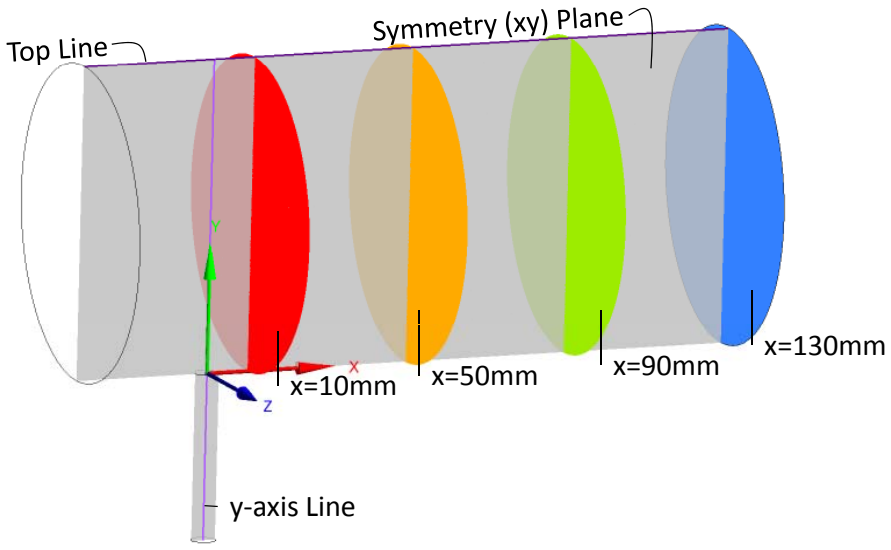

Figure 5.3: Modeling domain with coordinate system symbol located at the origin and lines and planes on which data will be presented in this chapter.

chapter to present data from the model—the plane of symmetry (on the xy-plane), yz-plane cross-sections of the reactor at $x = 10$, 50, 90, and 130 mm, the line running along the top of the reactor, and the line running through the center of the evaporation zone and above (the y-axis).

The steady, laminar, three-dimensional, and species transport models are applied to the governing conservation equations of mass, momentum, and energy [60]. The species transport model is used to model the mixing of Ar, H_2O, and Zn using the following diffusion coefficients, D, for species transport:

$$D_{H_2O \to Ar} = 1.467 \times 10^{-10} T^2 + 6.036 \times 10^{-8} T - 1.126 \times 10^{-5} \tag{5.1}$$

$$D_{Zn \to Ar} = 1.060 \times 10^{-10} T^2 + 3.474 \times 10^{-8} T - 7.203 \times 10^{-6} \tag{5.2}$$

$$D_{Zn \to H_2O} = 1.657 \times 10^{-10} T^2 - 8.397 \times 10^{-9} T + 1.653 \times 10^{-6} \tag{5.3}$$

where D is in units of $^{m^2}/_{s}$ and T is in K. These expressions for D are derived using the Chapman-Enskog theory for gaseous diffusion coefficients [65], and have $R^2 = 1$ for the temperature range $400\,K \leq T \leq 800\,K$. Particle nucleation is not modeled. Velocity and pressure are coupled using the SIMPLE algorithm. The solutions are considered converged

when the residual of continuity is less than 10^{-6}, the velocity residuals are less than 10^{-8}, the species residuals are less than 10^{-11}, and the energy residual is less than 10^{-9}.

5.3 Results

5.3.1 Effective Velocity Ratio and Particle Yield

In this section, the hypothesis that jet trajectory can be tuned via the effective velocity ratio, R, to maximize particle yields on the filter is assessed experimentally and through numerical models. In general, the trajectory of transverse jets are strongly dependent on R—a higher value of R corresponds to a jet with a higher kinetic energy relative to the cross-flow. Thus, increases in R will result in jets that penetrate farther into the cross stream before being deflected. This effect of R on jet trajectory can be seen in the contours of constant Zn molar fraction—all Zn comes from the evaporation zone, so Zn is a good indicator of jet trajectory. These contours of constant Zn molar faction can be seen in Figure 5.4 in the plane of symmetry (xy-plane) in the numerical models corresponding to experiments 3, 6, 8, and 10. The jet in experiment 3, with the largest shown value of R (5.81) penetrates farthest into the mixing zone before being deflected, while the jet in experiment 10, with the lowest value of R (3.04) penetrates the least before being deflected. Particle nucleation and growth is not modeled, so Zn remains in the vapor phase throughout the modeling domain. However, the molar fraction of Zn is a reasonable indicator of the location of Zn mass in the experiments, despite the difference in phase. The model of experiment 10 indicates that Zn will be near the lower portion of the reactor wall, so significant deposition is likely in that region. Similarly, in the model of experiment 3 shows Zn approaching the upper part of the reactor wall, indicating that Zn is likely to deposit there. In contrast, the jets in experiments 6 and 8 flow down the center of the reactor, which should result in reduced particle deposition on the reactor walls at $R = 4.24$ to 4.5.

The yield, Y, is the fraction of mass entering the reactor that is collected on the downstream filter or from the walls of the cooling zone (see Equation 4.6). It is the most direct measure of how well the reactor meets the goal of reduced deposition on the walls. Table 5.2

Table 5.2: Experimental Series 1: Effect of R on particle yield. Listed uncertainties are absolute uncertainty in calculated percentage.

	R	y_{H_2O}	Yield (±0.5%)	% Loss in Evaporation Tube (±5%)	Mixing Zone, Lower Wall (±1%)	Mixing Zone, Upper Wall (±1%)	Collection Zone Wall Deposits (±1%)
1	12.15	0	8.5	4.0	< 1	57.1	< 1
2	6.38	0	27.5	22.8	< 1	13.5	1.3
3	5.81	0.12	70.8	30.4	< 1	2.5	< 1
4	4.91	0	68.3	29.2	< 1	< 1	< 1
5	4.49	0	84.2	31.5	< 1	< 1	< 1
6	4.50	0.11	93.1	31.2	< 1	< 1	< 1
7	4.25	0	79.3	22.2	< 1	< 1	< 1
8	4.24	0.12	91.9	32.9	< 1	< 1	< 1
9	3.04	0	69.2	43.4	2.3	< 1	< 1
10	3.04	0.12	32.8	31.2	38.0	< 1	< 1

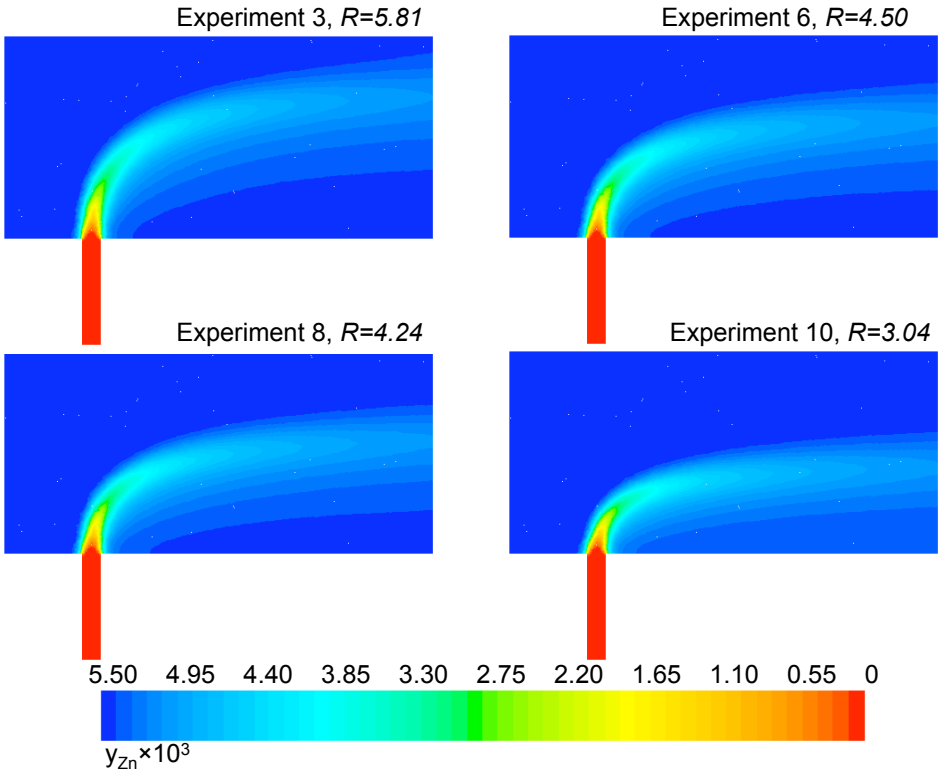

Figure 5.4: Contours of constant Zn molar fraction in the plane of symmetry for numerical models corresponding to experiments 3, 6, 8, and 10.

lists the yield, Y, and the fraction of the total evaporated mass that is measured from the following locations: condensed on the tip of the evaporation tube, deposited on the bottom of the mixing zone immediately after the jet inlet, deposited in all other parts of the mixing zone wall (primarily the upper part of the wall), and deposited on the cooling zone wall. In addition, Y is plotted against R for all experiments in Figure 5.5. As predicted from the contour plots from the numerical models, the yields are maximized at $4.24 < R < 4.50$ in the transverse jet reactor. In these four experiments, Y is between 79.3% (experiment 7, $R = 4.25$) and 93.1% (experiment 6, $R = 4.50$). At lower values of R, the yields drop precipitously, as more mass is lost in the region surrounding and immediately after the jet inlet, on the lower part of the mixing zone wall (see Table 5.2 and Figure 5.5). Conversely, as R increases beyond 5, more mass is deposited on the upper portion of the mixing zone walls, also seen in the data in Table 5.2. At $R < 5$, the fraction of total evaporated mass

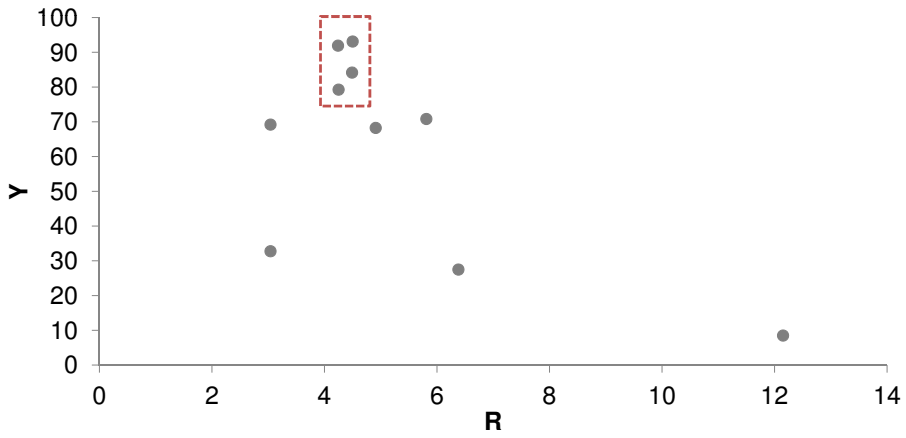

Figure 5.5: Yield, Y, vs. effective velocity ratio, R, for all experiments. Y is maximized at $4.24 \leq R \leq 4.50$ (dashed box).

that is deposited on the upper part of the mixing wall is always $< 1\%$; above $R = 5$, the mass deposited there increases rapidly from 2.5% for $R = 5.81$ to 13.5% for $R = 6.38$, and finally 57.1% for $R = 12.15$. Thus, the effective velocity ratio in a transverse jet reactor can be tuned to maximize particle yield on the filter. Indeed, at the optimized value of $R = 4.5$, over 90% of the mass that entered the reactor reached the filter.

The impact length, l_i, or the length at which deposition begins on the upper wall of the reactor, can be used to compare the flow field in the transverse jet reactor to the generalized scaling law for transverse jets developed by Muppidi and Mahesh [56] (see Section 3.1 for more details on the generalized scaling law). On the upper part of the mixing zone wall, the observable deposition begins gradually, making precise measurements of l_i difficult. Thus, two lengths were recorded—the length at which deposition was initially visible and the length at which deposition became opaque. The average value is reported with uncertainty that covers the range between the two measurements.

For most experiments, deposition begins between between $x = 30$ and $140\,mm$. The two exceptions are experiment 1, in which the majority of mass was deposited from $x = -23\,mm$ to $50\,mm$, directly above the jet inlet, and experiment 10, in which the characteristic deposition on the top did not occur. In the case of experiment 1, the effective velocity ratio was so high that the jet impinged directly on the opposite side of the mixing zone tube,

Table 5.3: Measured and predicted scaling law impact lengths for experiments with varying R and y_{H_2O}, all in mm. No reported value (–) for the model data indicates that y_{ZnO} did not reach the indicated level before the end of the modeling domain.

	R	y_{H_2O}	Measured	Scaling Law
1	12.15	0	-12 ± 12	6
2	6.38	0	43 ± 12.5	40
3	5.81	0.12	53 ± 17.5	53
4	4.91	0	115 ± 15	89
5	4.49	0	125 ± 15	118
6	4.50	0.11	125 ± 25	117
7	4.25	0	135 ± 15	139
8	4.24	0.12	135 ± 15	140
9	3.04	0.12	170 ± 15	388
10	3.04	0.12	none	388

depositing 57% of the evaporated mass in upper portion of the mixing zone. In the case of experiment 10, the effective velocity ratio was the lowest value studied—3.04—resulting in a faster bend in the jet trajectory. In addition, a significant portion of the mass (38%) was deposited immediately around and after the jet inlet, resulting in less total mass in the aerosol in this experiment. For all other experiments, impact length, l_i, or the axial distance between the jet inlet and the start of the depositions on the top of the tube, increases with decreasing R (see Table 5.3). The jets in experiments with higher values of R penetrate farther into the reactor before bending in the direction of the cross-flow. Thus, the particulate Zn reaches the upper wall of the reactor sooner, resulting in a shorter impact length than in experiments with lower values of R. Thus, this result is qualitatively consistent with the expected behavior of the transverse jet reactor.

Quantitative comparisons can be made between the experimental impact lengths and those predicted by the generalized scaling law in Muppidi and Mahesh [56]. The impact length, l_i, predicted by the generalized scaling law for jet trajectory (equation 3.3) is taken to be the value of x when $y = D = 76\,mm$. Equation 3.3 can be re-arranged to get l_i as a

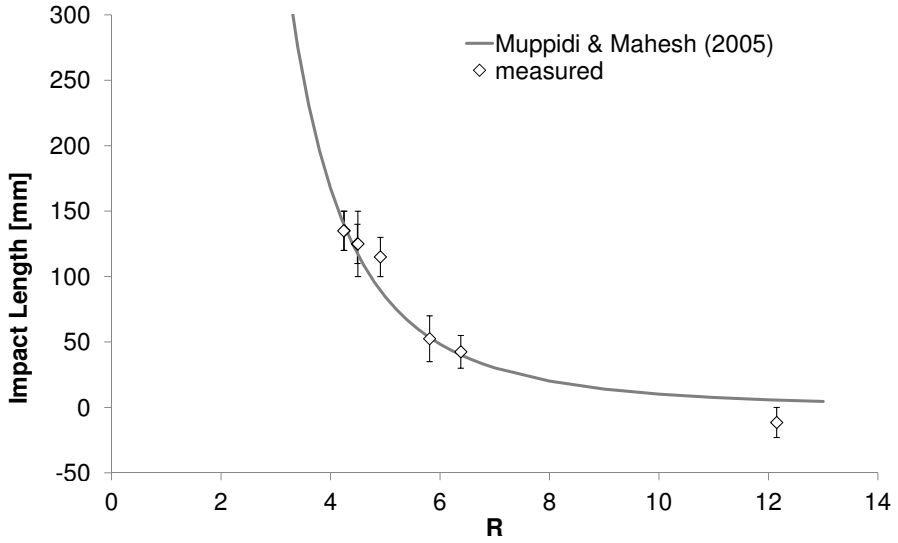

Figure 5.6: Predicted and measured jet impact lengths for the transverse jet reactor.

function of R:

$$l_i = Rd_j \left[\frac{D}{A' R d_j} \left(\frac{h}{d_j} \right)^{-0.15} \right]^{1/0.32} \tag{5.4}$$

The experimentally measured impact lengths are plotted with predicted impact lengths as a function of R in Figure 5.6. There is good agreement between the measured and predicted impact lengths. This agreement shows that tuning R in the transverse jet reactor has the expected effect on the jet trajectory and supports the conclusion that the transverse jet offers a measure of predictable control over the flow field in the reactor. Comparisons between experimental observations and numerical model data can be found in Appendix G. Because maximum yields are obtained with $R = 4.50$, the discussion on the quench rate (Section 5.3.2) and mixing of the reactants (Section 5.3.3) will be based primarily, though not exclusively, on results from experiment 6 and the corresponding numerical model.

5.3.2 Quench Rate

A rapid quench of the Zn vapor—a prerequisite for the formation of small particles—is a major objective of the transverse jet reactor. The gas temperature along the centerline of the evaporation tube extended up along the reactor diameter (the y-axis, as shown in Figure 5.3) is measured experimentally and predicted in the numerical model. These measured and

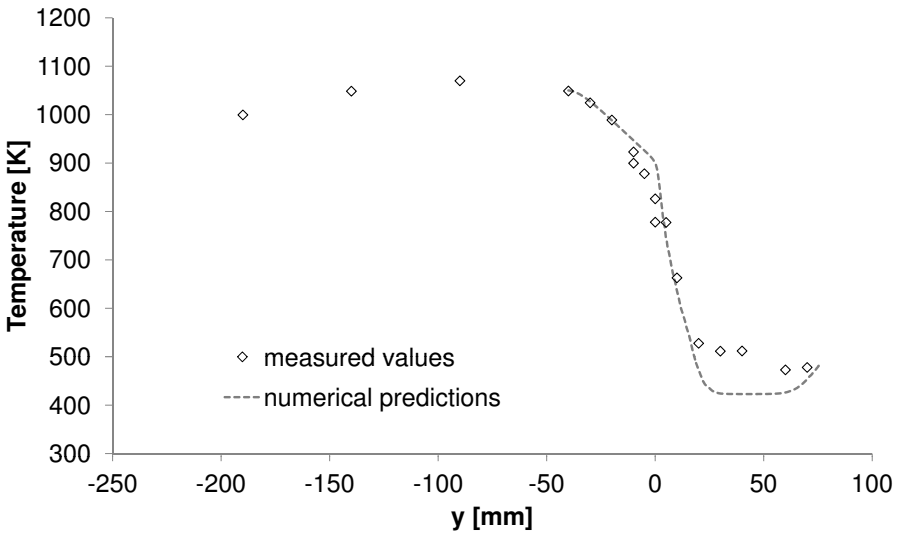

Figure 5.7: Measured and numerically predicted temperatures along the line $x = z = 0$—the centerline of the evaporation tube extended up along the reactor diameter.

predicted temperatures are shown in Figure 5.7. The elbow in the predicted temperatures at $y = 0$ is a product of the discontinuity in the wall boundary conditions used in the numerical model (i.e. the evaporation zone wall temperature reaches $880\,K$ at $y = 0$, while the mixing zone wall temperature is assumed to be $485\,K$ at all locations). The higher measured gas temperatures in the mixing zone, where the gas temperatures level off at $\sim 500\,K$, indicates that the quench gas in the reactor was at a higher temperature than was modeled. Overall, there is very good agreement between the predicted and measured temperatures; the numerical and experimental results both show that the temperature drops from $1050\,K$ at $y = -40\,mm$ to just below $530\,K$ at $y \approx 20\,mm$.

Nanoparticle formation is expected when the temperature of the Zn vapor rapidly falls below its saturation temperature at rates on the order of 10^3 to $10^4\,K/s$ [28, 30]. At the expected molar concentration of Zn in the evaporation zone ($y_{Zn} = 5.5 \times 10^{-3}$), the saturation temperature is $827\,K$. The relationship between saturation temperature, T_{sat}, and the partial pressure of Zn, P_{Zn}, is

$$\log P_{Zn} = -20.3143 - \frac{4636.2}{T_{sat}} + \frac{10.073}{\log T_{sat}} - 3.8085 \times 10^{-3} T_{sat} + 4.886 \times 10^{-7} T_{sat}^2 \qquad (5.5)$$

Isotherms are shown in Figure 5.8 for the symmetry plane in the model corresponding to

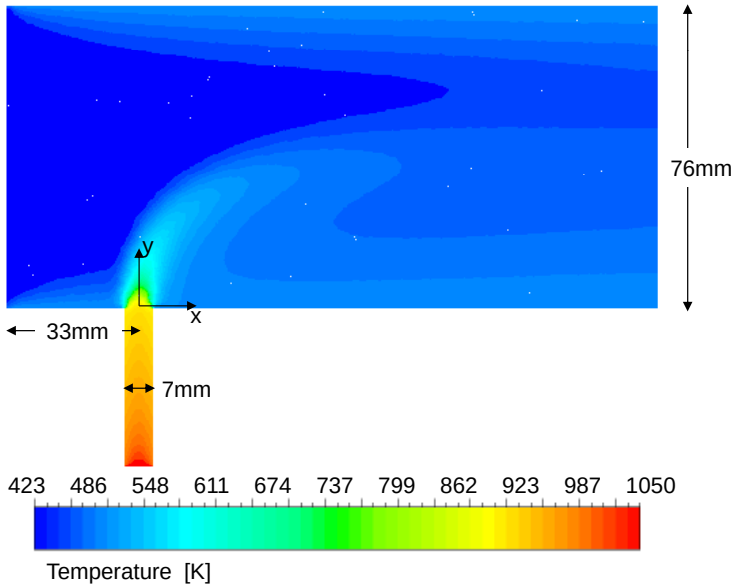

Figure 5.8: Numerical model isotherms in the plane of symmetry for experiment 6.

experiment 6. Qualitatively, Figure 5.8 illustrates the steep temperature gradients near the jet inlet. The quench rate can be quantified via temperature data along pathlines originating at the jet inlet. The agreement between the experimental data and modeled temperature along the y-axis indicates that using modeled data for temperature vs. residence times along jet pathlines should be relatively accurate. Temperature is plotted versus pathline residence time for a pathline originating at the center of the evaporation zone inlet (Figure 5.9). In the evaporation zone, the temperature decreases gradually from $1050\,K$ at the domain inlet to approximately $880\,K$ as it enters the mixing zone. At this point, the rate of temperature change increases sharply, as can be seen in Figure 5.9, so $880\,K$ is used as the initial temperature in calculating the quench rate, with the second temperature is the temperature on the pathline $10\,ms$ later:

$$\frac{\Delta T}{\Delta t} = \frac{880\,K - T_{10ms}}{10\,ms} \tag{5.6}$$

These two points are indicated with open circles in Figure 5.9. The average quench rate is $2.08 \times 10^4\,K/s$ in experiment 6. Using the same method to calculate quench rates based on streamlines originating elsewhere in the evaporation zone inlet, including lateral, upstream, and downstream the edges and points in between, results in quench rates that vary by less

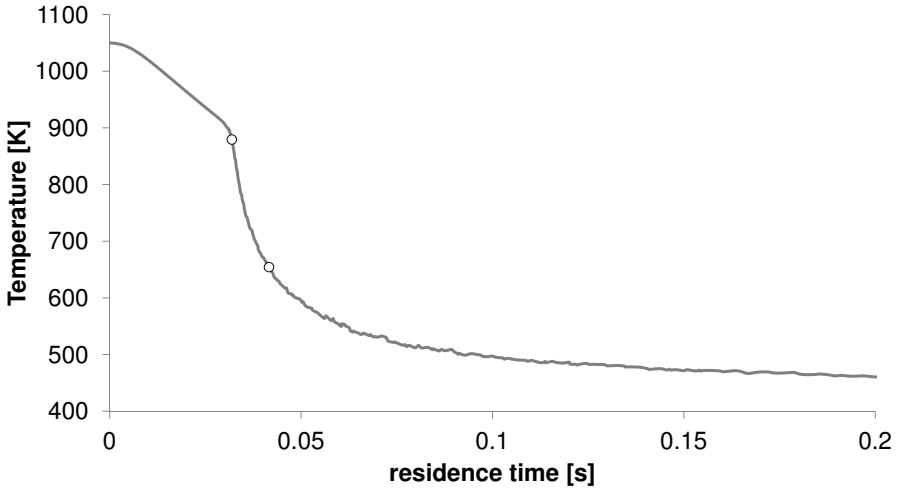

Figure 5.9: Modeled temperature along a streamline originating from the center of the evaporation zone inlet. The average quench rate is calculated as $^{\Delta T}/_{\Delta t}$ over the two points represented by open circles.

than $\pm 10\%$. In addition, the average quench rate does not vary significantly over the range of R studied numerically. The average quench rates predicted by the numerical model are $2.06 \times 10^4\, K/s$, $2.10 \times 10^4\, K/s$, and $2.00 \times 10^4\, K/s$ for experiments 3, 8 and 10, respectively.

5.3.3 Mixing in the Reactor

The modeled mass fraction of H_2O in the reactor is the best indicator of mixing between the Zn in the jet and H_2O in the quenching gas. Contours of constant molar fraction of H_2O for the model corresponding to experiment 6 are shown on (a) the symmetry plane and (b) cross-sections of the reactor at axial locations 10, 50, 90, and $130\, mm$ downstream of the jet inlet in Figure 5.10. The quench gas enters the domain with $y_{H_2O} = 12\%$, and the jet enters the reactor with $y_{H_2O} = 0$; by $x = 10\, mm$, $y_{H_2O} \geq 7.9\%$ for all locations in that plane. Thus, only $10\, mm$ after the jet enters the reactor, the concentration of H_2O at all locations in that plane and at greater axial locations is at least 66% of its maximum value. At $x = 130\, mm$, the outlet of the modeled domain, the minimum y_{H_2O} value is 11.3%—94.2% of the maximum value of y_{H_2O} anywhere in the reactor. Thus, the reactants are expected to be well mixed in the transverse jet reactor.

Mixing is driven primarily by the CRVP, which entrains cross-flow gas as it forms and

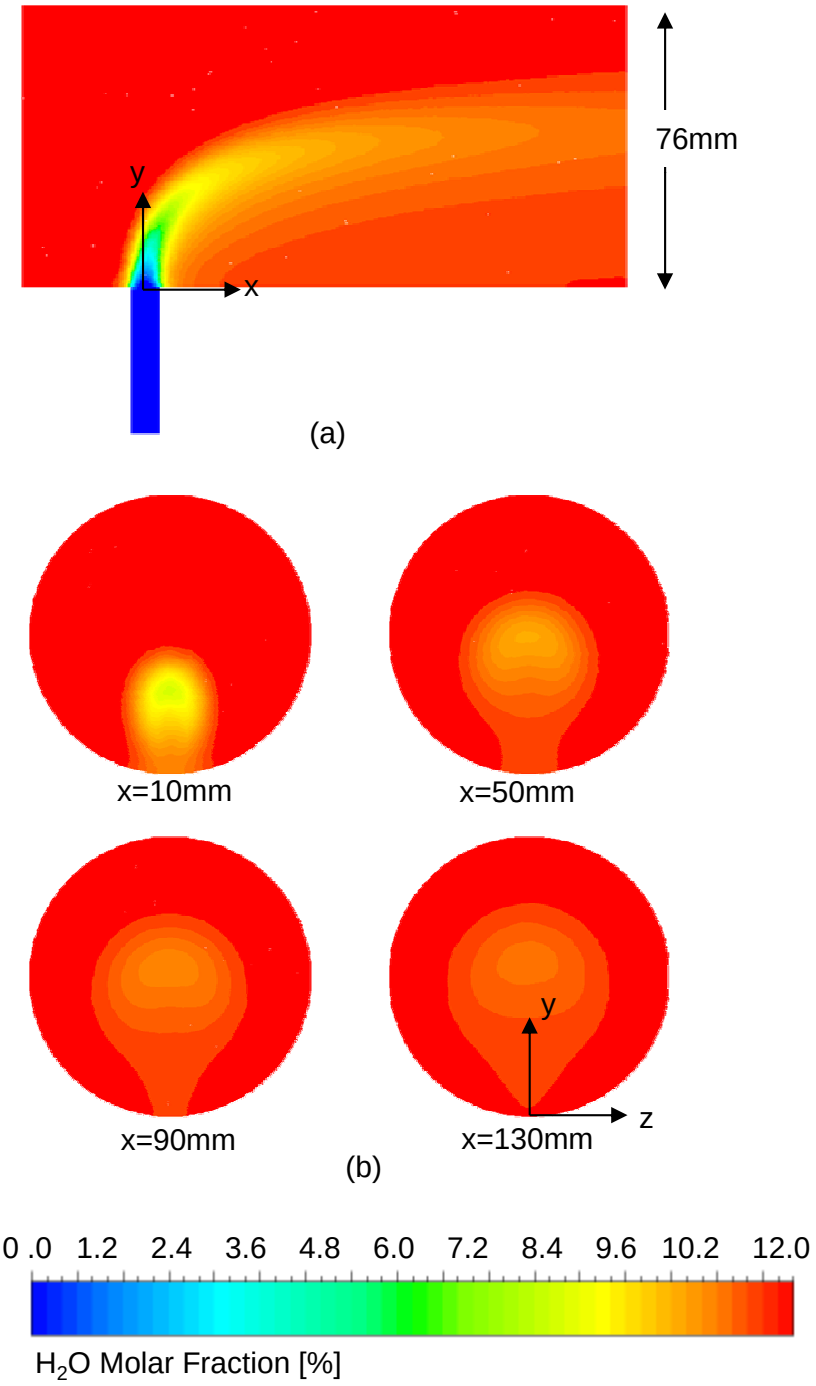

Figure 5.10: Contours of constant molar fraction of H_2O (a) in the symmetry plane of the modeled reactor (i.e. the xy plane at $z = 0$) and (b) in cross-sections of the reactor 30, 50, 90, and 130 mm downstream from the jet inlet.

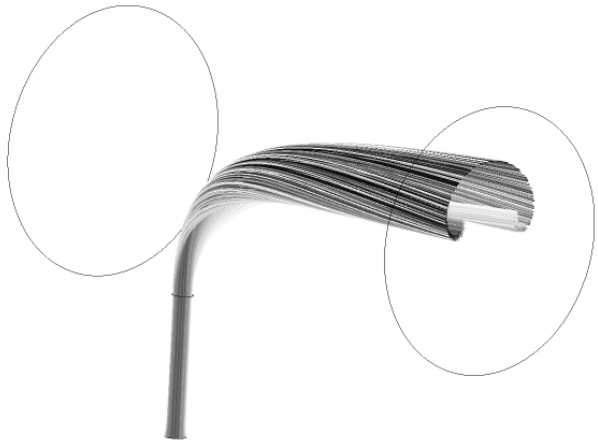

(a)

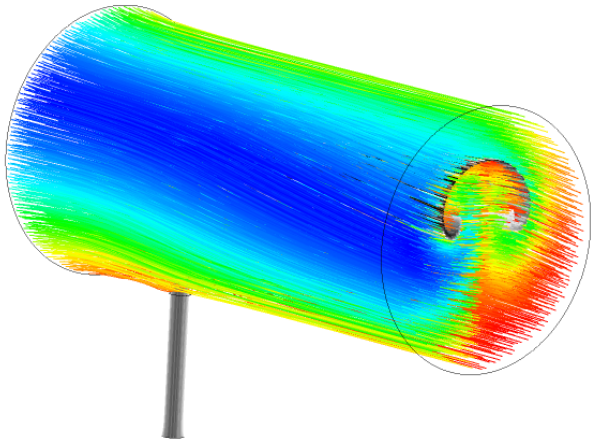

(b)

Figure 5.11: (a) Pathlines originating from the jet inlet only and (b) pathlines originating from the jet inlet (gray-scale) and cross-flow inlet (rainbow) in the numerical model.

develops in the reactor. Figure 5.11(a) shows pathlines originating from the jet inlet only, while Figure 5.11(b) shows pathlines originating from both the jet (gray-scale) and the quenching cross-flow inlet (rainbow) for the model corresponding to experiment 6. As the cross-section of the jet changes from a circle at the inlet, to a kidney shape as it bends, to finally the characteristic counter rotating swirl, it pulls gas from the quenching cross-flow into the swirl, thereby reducing the length scale, and thus the time scale, for mass diffusion. The counter rotating vortex pair can be seen in the swirling pattern of the jet pathlines. The entrained cross-flow gas is evidenced by the cross-flow pathlines inside and surrounding the

jet pathlines. As in the model presented in Chapter 3, the smaller scale vortical structures common to all transverse jets–the jet shear layer vortices, the horseshoe vortex, and the wall vortices–are not captured in this simulation. They can be expected to further increase mixing in the transverse jet reactor.

5.4 Conclusion

In past Zn aerosol reactors that combined particle nucleation with hydrolysis, there has been a trade-off between high quench rates and long residence times, and significant fractions of the Zn mass has been deposited on the walls of the reactors (see Section 2.1). The transverse jet reactor succeeds at achieving quench rates on the order of $10^4\,K/s$ and at thoroughly mixing the reactants at $Re_D = 236$ and with residence times as long as any in previous studies. The vortical structures inherent in transverse jets, especially the CRVP, drive mixing in the jet, while characteristically laminar flow persists near the wall. Furthermore, effective velocity ratio allows for a measure of control over the flow field, specifically the trajectory of the jet. Thus, particle yields can be optimized—as much as 90% of the mass that entered the reactor reached the downstream filter in the present study.

Chapter 6

Hydrolysis in the Transverse Jet Reactor

6.1 Introduction

Much attention has been given to Zn nano-scale reacting aerosols because, in theory, they promise fast kinetics and a continuous, controllable process. However, success of this approach depends on achieving high particle yields and high Zn conversion in the aerosol, neither of which have yet been achieved. To date, no set of experimental parameters in any reactor have achieved filter yields over 50% or aerosol conversions over 34% (by RIR peak fitting method for XRD). Furthermore, no single experiment has achieved filter yields *and* aerosol conversions that are both over 25%.

There are three potential mechanisms for H_2 production in the aerosol reactor. At low temperatures, a $Zn(OH)_2$ reaction has been observed for $70\,nm$ particles [17]. At higher temperatures, Zn particles can react directly with steam in either a fast, surface reaction, or a much slower, diffusion limited reaction [13]. Finally, if some Zn remains in the vapor phase in the aerosol reactor, it could react with steam on the surface of aerosol particles in via heterogeneous Zn vapor hydrolysis [18]. All three mechanisms are discussed in more detail in Chapter 2.

In this chapter, I present results from experiments conducted at temperatures from

$418\,K$ to $713\,K$ with and without steam in the transverse jet reactor, which was designed to balance the competing goals of high filter yields, high quench rates, and long residence times. The reactor is shown in Figure 6.1 which is identical to Figure 4.1, and re-printed here for ease of reference. Experiments were designed to determine the mechanisms that dominate particle growth and hydrolysis in the reactor, and the effect that hydrolysis has on particle morphology and filter yield—see Table 6.1. All experiments were conducted at $R \simeq 4.5$. First, experiments are conducted at $418\,K$ (A and B), a temperature favorable for the low temperature production of $Zn(OH)_2$. No evidence of such a reaction is found. However, there is some evidence that a thin ZnO layer forms on the surface of particles, even at these low temperatures. The rest of the experiments are conducted at temperatures where ZnO production by Zn hydrolysis has been observed in aerosol reactors and TGA studies: above $573\,K$. At these temperatures, particles can either react directly with steam or serve as a surface on which heterogeneous Zn vapor hydrolysis can occur. Of course, the heterogeneous vapor reaction can only occur if Zn vapor is present.

It is not possible to accurately quantify P_{Zn} in the reactor, as much of the Zn is in particle form. However, qualitatively, it is expected that if some of the Zn has not condensed before entering the heated reaction zone, it will remain in the vapor phase if $P_{Zn,eq}$ at T_{RZ} is greater than the local P_{Zn}. Furthermore, in the absence of something to impede particle re-evaporation (e.g. a ZnO layer), Zn particles that form in the mixing zone will have a tendency to re-evaporate in the reaction zone until equilibrium is reached, and the fraction of Zn mass that evaporates before reaching equilibrium depends on the reaction zone temperature. Though the actual P_{Zn} in the reaction zone is unknown, we can compare $P_{Zn,eq}$ to $P_{Zn,total}$, the Zn partial pressure assuming all the Zn in the reactor is vapor. For $T_{Rz} < T_{sat}$, the ratio of $P_{Zn,eq}$ and $P_{Zn,total}$ is the fraction of the total Zn mass that would be vapor at equilibrium, $mf_{Zn(v),eq}$:

$$mf_{Zn(v),eq} = \frac{P_{Zn,eq}}{P_{Zn,total}} \tag{6.1}$$

In all experiments, $P_{Zn,total} = 9.1 \times 10^{-5}\,atm$, corresponding to $T_{sat} = 665\,K$. The relationship between temperature and Zn partial pressure is described by Equation 5.5. When

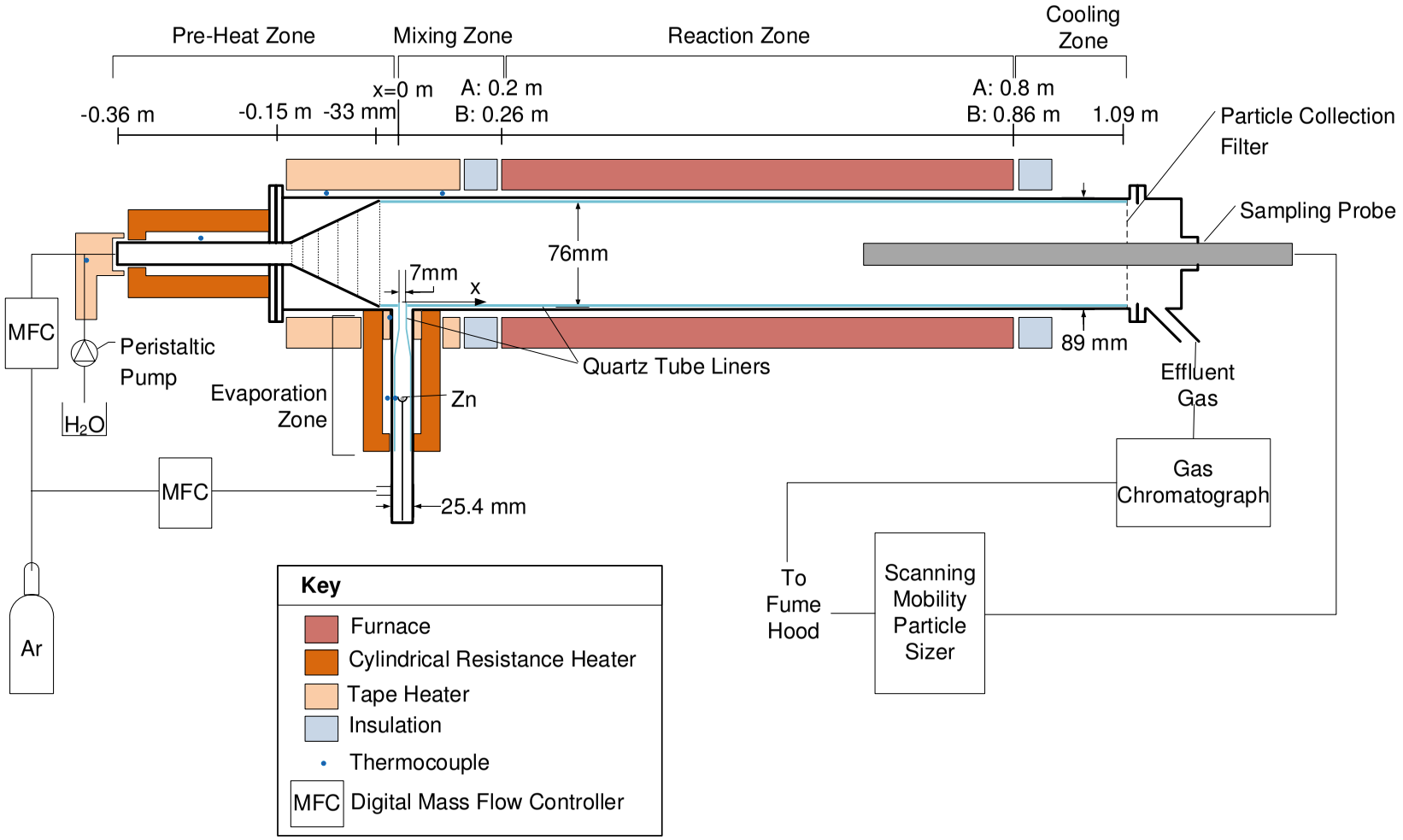

Figure 6.1: Schematic of the jet in cross-flow reactor (not to scale), including the pre-heat zone, mixing zone, Zn evaporation zone, reaction zone, and particle collection zone.

Table 6.1: Experimental parameters for experimental series 2: Hydrolysis and particle stability at varying reaction zone temperatures. $P_{Zn,eq}$ is the equilibrium partial pressure at T_{RZ}

	T_{RZ}	T_{EZ}	R	y_{H_2O}	$P_{Zn,eq}$ [atm]	$\frac{P_{Zn,eq}}{P_{Zn,total}}$	Ar quench flow rate $[L/min]$	Jet flow rate $[L/min]$	T_1	T_3	T_{filter}	configuration
A	$418\,K$	$1000\,K$	4.49	0	4.07×10^{-10}	0%	14.2	0.35	$423\,K$	$485\,K$	$333\,K$	A
B	$418\,K$	$1000\,K$	4.50	0.12	4.07×10^{-10}	0%	12.9	0.35	$423\,K$	$485\,K$	$335\,K$	A
C	$573\,K$	$1000\,K$	4.49	0	2.98×10^{-6}	3.3%	14.2	0.35	$423\,K$	$503\,K$	$435\,K$	B
D	$573\,K$	$1000\,K$	4.50	0.12	2.98×10^{-6}	3.3%	12.9	0.35	$423\,K$	$503\,K$	$449\,K$	B
E	$603\,K$	$1000\,K$	4.49	0	1.01×10^{-5}	11.1%	14.2	0.35	$423\,K$	$503\,K$	$453\,K$	B
F	$603\,K$	$1000\,K$	4.50	0.12	1.01×10^{-5}	11.1%	12.9	0.35	$423\,K$	$503\,K$	$454\,K$	B
G	$713\,K$	$1000\,K$	4.34	0	3.76×10^{-4}	100%	14.2	0.35	$453\,K$	$563\,K$	$423\,K$	A
H	$713\,K$	$1000\,K$	4.40	0.12	3.76×10^{-4}	100%	12.9	0.35	$443\,K$	$553\,K$	$430\,K$	A
I	$713\,K$	$1000\,K$	4.45	0.12	3.76×10^{-4}	100%	12.9	0.35	$433\,K$	$523\,K$	$452\,K$	B

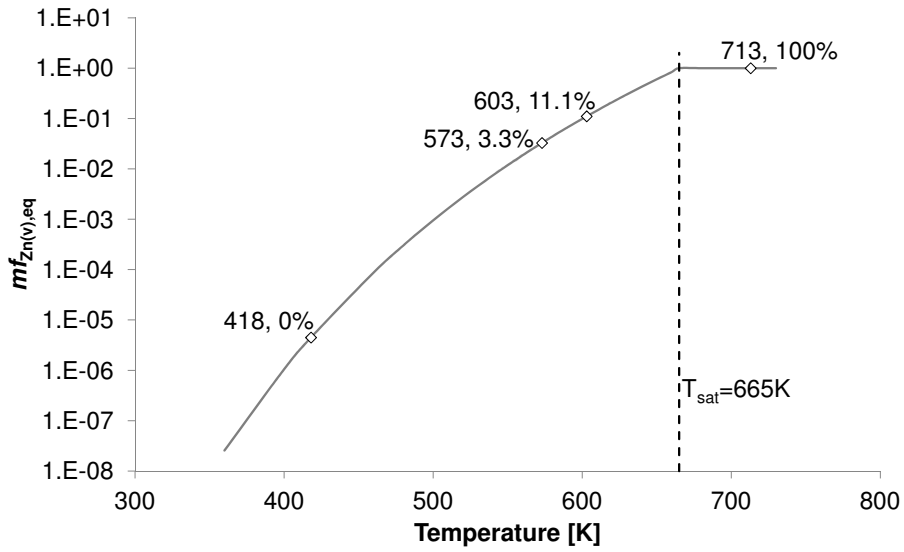

Figure 6.2: The fraction of mass that would be vapor at equilibrium, $mf_{Zn(v),eq}$ is plotted versus temperature over the range of temperatures relevant to this study. Experiments are conducted at $418\,K$, $573\,K$, $603\,K$, and $723\,K$, and are represented by the open diamonds plotted on the curve. The dashed line indicates $T_{sat} = 665\,K$.

$T_{RZ} \geq T_{sat}$, $mf_{Zn(v),eq} = 100\%$. Figure 6.2 shows $mf_{Zn(v),eq}$ as a function of temperature, with experimental reaction zone temperatures indicated by open diamonds and $T_{sat} = 665\,K$ indicated by a dashed line. In experiments at $T_{RZ} = 418\,K$, essentially none of the mass is vapor at equilibrium ($mf_{Zn(v),eq} = 4.5 \times 10^{-6}$); in experiments at $T_{RZ} = 573\,K$ (C and D), only a small fraction of the total Zn would be vapor at equilibrium (3.3%); in experiments at $T_{RZ} = 603$ (E and F), 11.1% of the Zn mass would be vapor at equilibrium; and in experiments at $T_{RZ} = 713\,K$ (G-I), which is above T_{sat}, all the Zn mass would be vapor at equilibrium.

Experiments have been conducted at temperatures above T_{sat} in prior studies as well, however in those studies particle formation was also suppressed. In contrast, in this study, particle formation occurs in the mixing zone of the reactor, where temperatures are much less than T_{sat}. The residence times for particles in the mixing zone are $\sim 2\,s$, longer than the total residence times in some past reactors [19, 20, 22–25]. So, regardless of T_{RZ}, an aerosol containing Zn particles in a mixture of Ar, H_2O, and (possibly) Zn gas enters the reaction zone. Temperatures upstream of the reaction zone are kept as constant as possible, though

conduction along the wall of the stainless steal reactor shell from the reaction zone results in variation in T_1 and T_3. Temperatures in the pre-heat and evaporation zones are constant across all experiments. The temperatures in the pre-heat zone are set to $T_{PH} = 398K$ ($125°C$). In the evaporation zone, $T_{EZ} = 1000\,K$ ($727°C$), and the tape heater at the tip of the evaporation zone is $885K$ ($612°C$). The temperature in the diffuser section of the pre-heat zone (T_1), the mixing zone wall (T_3), and just behind the filter vary by experiment, and are listed in Table 6.1. For all experiments $423\,K \leq T_1 \leq 458\,K$.

Experiments C-F and I are conducted in configuration B. The extended mixing zone provides more time for complete nucleation and/or condensation of the Zn vapor before particles enter the heated reaction zone. Comparison between experiments H and I thus provides insight into the degree of condensation that occurs in the mixing zone. The extra mixing zone length in configuration B also allows for more control over T_1, so that in experiments C-F, $T_1 = 423\,K$ despite the elevated reaction zone temperatures relative to experiments A and B. Overall hydrogen conversion (X), ZnO content on the filter (Z), yield on the filter (Y), deposition patterns, and morphology of particles collected on the filter from each experiment are used to gain insight into the hydrolysis process in the aerosol reactor and assess the effect of hydrolysis on particle morphology.

6.2 Results

6.2.1 Axial Temperature Profiles

The temperature profiles along the axis of the reactor for $T_{RZ} = 418\,K$, $573\,K$, $603\,K$, and $713\,K$ are plotted in Figure 6.3. The temperature along the axis of the evaporation zone (Figure 5.7) and quench rates are not greatly affected by the reaction zone temperature (see Section 5.3.2). Thus, quench rates are approximately $2 \times 10^4\,K/s$ in all experiments. The molar concentration of Zn decreases from 5.5×10^{-3} in the evaporation zone, to, on average 3.63×10^{-3} at the inlet to the mixing zone (after an average of 34% of the Zn condenses on the tip of the evaporation tube). The corresponding saturation temperatures are $827\,K$and $807\,K$, respectively. Assuming all Zn is in the vapor phase, y_{Zn} would be 8.5×10^{-5}, with

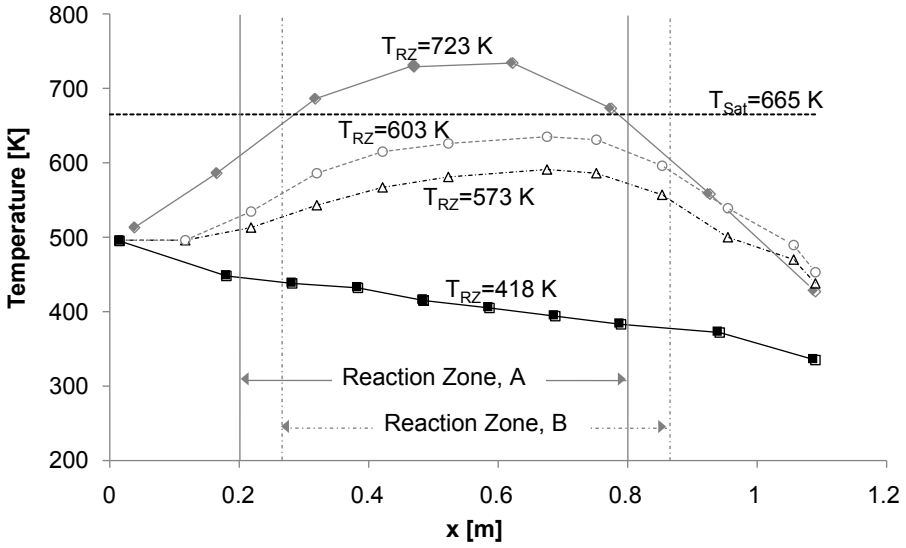

Figure 6.3: Axial temperature profiles for experiments with nominal reaction zone temperatures $418\,K$ ($145°C$), $573\,K$ ($300°C$), $623\,K$ ($350°C$), and $713\,K$ ($440°C$).

$T_{sat} = 665\,K$ in the reaction zone. This temperature is shown in Figure 6.3 (black dashed line).

6.2.2 Deposition Patterns

Properly interpreting key data such as overall hydrogen conversion (X), conversion of particles collected on the filter (Z), and particle yield on the filter (Y), relies on an understanding of where and how mass deposits in the reactor. Thus, this section includes a brief description of deposits in the evaporation zone, the reaction zone, the cooling zone, and on the filter. Three main types of deposits are observed: first, condensation of pure Zn, which is characterized by shiny silver droplets that are firmly attached to the wall; second, deposits of aerosol particles, which are gray in color and easy to wipe off; and ZnO by heterogeneous Zn vapor hydrolysis, which ranges from cloudy white to opaque off-white depending on concentration, and can only be removed by rinsing with diluted hydrochloric acid.

Condensation at the Tip of the Evaporation Zone

In all experiments, between 28% and 43% of the evaporated mass condenses on the upper $6\,mm$ of the quartz evaporation tube. On average, less mass condenses in the evaporation

Figure 6.4: ZnO deposition at the tip of the evaporation tube experiment H .

tube when the reactor is in configuration A than when it is in configuration B ($31.0\% \pm 1.5\%$ in configuration A vs $37.0\% \pm 3.8\%$ in configuration B). The presence of steam does not have any consistent effect on the fraction of mass that condenses. However, in experiments without steam, the deposits on the tip of the evaporation tube are shiny mirror-like silver droplets, characteristic of pure bulk Zn. In experiments with stream present, there is significant evidence of ZnO in the deposits on the tip of the evaporation tube (Figure 6.4). On the top edge of the tube, ZnO is deposited as off-white layers that are typical of pure ZnO by heterogeneous Zn vapor hydrolysis at high concentrations [19, 22, 25, 45]. In this region, Zn is entering the reactor in the vapor phase at high concentrations (relative to the rest of the reactor) and high temperatures and is mixing with H_2O at the edge of the jet. The surface of the top edge of the evaporation tube provides an ideal location on which the heterogeneous vapor reaction can occur. In addition, the cloudy translucent white deposits typical of pure ZnO formed by heterogeneous Zn vapor hydrolysis at lower concentrations occurs on the upper $2\,mm$ of the outside of the wall of the evaporation tube. In hydrolysis experiments, some of the measured overall conversion, X, is due to the reaction occurring at the jet exit.

Particle Deposits in the Mixing, Reaction, and Cooling Zones

In experiments A and B, deposition begins at approximately $x = 125\,mm$ on the upper part of the mixing zone wall. Particle deposits on the top part of the tube continue throughout the reactor, slowly tapering off in the stream-wise direction. In experiments C through I particle deposition on the upper part of the mixing zone wall is extremely light and hard to see; it tapers off by the beginning of the reaction zone. In these experiments, particle deposition is primarily observed in the cooling zone. Light particle deposits begin approximately $4\,mm$ after the start of the cooling zone (in both configurations) and gradually darken for the next $\sim 6\,mm$, after which deposits appear uniform until the filter.

The difference in deposition on the reactor walls in experiments A and B compared to experiments C-I is due to the different thermophoretic forces experienced by the particles. In experiments A and B, temperatures in the reaction zone are slightly cooler than those in the mixing zone, and wall temperatures are held as constant as possible along the heated length of the reactor (mixing and reaction zones). In contrast, the reaction zone is heated above the mixing zone temperatures in experiments C through I. The walls in these experiments are thus hotter than the entering gas, creating a temperature gradient in the reactor. Assuming a temperature gradient of $20\,K/mm$ near the wall, u_{th} is $0.18\,mm/s$ away from the wall for a $500\,nm$ particle. Thus, particles have a slight velocity away from the wall until near the start of the cooling zone. Given a temperature gradient of $30\,K/mm$ near the wall, $u_{th} = 0.36\,mm/s$ towards the wall. In this section, thermophoresis results in the observed increased deposits. Calculation of thermophoretic velocity, u_{th}, for particles in the reactor is described in Appendix H.

In the cooling zone, convective cooling cells are set up in the reactor that interact with the counter rotating vortex pair (CRVP) in the transverse jet. Figure 6.5 shows the filter deposits from experiment C. The CRVP appears in the bottom center part of the filter, while the other swirl pattern is due to the convective cooling cells as they rotate down the side of the reactor and then are directed up over the CRVP. Prior to cooling, the CRVP would have been significantly higher in the reactor and would have had a larger diameter.

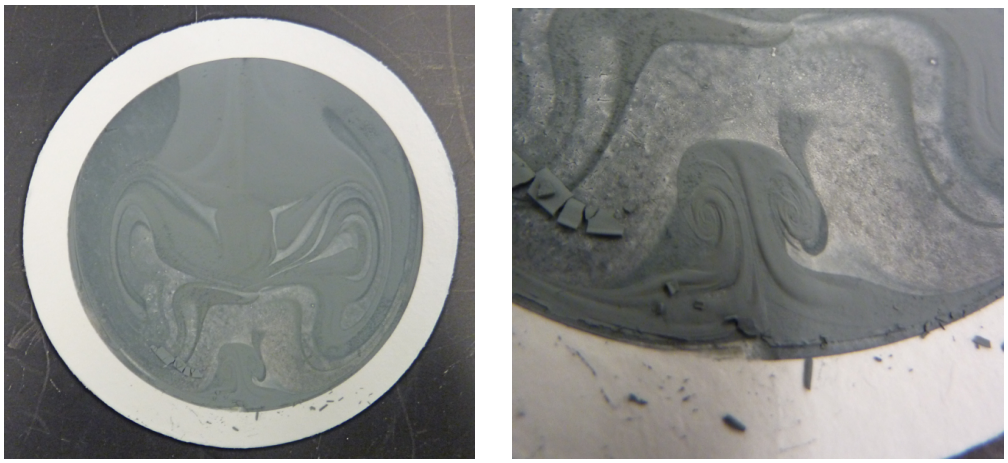

(a) (b)

Figure 6.5: Filter deposits from experiment C showing (a) the entire filter and (b) a close-up on the CRVP.

ZnO by Heterogeneous Zn Vapor Hydrolysis

Though there is no particle deposition on the walls of the reaction zone for $T_{RZ} \geq 573\,K$, in most experiments with steam there are cloudy white deposits characteristic of pure ZnO by heterogeneous Zn vapor hydrolysis [19, 21, 45]. This observation is important—it indicates that Zn vapor was present in the reaction zone and reacting with steam on available surfaces. Observations of the opacity of the ZnO deposits are qualitative indicators the importance oft the vapor reaction in overall Zn hydrolysis, with more opaque white deposits corresponding to high levels of ZnO deposition. There is no evidence of this type of deposit in experiment B ($T_{RZ} = 418\,K$). However, in experiment D ($T_{RZ} = 573\,K$), the ZnO was extremely light, but visible. In experiments F, H, and I, the ZnO deposits became more opaque with increasing temperature.

Experiments H and I offer an interesting comparison. These experiments were nominally identical except for configuration—experiment H had a shorter mixing zone than experiment I. In both cases, the ZnO deposits began at the beginning of the reaction zone. In experiment H, deposits continued until the end of the reaction zone, while in experiment I, deposits slowly tapered off, ending $0.2\,m$ before the end of the reaction zone. The fact that ZnO deposition ceased before the end of the reaction zone in the experiment with the longer mixing

zone is evidence that there was less Zn vapor entering the reaction zone in that experiment; chemical vapor deposition of ZnO slowed and then stopped because the availability of the reactant, Zn, decreased. The difference in available Zn vapor is a result of the different mixing zone lengths. In the mixing zone, particles grow by condensation, so in a longer mixing zone, there is more time for growth, and more Zn condenses onto particles. This is evidence that Zn is not re-evaporating from the particles in hydrolysis experiments, but simply still in the vapor phase at the end of the mixing zone.

6.2.3 Conversions and Yield

The extent of the reaction is quantified in two ways: first, overall conversion, X, is the total molar H_2 production as a fraction of the theoretical maximum H_2 production. In prior work, this measure included, and was dominated by, hydrolysis of particles deposited on the reactor walls. In that case, X strongly depended on the experimental duration, as particles deposited on the walls of the reactor continued to react as long as temperatures were elevated and H_2O was present. In this work, particle deposition on the walls of the reaction zone has been eliminated for $T_{RZ} \geq 573\,K$. However, X does include H_2 produced by heterogeneous Zn vapor hydrolysis at the jet inlet and on the walls of the reaction zone. These reactions stop as soon as Zn evaporation is completed, so X is not a function of experimental duration in the present study. However, the goal of aerosol reactors is conversion of aerosol particles, so the conversion in the aerosol, Z, is a far more instructive parameter. To obtain accurate measurements of Z, the internal standard method [64] is used to create an XRD calibration, as described in Section 4.2, for measuring the ZnO content (by mole) of particles collected on the filter. The particle yield, Y, is the fraction of the mass entering the reactor that is collected on the downstream filter and cooling zone walls (Equation 4.6). Because a major appeal of the aerosol process is that it can be continuous, particle yield, Y, and conversion in the aerosol, Z, define the success of experimental reactors.

Both X and Z are listed for each experiment in Table 6.2. As expected, in experiments without steam both overall conversion and conversion of filter particles is zero. The extent of conversion predicted by Ernst et al.'s kinetic expression for the surface reaction [13] on

Table 6.2: Experimental series 2: Hydrolysis and particle stability at varying reaction zone temperatures.

	T_{RZ}	T_{EZ}	y_{H_2O}	config.	τ_{ave}	X	Z	Predicted Conversion [13]	Y
A	$418\,K$	$1000\,K$	0	A	$11.7\,s$	0%	–		84.2
B	$418\,K$	$1000\,K$	0.11	A	$11.7\,s$	$11\% \pm 3\%$	–		93.1
C	$573\,K$	$1000\,K$	0	B	$5.8\,s$	0%	0%		74.5
D	$573\,K$	$1000\,K$	0.12	B	$5.8\,s$	$17\% \pm 6\%$	$1.5\% \pm 0.6\%$	0%	81.6
E	$603\,K$	$1000\,K$	0	B	$5.5\,s$	0%	0%		74.6
F	$603\,K$	$1000\,K$	0.12	B	$5.5\,s$	$24\% \pm 3\%$	$2.2\% \pm 0.6\%$	0.4%	77.5
G	$723\,K$	$1000\,K$	0	A	$4.8\,s$	0%	0%		84.7
H	$723\,K$	$1000\,K$	0.12	A	$4.8\,s$	$49\% \pm 8\%$	$6.3\% \pm 0.6\%$	1.5%	59.4
I	$723\,K$	$1000\,K$	0.12	B	$4.8\,s$	$36\% \pm 4\%$	$6.8\% \pm 0.6\%$	1.5%	72.4

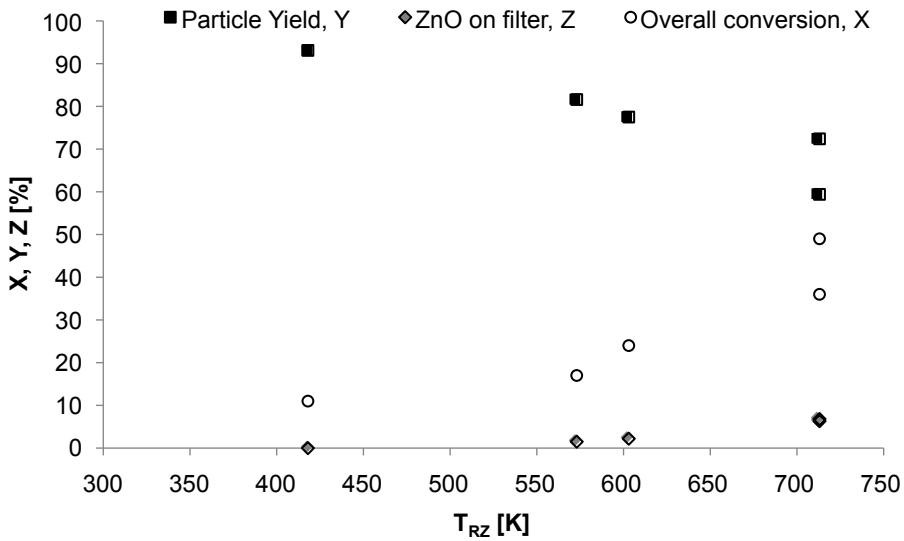

Figure 6.6: Overall molar conversion, X (circles), ZnO content by mole on the filter, Z (diamonds), and filter yield, Y (squares), plotted against T_{RZ}.

a $500\,nm$ diameter particle at the residence times and temperatures appropriate for each experiment is also listed in Table 6.2. The method used to extend the kinetic expression for use here is described in Appendix A. The kinetic expression for the surface reaction is used to provide the most optimistic prediction of aerosol conversion possible from the TGA kinetic expressions. Figure 6.6 shows overall molar conversion, X (circles), ZnO content by mole on the filter, Z (diamonds), and particle yield, Y (squares), plotted against T_{RZ}.

In general, both X and Z increase with temperature, consistent with past aerosol hydrolysis reactors [19–25] and kinetic studies [12, 13, 24]. While kinetics improve with increasing temperature, $P_{Zn,eq}$ increases as well, and with it $mf_{Zn(v),eq}$. In fact, the increase in X with temperature is consistent with the visual observations of ZnO deposits by heterogeneous Zn vapor hydrolysis on the wall of the reaction zone.

The measured ZnO content on the filter, Z, is about five times greater than the predicted extent of conversion for particle hydrolysis, even given the use of the surface reaction kinetics. The difference between the predicted conversion and Z could be attributed to the fact that, at least in oxidation of other metals, kinetics are faster in the aerosol than is measured via TGA. However, as discussed in Section 2.2.2, the thermodynamic favorability of the heterogeneous Zn vapor hydrolysis implies that if they are both present Zn vapor will react

heterogeneously with H_2O on any available surface. In all cases ZnO by heterogeneous Zn vapor hydrolysis was observed on the walls of the reaction zone (see Section 6.2.2), confirming that some Zn was in the vapor phase in the reactor and that it was reacting with H_2O on solid surfaces. Once an initial layer of ZnO forms on the particle surface, either by direct hydrolysis of the particle or by heterogeneous Zn vapor hydrolysis, there will be fewer kinetic limitations to a H_2O molecule reacting with a Zn vapor molecule heterogeneously on the surface of the particle, than the diffusion limited reaction that would be required for further hydrolysis of the Zn particle [13, 18].

In experiment B, the overall measured conversion, X, is 11%. At this temperature, the expected conversion was to $Zn(OH)_2$, not ZnO. According to the reported kinetics (for $70\,nm$ particles), conversion to ZnO after the $12\,s$ residence time in the reactor at $T_{RZ} = 418\,K$ would be 1.7 to 3.4% for $1\,\mu m$ to $500\,nm$ particles, respectively [17]. Use of this kinetic expression for larger particles is likely to result in over-predictions of conversion, given the dependency of kinetics on particle size [14, 26]. No peaks associated with $Zn(OH)_2$ were observed in the XRD spectra, though an extremely small ZnO peak was observed. This peak could be evidence that some $Zn(OH)_2$ formed and then subsequently dissociated to ZnO and H_2O, a process that occurs starting at temperatures above $423 - 448\,K$. However the temperature profile in the reactor, in which temperatures slowly drop from $440\,K$ to $373\,K$, indicates that the dissociation of $Zn(OH)_2$ is unlikely. The ZnO peak observed via XRD is too small to be quantified with the XRD calibration, which only goes down to 0.5% (see Section 4.2.1). However, the presence of a small Zn peak in this experiment, when no such peaks were measured in experiments without steam, is of note. The small ZnO peak may be evidence that a thin ZnO layer forms on the surface of particles in the mixing zone, consistent with SEM images of particle morphology in experiments G and H. This initial ZnO layer could be formed either by direct hydrolysis of the particle or via heterogeneous Zn vapor hydrolysis. Because the ZnO peak is so small, the 11% overall conversion is attributed to the heterogeneous Zn vapor hydrolysis reaction that deposited ZnO around the jet inlet. Conditions around the jet inlet are very similar across experiments, so it is likely that approximately 10% of the total Zn mass reacts at the jet inlet in the other

hydrolysis experiments as well (experiments D, F, and H-I).

The only significant operating condition difference between experiments H and I was their configuration, with experiment I set up in configuration B (longer mixing zone). The overall conversion in experiment I is 36%—over 10% less than the 49% conversion measured in experiment H. The lower conversion in experiment I is consistent with visual observations of ZnO on the reactor walls. In the mixing zone, particles are growing by condensation, so in the longer mixing zone of experiment I, there is more time for growth, and more Zn condenses onto particles, resulting in less Zn vapor in the reaction zone. The reduction in overall conversion is a direct result of the reduced Zn vapor available for heterogeneous Zn vapor hydrolysis. However, the ZnO content of the filter particles is basically the same (within the uncertainty range of each other).

Figure 6.6 shows the particle yield, Y, decreasing with increasing T_{RZ}. In fact, the decrease in Y with increasing T_{RZ} is mirrored by the increase in X with T_{RZ}. At higher reaction zone temperatures, more Zn mass reacts heterogeneously with steam on the reaction zone wall, resulting in both increase hydrogen production and decreased particle yields on the filter. At all temperatures, Y is significantly higher than has been achieved to date. In configuration B, the yield is over 70% for all experiments. In experiments without steam, Y shows no temperature dependency and is between 75% and 85% in all four experiments (see Table 6.2).

6.2.4 Particle Morphology

Figure 6.7 shows SEM images of the particles collected on the filter in experiments with and without steam at $T_{RZ} = 418\,K$ (experiments A and B), $T_{RZ} = 573\,K$ (experiments C and D), and $T_{RZ} = 713\,K$ (experiments G and H). The reaction zone temperature in experiments A-D were all low enough that $mf_{Zn(v),eq}$ is negligible (A and B) to small (C and D). In all four experiments, the particles are primarily hexagonal in shape. They grew via a 2-D growth mode from the vapor, layer by layer [66]. Similar hexagonal particles have been formed in other Zn aerosol reactors [5, 21, 22] and were predicted in the Zn nucleation and growth model by Ernst [41].

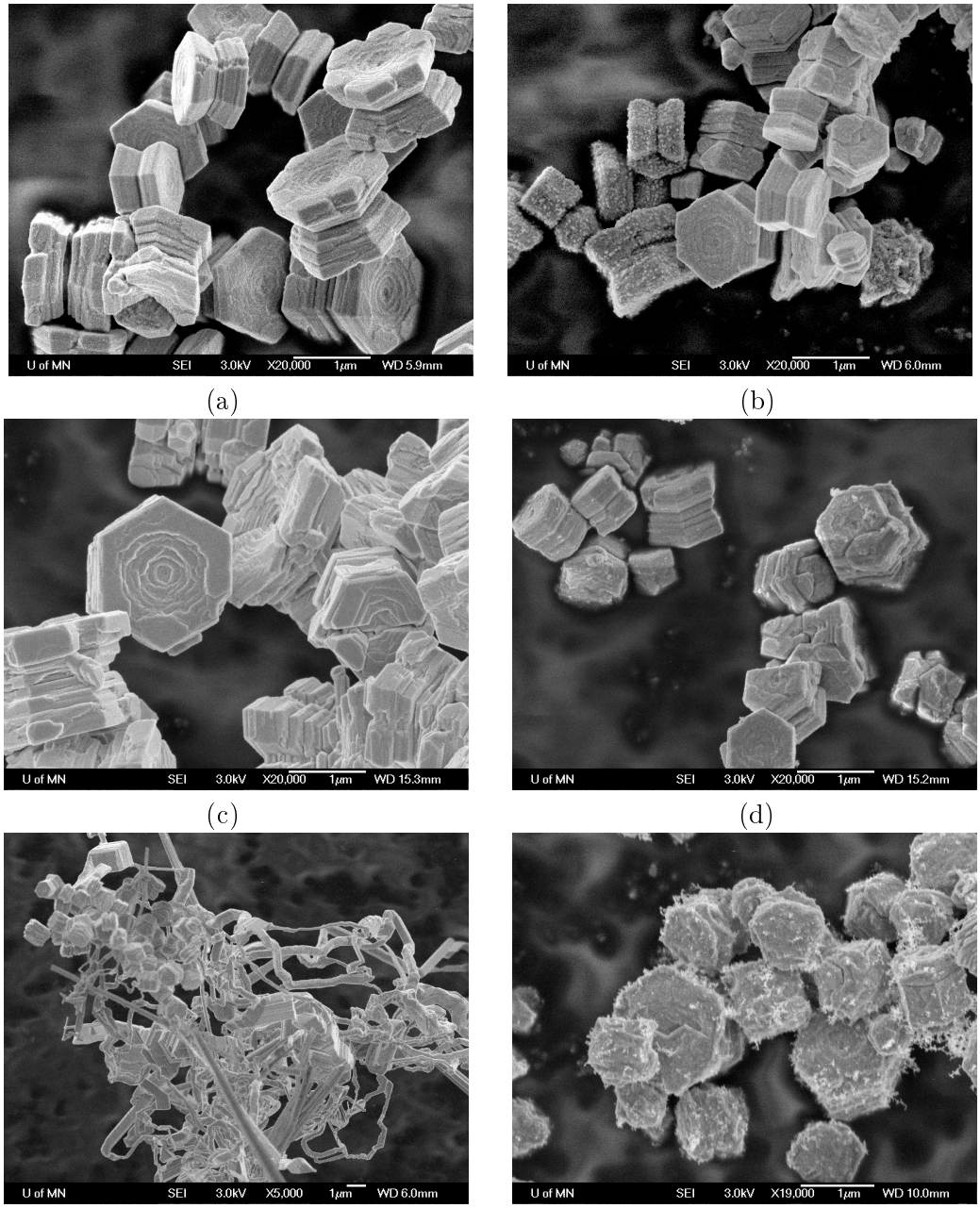

(a) (b) (c) (d) (e) (f)

Figure 6.7: SEM images of particles collected on the filter of experiments A-D, G and H. (a) Experiment A, with $T_{RZ} = 418\,K$ and $y_{H_2O} = 0$; (b) Experiment B, with $T_{RZ} = 418\,K$ and $y_{H_2O} = 0.11$; (c) Experiment C, with $T_{RZ} = 573\,K$ and $y_{H_2O} = 0$; (d) Experiment D, with $T_{RZ} = 573\,K$ and $y_{H_2O} = 0.12$; (e) Experiment G, with $T_{RZ} = 723\,K$ and $y_{H_2O} = 0$; (f) Experiment H, with $T_{RZ} = 723\,K$ and $y_{H_2O} = 0.12$.

In both sets of experiments, particles grown in hydrolysis experiments (with steam) (Figure 6.7b and d) are generally $300\,nm$ to $1\,\mu m$ across the hexagonal face, while particles grown in the aerosol reactor without steam (Figure 6.7a and c) are generally $1-3\,\mu m$. Particles in experiments A and C especially, and B to a lesser extent have holes in the top and bottom hexagonal faces. In addition, particles in experiments A-D are narrower in the center than on the top and bottom, much like an hour glass. This shape has been attributed to partial evaporation of hexagonal Zn particles [26]. Experiments below T_{sat} without steam (A and C) have more material etched away from the center, showing more evidence of evaporation than the comparable experiments with steam (B and D). In addition, hydrolysis experiments show less evidence of evaporation with increasing T_{RZ}, which is attributed to the faster reaction rates and greater extent of conversion of aerosol particles at higher temperatures.

In both experiments without steam, the faces are relatively smooth, especially compared to the experiments with steam, which have much smaller scale growths on some, though not all, of the particles. This "roughness" on the surface of particles has been attributed to partial oxidation [5]. These smaller growths have characteristic lengths of less than $100\,nm$, and occasionally there are agglomerates made entirely of these small scale structures (see Appendix I for more SEM images of filter particles). The agglomerates with small characteristic length scales are likely to have formed from particles that nucleated at lower concentrations than those present very near the jet inlet. Their small characteristic lengths also indicate short residence times, so they may have formed in the cooling zone.

Unlike particles from experiments A-D, in which the presence of steam had subtle effects on particle morphology, the morphology of particles collected on the filters in experiments G (without steam) and H (with steam) are drastically different. Figure 6.7(d) shows the filter deposits from experiment G, in which the reaction zone was at a temperature high enough that, if the system was at equilibrium, all the Zn would be in the vapor phase and in which no was steam present. There are some hexagonal particles approximately $1\,\mu m$, but the majority of the deposits are Zn nanowires, often called filamentary particles in the prior literature on Zn aerosol hydrolysis reactors [5, 21, 22, 25]. In addition to the wires

and hexagonal particles, there are 2 to 10 μm sharp edged layered structures, long "needles", and spherical or nearly spherical particles made out of layered hexagons, generally around 5 μm in diameter (see Appendix I).

The wires provide the most insight into the formation of these deposits. A few studies in the literature document the deliberate formation of Zn nanowires [67, 68]. In both cases, Zn vapor is produced in a tubular furnace and collected downstream on a filter or substrate, from which the nanowires are collected. Both groups state that the Zn nanowires are formed *on the collection surface*, not in the gas stream. The deliberately produced nanowires have very similar morphologies to those produced in experiment H. Furthermore, given that the temperature in the reactor was above the saturation temperature for the Zn concentration present, we might expect a significant fraction of the Zn to be gaseous. These facts are strong evidence that without the layer of ZnO to impede re-evaporation, much of the Zn mass that nucleated into particles in the mixing zone of the reactor re-evaporated in the reaction zone, and that the nanowire structures formed on the filter surface from that Zn vapor. The hexagonal and spherical particles are likely to have remained particles through the reaction zone, given their structural similarity to particles from lower temperature experiments.

Figure 6.7(e) shows the particles collected on the filter from the hydrolysis experiment H at the same temperature ($T_{RZ} = 723\,K$). The difference in morphology is stark. In the hydrolysis experiment, the particles are hexagonal and generally 1 μm or less, much like the particles in hydrolysis experiments at lower temperatures, though at this temperature the hour glass shape and hole in the hexagonal faces is not present. The small agglomerate structures with characteristic lengths significantly less than 100 nm are also again present, and are more common at this temperature than at the lower temperatures. The difference in the morphology of the particles in the hydrolysis experiment is attributed to the early formation of a ZnO layer on the surface of the particles that impedes their re-evaporation in the reaction zone.

Approximate aerosol concentrations can be made based on the particle sizes observed in the SEM images and the Zn mass concentration in the reactor. Given the evaporation rate of $5.3 \times 10^{-3}\,g/min$ and the total flow rates of steam and argon in the reactor, the Zn mass

concentration is $1.7 \times 10^{-7}\, g/cm^3$. A mono-disperse aerosol of $300\, nm$ particles would have a concentration of $\sim 10^6/cm^3$, while a mono-disperse aerosol of $1\, \mu m$ particles would have a concentration of $4 \times 10^4/cm^3$.

6.2.5 Aerosol Sampling

For the most part, the particles in the aerosol of this study were too large to measure with the SMPS, which measured up to $230\, nm$ particles (equivalent mobility diameter). However, measurements that were taken during experiments with $T_{RZ} = 418\, K$ and $713\, K$ without steam support the conclusion that the majority of Zn was in the vapor phase in the reaction zone at $T_{RZ} = 713$ and was particles at $T_{RZ} = 418\, K$, shown in Figure 6.8. In the reaction zone ($x = 0.48\, m$) at in the experiment at $T_{RZ} = 418\, K$, the SMPS measured large particles ($d_p > 50\, nm$) and a total concentration of $\sim 10^4/cm^3$ (Figure 6.8a). The aerosol distribution shows a peak concentration at $d_p = 178\, nm$. However, given SEM images from comparable experiments, it is likely that the SMPS measured the lower part of the aerosol distribution. The decreased measurements for $d_p > 178\, nm$ are attributed to lower sampling efficiencies for larger particles in the sampling probe. In contrast, SMPS measurements taken during the same experiment but near jet inlet in the mixing zone ($x = 25\, mm$), where Zn vapor concentrations are expected to be high, reveal primarily very small particles ($< 20\, nm$), as can be seen in Figure 6.8b. These small particles can be understood as the result of sampling Zn vapor that is quenched by dilution gas in the sampling probe. Further cooling occurs in the hose connecting the probe to the SMPS. Much like the samples taken from the near the jet inlet in the low temperature experiment, particles sampled from the reaction zone ($x = 540\, mm$) in the experiment at $T_{RZ} = 713\, K$, were very small particles ($< 30\, nm$), a further indication that the particles re-evaporate when $T_{RZ} > T_{sat}$ (Figure 6.8c).

6.3 Conclusion

Hydrolysis experiments conducted in the transverse jet reactor with $R = 4.5$ at $418\, K$, $573\, K$, $603\, K$, and $713\, K$ are used to assess the mechanisms of particle growth and hydrolysis in

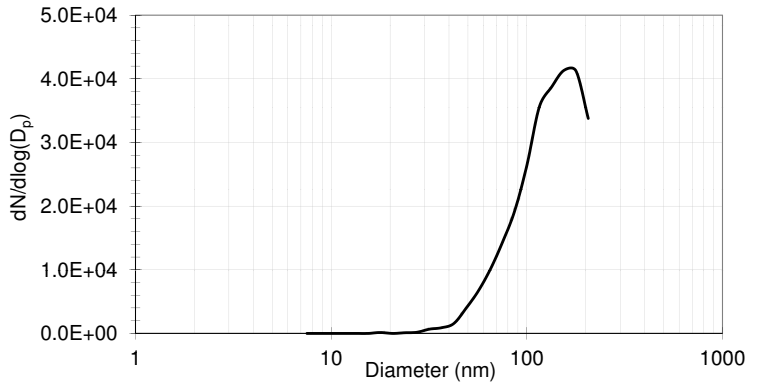

(a)

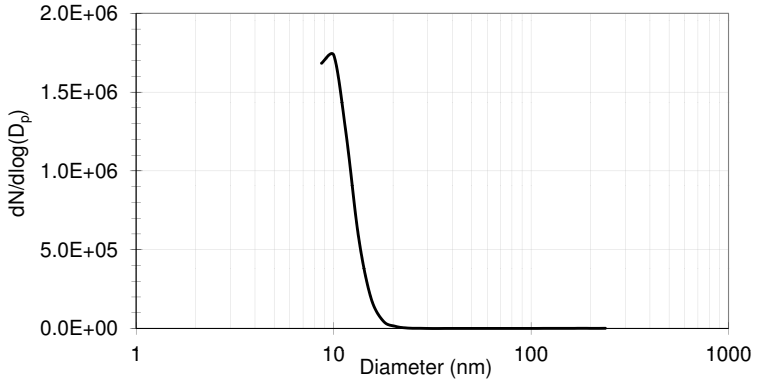

(b)

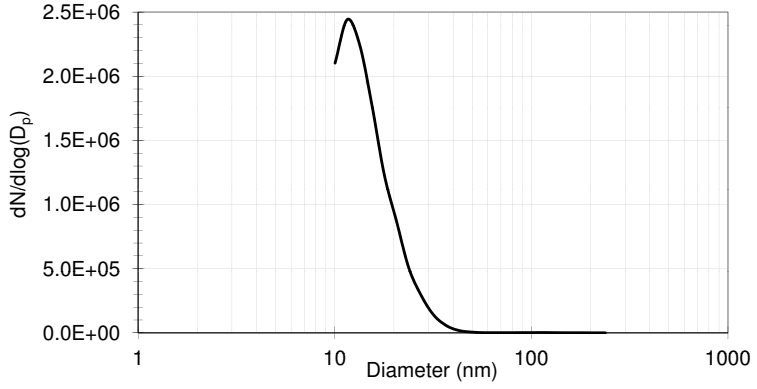

(c)

Figure 6.8: SMPS particle measurements for (a) $T_{RZ} = 418\,K$ at $x = 25mm$, (b) $T_{RZ} = 418\,K$ at $x = 480mm$, and (c) $T_{RZ} = 713\,K$ at $x = 540mm$.

the aerosol. Residence times in the reactor are $\sim 12\,s$ at $418\,K$ and $\sim 5\,s$ for experiments at $573\,K$ and above. Experiments are conducted with and without steam to assess the effect of the reacting gas on particle morphology. SEM images of particles collected on a filter downstream from the reaction zone indicate that particle growth is dominated by condensation, resulting in hexagonal particles generally with lengths across their hexagonal face of $300\,nm$ to $1\,\mu m$ in experiments with stream, and 1 to $3\,\mu m$ in experiments without steam. SEM images indicate that in hydrolysis experiments, a ZnO shell forms on the surface of particles early on, protecting them from re-evaporation. Hydrolysis experiments at higher temperatures show less evidence of evaporation, than at lower temperatures, which is attributed to the faster kinetics at higher temperatures. Filter deposits from an experiment above T_{sat} without steam are primarily Zn nanowires, which form on the filter from Zn vapor [67, 68].

The conversion in the aerosol is $< 7\%$ and decreases with reaction zone temperature. The overall conversion ranges from 11% at $418\,K$ to 49% at $713\,K$. The difference between overall conversion and conversion in the aerosol is attributed to heterogeneous Zn vapor hydrolysis on the walls of the reaction zone and near the jet inlet, as evidenced by characteristic deposits. Given that Zn vapor is present in the reactor and reacting with steam on the wall, it is inferred that the heterogeneous Zn vapor reaction also occurs on the surface of aerosol particles. In that case, some of the measured ZnO content of filter particles is due to heterogeneous vapor hydrolysis, not conversion of the aerosol particle.

This study finds no evidence of the low temperature, $Zn(OH)_2$ process, which was previously observed for $70\,nm$ diameter particles [17]. At the reported reaction rates for $Zn(OH)_2$ formation, a $70\,nm$ particle would have a conversion of 16% for the residence time ($8\,s$) and temperature ($418\,K$) in the transverse jet reactor, whereas no conversion was measured for micron sized particles in this reactor. Thus, the lack of evidence of $Zn(OH)_2$ may be attributable to insufficient residence times for $300\,nm$ to $1\,\mu m$ particles to measurably react.

Particle yield decreases with increasing reaction zone temperature due to the greater amounts of ZnO deposited on the reaction zone walls. However at all temperatures, high

particle yields are attained—60 to 93% in all experiments, and 72 to 82% in hydrolysis experiments conducted in configuration B. Further, particle deposition on the walls of the reaction zone is eliminated for temperatures of $573\,K$ and above. Thus, careful attention to the fluid dynamics generally, and a transverse jet reactor specifically, can be used to significantly reduce particle deposition on the walls, an important step towards the success of the continuous aerosol process.

Chapter 7

Renewable Hydrogen from the Zn/ZnO Thermochemical Cycle: A Cost and Policy Analysis

7.1 Introduction

Most scientists agree that in order to avoid some of the most serious consequences of climate change, atmospheric greenhouse gas (GHG) concentrations should be stabilized at or below an equivalent doubling over pre-industrial levels—approximately 500 ± 50 parts per million [69, 70]. This tremendous challenge will require bold policy action and continuing innovation in the field of renewable energy technologies. Pacala and Socolow [69] suggest that the goal can be met by stabilizing emissions at 2004 levels through 2054, followed by a linear decline to about two thirds of 2004 levels by 2104. They argue that stabilization over the next 50 years can be achieved through the use of current technologies. However, to achieve the reductions necessary in the second half of the century, new and transformational renewable energy technologies will be necessary. Policies and technological development must strive both to meet near-term GHG reduction goals and to plan and prepare for meeting long term goals. If the scientific and engineering community can overcome the considerable technical challenges of the cycle, hydrogen production via the Zn/ZnO cycle could the type

of transformational technology they call for.

This analysis explores the economic viability of the Zn/ZnO hydrogen production cycle and the policy tools necessary to make it economically competitive with steam methane reforming. Technological improvements will be necessary for the Zn/ZnO cycle to achieve an efficiency that approaches the theoretical maximum value. However, if these technical issues are resolved, the important question will be whether H_2 produced by this process is economically competitive. If not initially, what kinds of policies would be needed to make this process economically viable in the long term?

Most climate change mitigation policies fit into two categories. The first type of policy involves internalizing the cost of carbon emissions through a carbon tax or a cap and trade program. By placing a price on carbon emissions, this type of policy makes all renewable and energy efficient technologies more cost competitive. The appropriate level of carbon taxation is the social cost of carbon emissions, or the marginal externalized cost to society of emitting one extra tonne of CO_2. Estimates of the social cost of carbon vary widely by study, but in their 2007 report, the IPCC summarized the literature and found an average social cost of \$158 per metric tonne of CO_2 (tCO_2) with a standard deviation of $\$304/tCO_2$ [70]. European countries with carbon tax programs have instituted taxes well below this range (i.e., $\$24.39/tCO_2$ in Finland for heating and transportation fuels, but not electricity generation [71]).Carbon tax or cap and trade policies are generally considered the most economically efficient way to increase the market share of renewable energy. Under these policies, the market operates to identify and implement the least expensive CO_2 reduction methods first, only implementing more expensive technologies after the less expensive options have been exhausted. The danger in relying solely on these market based CO_2 reduction strategies is that insufficient resources may be put into development of future technologies—technologies like the Zn/ZnO cycle—that have potential to be important energy sources in the future.

The second type of climate change mitigation policy aims to increase the implementation of renewable energy and energy efficient technologies and practices by making them more economically competitive and/or by decreasing investment risk. Such incentive poli-

cies include direct financial support for research and development (R&D), demonstration, and initial commercial projects; and indirect support through tax incentives, purchase guarantees, or low interest rate loans. History has shown that incentive policies are critical in the early stages of market penetration, as they enable investment in risky or unproven technologies with high capital costs and uncertain revenue streams (such as the Zn/ZnO cycle) [72]. Ideally, technologies eventually become cost competitive without incentives. However, in some past cases in which incentive policies were used to support a technology, the expectation that increased experience leads to reduced costs did not hold [72]. If implementation proceeds too rapidly for successive plants to learn from the experience of those that came before, prices can increase as cumulative installed capacity grows, as initially occurred in the U.S. nuclear power industry. Also, a market structure with price guarantees and limited competition can result in little reduction in cost as experience increases, as happened in the Japanese liquid natural gas industry. Thus, though incentivizing specific technologies may not be the most economically efficient path to reduce GHG emissions, some important technologies require direct and indirect government support, especially in R&D, demonstration, and early commercialization. To keep the technology on a path in which increased experience leads to decreased costs, policies should be clearly defined and consistent, diffusion of the technology should not be excessively rushed, and a way to transition to a competitive market structure should be planned into the policy.

In this chapter, the predicted cost of hydrogen produced using the Zn/ZnO cycle is compared to the costs of hydrogen production via steam methane reforming (SMR). Methane reforming accounts for about 95% of hydrogen production in the United States [73], and is therefore likely to be the most significant non-renewable competition for the Zn/ZnO solar thermochemical cycle. The level of carbon taxation that would be necessary to make H_2 produced by SMR cost as much as H_2 produced by the Zn/ZnO cycle is calculated, and is found to be higher than is politically feasible. Consequently, this study focuses on the efficacy of incentive policies to help bring the technology down its learning curve until it is economically competitive. The effect of accumulating experience (i.e., cumulative production) on the cost of H_2 produced by the Zn/ZnO cycle is predicted based on a

range of estimated progress ratios for the Zn/ZnO cycle. To tie the cost to time, three policy scenarios are applied to estimate the time frame for the accumulated experience. The projected costs are compared to the cost of H_2 produced via SMR, which is predicted based on increasing costs of methane and decreasing operation and maintenance (O&M) costs due to the learning effect of accumulated experience. Policies that would make solar hydrogen cost competitive with SMR are discussed.

It should be noted that there are strong and logical arguments against policies that favor particular technologies—the market should decide which technologies succeed, not policy makers [74]. Picking technology winners may result in a less than optimal use of funds, especially if the technology is picked for political reasons, rather than for scientific or environmental reasons. This paper is not intended to advocate for "picking" the Zn/ZnO cycle, rather it is an exploration of the policy and economic factors that would be required for the technology to compete with SMR. The present analysis does not consider other renewable hydrogen production paths, which will also compete with SMR. The analysis does not consider issues of storage, transportation, distribution of hydrogen, or the status of fuel cell technology. How these issues play out will have significant impacts on the relative importance of hydrogen in the overall energy portfolio, but they will have a lesser effect on how hydrogen is produced.

7.2 Analysis

The goals of this analysis are to evaluate the effects of both a carbon tax policy and incentive policies on the relative costs of the Zn/ZnO cycle and steam methane reforming, to estimate the level of public and private investment needed to bring the Zn/ZnO cycle down its experience curve to economic competitiveness, and to estimate the break even point for the Zn/ZnO cycle—the year when it becomes economically competitive with SMR. To achieve these goals, we first compare predicted costs of the Zn/ZnO cycle [1, 75] with near term SMR costs [73, 76, 77] and calculate the level of carbon taxation necessary to make hydrogen

produced by SMR the same price as hydrogen produced via the Zn/ZnO cycle.

Second, we use experience curve analysis to estimate the level of public and private investment needed to bring the Zn/ZnO cycle down its experience curve. The initial price and production level used in the experience curve are taken to be $\$14.75/kg$ and $100000\,kg/yr$, consistent with the estimate for the smallest plant analyzed in the literature [1, 75]. The small plant was chosen as the initial plant because the investment risk on a small plant is less than on larger plants. The progress ratio for the Zn/ZnO cycle is calculated from assumed and estimated values of the progress ratios of the constituent parts of the cycle—the concentrating heliostat field and solar receiver and the two step chemical reactors—and estimated to be 0.82 ± 0.05. The level of public and private investment needed to bring the Zn/ZnO cycle to economic competitiveness is the integrated difference in the prices of H_2 produced by the Zn/ZnO cycle and by SMR.

To predict the break even year for the Zn/ZnO cycle, the cost of hydrogen produced by the Zn/ZnO cycle and SMR are estimated as a function of time. The experience curve for the Zn/ZnO cycle, which expresses cost as a function of cumulative experience, is tied to three possible policy scenarios defined by three rates of implementation of the Zn/ZnO cycle. Similarly, the cost of hydrogen produced by SMR is predicted based on the experience curve effect for that technology combined with predicted increasing cost of methane. The initial cost of hydrogen produced by SMR is assumed to be $\$3/kg$ and the fraction of the cost due to the price of natural gas is taken to be 0.6. A sensitivity analysis of the effect of changing the value of these parameters is conducted over the range of reasonable assumptions for each. The break even year was found to be relatively consistent over the range of reasonable assumptions; generally varying by a decade or less.

7.2.1 Calculating the required level of carbon taxation

To estimate the level of carbon taxation necessary for the Zn/ZnO cycle to compete economically with SMR, predicted cost estimates for hydrogen produced via the Zn/ZnO cycle are taken from the literature [1, 75], while near term estimates of the cost of hydrogen pro-

duced by SMR are calculated based on a range of probable natural gas prices in the near term.

The cost of hydrogen production via the Zn/ZnO cycle has been previously analyzed by Steinfeld [1] and Charvin et al. [75]. Both studies account for the optical efficiencies in the solar concentrating field and efficiencies defined by the thermodynamic irreversibility of the chemical reactions. They include thecost of the solar power plant, the reactor, and annual operation and maintenance and financing costs, and assume that all costs associated with GHG emissions are external. They both assume the concentrated solar energy is provided by a solar power tower. Because the present analysis is based on these two prior studies, a solar power tower is assumed in this analysis as well. The two prior studies are summarized in Table 7.1.

Steinfeld [1] predicts that H_2 produced via the Zn/ZnO cycle would cost $\$5.02/kg$ based on a plant producing $792\,kg/hr$. He neglects external work input, and assumes no heat recovery and no recombination in the solar step, and complete hydrolysis and recovery of Zn in the second step. The total capital cost is estimated to be \$55.08 million, and total O&M costs are estimated to be \$9.36 million. With these assumptions, the thermodynamic analysis indicates a theoretical efficiency[1] of 29%.

Charvin et al. [75] predict that H_2 produced via the Zn/ZnO cycle would cost $\$7.98/kg$ based on a plant producing $250\,kg/hr$, and $\$14.75/kg$ based on a plant producing $50\,kg/hr$. They attribute their higher estimations to the smaller scale of the plants assumed. As in Steinfeld's analysis, external work input is neglected and the hydrolysis step is assumed to be complete. In contrast to Steinfeld's analysis, Charvin et al.'s study includes heat recovery and assumes that 20% of the product $Zn(g)$ recombines with O_2 in the solar step.

Natural gas cost comprises 52 to 68% of the total cost of hydrogen production in large scale steam methane reforming plants [76], making the cost strongly dependent on the cost of natural gas. Hydrogen produced in a steam methane reforming plant that produces $22000\,kg$ of hydrogen per day has been calculated to cost $\$2.40/kg$ or $\$4.10/kg$ assuming natural gas prices of $\$7/GJ$ and $\$15/GJ$, respectively [77]. Using proportionality, and assuming that

[1] Efficiency is defined as the fraction of the solar energy reaching the heliostats that is stored in the hydrogen, based on the LHV in [1] and the HHV in [75].

Table 7.1: Key assumptions and findings from prior cost and efficiency analyses of the Zn/ZnO cycle.

	Steinfeld $(792\,kg/hr)$[1]	Charvin et al., $(250\,kg/hr)$[75]	Charvin et al., $(50\,kg/hr)$[75]
Plant size, energy and mass flows			
Concentration ratio, C	5,000 suns	5,000 suns	5,000 suns
Plant size (input to reactor) $[MW_{th}]$	90	55	11
Beam irradiation $[kWh_{th}/m^{2}\cdot yr)]$	2300	2000	2000
Heliostat area $[m^2]$	155,172	54,800	10,960
Efficiencies			
Optical efficiency, η_{optics}	58%	68.4%	not included
Cycle efficiency, η_{cycle}	29%	30.4%	not included
Global efficiency, η_{global}	17%	20.8%	not included
Assumptions			
Pump or work input	none	none	none
Solar step temperature $[K]$	2300	2000	2000
Reactor re-radiation losses	yes	yes	yes
Endothermic reaction losses	yes	yes	yes
Heat recovery from quenching	no	yes	yes
Heat recovery, exothermic reaction	none	complete	complete
Recombination of Zn & O_2	none	20%	20%
Efficiency of hydrolysis step	complete	complete	complete
Hydrogen energy content $[kJ/mol]$	241(LHV)	286 (HHV)	286 (HHV)
Cost			
Heliostat field $[M\$, \$150/m^2]$	23.28	8.22	1.65
Land $[M\$, \text{assuming } \$1/m^2]$	not included	0.28	0.06
Tower $[M\$]$	3.60	1.50	1.00
Tower reflector and CPCs $[M\$]$	5.30	not included	not included
Solar receiver-reactor $[M\$]$	7.00	2.00	1.00
Quencher $[M\$]$	3.00	not included	not included
Hydrolyzer $[M\$]$	4.00	1.00	0.50
Balance of plant, indirects $[M\$]$	8.90	2.00	1.00
H_2 storage $[M\$]$	not included	1.00	0.50
Total capital cost for solar H_2 $[M\$]$	55.08	16.00	5.70
Annual Cost			
Annual fixed charge rate $[M\$]$	15%	not included	not included
Capital cost for solar H_2 $[M\$]$	8.26	not included	not included
O&M cost for solar H_2 $[M\$]$	1.10	1.01	0.42
Total annual cost for solar H_2 $[M\$]$	9.36	1.01	0.42
Hydrogen production rate $[kg/hr]$	792	250	50
Hydrogen cost $[\$/kg]$	5.02	7.98	14.75

natural gas comprises 60% of the cost of H_2, a natural gas price of \$10/GJ will result in hydrogen costing \$3.02/kg. Natural gas prices are volatile and hard to predict. In July, 2008 the price of natural gas was \$13.84/GJ, and in March of 2009, the price was \$9.23/GJ [73]. In the near term—the next ten to twenty years—the cost of natural gas is expected to be \$7 − 12/GJ [73], and hydrogen produced by steam methane reforming is thus expected to cost between \$2.40 and \$3.60/kg. For the present analysis, the base cost of hydrogen produced by SMR is taken to be \$3/kg.

A simple analysis of the internalized cost of carbon required to make the Zn/ZnO cycle competitive with SMR is based on the relative costs discussed above and the amount of CO_2 emitted for every kilogram of hydrogen produced by SMR:

$$CT = \frac{c_{Zn/ZnO} - c_{SMR}}{e_{CO_2}} \tag{7.1}$$

where $CT\,[\$/tCO_2]$ is the required level of carbon tax to make SMR hydrogen cost as much as Zn/ZnO hydrogen, $c_{Zn/ZnO}$ is the cost per kilogram of hydrogen produced by the Zn/ZnO cycle, c_{SMR} is the cost of hydrogen produced by SMR, and $e_{CO_2}\,[tCO_2/kg\,H_2]$ is the equivalent CO_2 emissions from SMR, $0.0119\,tCO_2/kg\,H_2$ [78].

7.2.2 Required levels of public and private investments

Experience, or learning, curves, are graphical representations of the effect of learning-by-doing on prices in manufacturing and technology sectors. They are based on the premise that the cost of a technology decreases by a constant fraction, the learning rate (LR), with every doubling of the cumulative production or installed capacity. It is often more useful to discuss the experience curve in terms of the progress ratio (PR), which is the fractional multiplier by which the price drops with every doubling of the cumulative production, i.e. $PR = 1 - LR$. There is extensive empirical support for the existence of this relationship between experience and cost from a wide range of industrial fields, including technologies that transform or use energy [79, 80]. Thus, experience curves are used to predict how the price of hydrogen produced via the Zn/ZnO cycle can be expected to decrease with

accumulated experience, i.e. accumulated production.

Experience curves are expressed as

$$c_t = c_\circ \left(\frac{P_t}{P_\circ} \right)^{-E} \tag{7.2}$$

where c_t is the cost of the technology at time t, $c_\circ$ is the cost of the technology in the first batch of production (at $t = 0$), P_t is the total cumulative production at time t, and $P_\circ$ is initial production level or batch size. The learning index, E [79, 80], is given by

$$PR = 2^{-E}. \tag{7.3}$$

Generally, experience curves are used to predict future trends based on existing data on past technology production and costs. However, in the case of the Zn/ZnO cycle, there are no existing data. Thus, to estimate future costs of H_2, we rely on the literature for initial cost and batch size predictions [1, 75], and estimate a range of likely progress ratios based on similar technologies. The conclusions drawn from this analysis can therefore be considered relevant within the bounds of the assumptions made. Initial cost and production level are taken from Charvin et al.'s analysis of the small scale plant producing $50\,kg/hr$, in which H_2 is predicted to cost $\$14.75/kg$.

To identify appropriate progress ratios for this technology, we apply a combination of progress ratios observed for solar thermal power towers and two-step chemical reactors. Thus, the total progress ratio for the Zn/ZnO cycle, PR, is a combination of PR_{solar}, or the progress ratio for the solar tower, receiver, and heliostat technology; and the progress ratio of the Zn/ZnO reactors and periphery equipment, $PR_{reactor}$, as

$$PR = f_{solar} \cdot PR_{solar} + f_{reactor} \cdot PR_{reactor}, \tag{7.4}$$

where f_{solar} is the fraction of cost due to the solar concentrating components, and $f_{reactor}$ is the fraction of cost due to the Zn/ZnO cycle reactors and periphery. Both Steinfeld [1] and Charvin et al. [75] predict that approximately 25% of the total cost of the Zn/ZnO cycle will be due to the reactors, so $f_{solar} = 0.75$ and $f_{reactor} = 0.25$. No data exist for the progress ratio of the Zn/ZnO reactors, so the progress ratio for steam methane reforming

(0.73 ± 0.05) is assumed [81]. SMR is chosen because it, like the Zn/ZnO cycle, is a two-step chemical reaction.

There are also no data for the progress ratio for solar tower concentrating systems (tower, receiver, heliostats), but one study estimates that the progress ratio for electricity generated from a solar power tower is 0.9 ± 0.05 [82]. Because the power tower combines the solar concentrating system with a Rankine cycle electricity generator, the total progress ratio for the solar power tower, PR_{PT}, is assumed to be due to a combination of PR_{solar}, and the progress ratio for the Rankine cycle generator, PR_{elec}, as

$$PR_{PT} = f'_{solar} \cdot PR_{solar} + f_{elec} \cdot PR_{elec} \tag{7.5}$$

where f'_{solar} and f_{elec} are the fraction of costs due to the solar components and electricity generation components, respectively. In Eq. (7.5), PR_{solar} is the only unknown. In PS-10,[2] 46.8% of the total cost of the power tower was due to the steam turbine and electrical power generation system [83], so for this analysis $f_{elec} = 0.468$ and $f'_{solar} = 0.532$. In addition, PR_{elec} is $0.965 \pm .02$ [81]. The progress ratio for the solar components of the power tower, PR_{solar}, is calculated for the assumed values of f'_{solar} and f_{elec} and the stated ranges for PR_{elec} and PR_{PT}, and is found to be between 0.74 and 0.95. Using $0.74 \leq PR_{solar} \leq 0.95$ and $0.68 \leq PR_{reactor} \leq 0.78$ in Eq. (7.4), PR for the Zn/ZnO cycle is between 0.73 and 0.91. It is reasonable to assume $0.77 \leq PR \leq 0.87$, as the outer portions of the range represent the confluence of multiple extremes from the preceding analysis. In the present analysis we consider $PR = 0.77$, 0.82, and 0.87.

With the stated assumptions, the experience curve for the Zn/ZnO cycle is given by

$$c_t = 14.75 \left(\frac{P_t}{100000} \right)^{-E} \tag{7.6}$$

where $E = 0.377$, 0.286, and 0.201 for $PR = 0.77$, 0.82, and 0.87, respectively. The cumulative production, P_t, can be assumed without reference to a time-frame, as is typical in experience curve analysis. The integrated difference between the cost of H_2 produced by the Zn/ZnO cycle and that produced by SMR is the additional public and private investment

[2] An 11 MW_e installed capacity solar concentrating power plant that went on line near Seville, Spain in 2007.

needed over the cost of SMR to bring the Zn/ZnO cycle to cost competitiveness, starting at the point when a plant begins operation producing $50\,kg/hr$, or $100000\,kg/yr$[3]. There is certainly public and private investment in the technology prior to when this plant begins operation; however, that investment is is external to this analysis.

7.2.3 Predicting future costs and break even year

The price of hydrogen produced by the Zn/ZnO cycle as a function of time is predicted by combining the learning curve data (which express price as a function of accumulated production) with implementation time frames (which express accumulated experience as a function of time). The experience curve for $PR = 0.82$ is used in this analysis. Because it is a new and unproven technology with high capital costs and uncertain revenue, and because the hydrogen produced by the Zn/ZnO cycle will not initially be economically competitive, the implementation time frame will depend on the level of direct government support for the technology. This support will come in the form of incentive policies. We assume three possible policy scenarios defined by three rates of implementation: a minimal input policy, a mid-range policy, and an aggressive policy. The implementation time frames corresponding to the three policy scenarios are chosen to bracket the range of potential implementation time frames. The aggressive policy scenario is defined by the fastest imaginable implementation time frame, while the minimal input policy scenario is defined by a very slow implementation time frame.

All three policy scenarios require the same amount of public and private investment to reach economic competitiveness, as the required investment is determined by the experience curve. The differences in these policies are in the rates at which these investments are made (i.e. the rate of technology demonstration and commercialization). Under the minimal input policy, either few resources are put to renewable energy in general, or the resources are directed almost entirely to other renewable technologies. The mid-range policy scenario assumes a moderate level of resources being devoted to demonstration and small

[3]Based on 2000 full power hours per year.

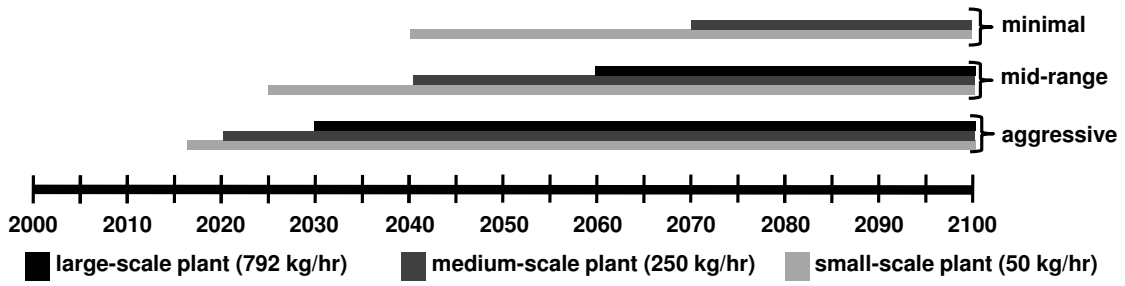

Figure 7.1: Time line for implementation of Zn/ZnO cycle technology under the three policy scenarios

scale implementation of the technology in the near to mid term, with the goal of economic viability by mid-century. The Zn/ZnO cycle is assumed to be one of many technologies being cultivated. The aggressive policy scenario assumes high levels of resources devoted to the technology immediately, including strong investments in R&D, with the goal of making the technology economically competitive well before mid-century.

Under each scenario, implementation of the technology is assumed to occur in three stages. First, one initial, small commercial plant goes on line, producing H_2 at a rate of $50\,kg/hr$, corresponding to the small plant analyzed in Charvin et al. [75]. Second, a mid sized plant goes into operation, producing H_2 at $250\,kg/hr$, corresponding to the larger plant size they analyzed [75]. Finally, a large scale plant goes on line, producing H_2 at a rate of $792\,kg/hr$, corresponding to the plant analyzed in Steinfeld [1]. If all three plants are in operation, these plants would produce a total of $3.8 \times 10^6\,kg$ of H_2 annually. This analysis only includes the first few plants to be implemented because later plants will be driven by economics, not policy, as will be discussed later.

The time line of implementation assumed for each policy scenario is depicted graphically inFig. 7.1. Under the aggressive policy, the small, medium, and large scale solar H_2 production plants are rapidly built, so that the large scale plant goes on line in 2030. Under the mid-range policy scenario, the commercial plants are deployed steadily, with the small-scale plant starting operation in 2025, the mid-scale plant in 2040, and the large scale plant in 2060. Under the minimal input policy, deployment of the small scale reactor only occurs once the need for solar fuels becomes acute, assumed here to be 2040. The medium sized

reactor is built for operation in 2070, once the learning associated with the small scale plant brings prices down to economically competitive levels. A large scale reactor is not assumed to be built in this century under the minimal input policy scenario. These implementation time frames are chosen to represent different rates of implementation of the technology that could result from different levels of incentive policy and support for the technology. In reality, the initial plant sizes may be different, or more medium plants may begin operating before a large scale plants is built. Any additional plants would result in an earlier break even year for the Zn/ZnO cycle.

To determine the year in which H_2 produced by the Zn/ZnO cycle becomes cost competitive with that produced by SMR, the price of H_2 produced by SMR is also predicted. Fifty-two to 68% of the cost of H_2 produced by SMR is due to the cost of methane. The remaining cost is the cost of the plant and O&M. This remaining cost is subject to an experience curve effect of its own with $PR = 0.73$ [81].

The cost of H_2 produced by SMR for each year is calculated as

$$c_t = (b \cdot c_{t-1})i_t + (1 - b) \cdot c_{O\&M,t} \tag{7.7}$$

where c_t is the cost of H_2 produced by SMR at time, t, b is the fraction of the cost due to natural gas, $c_{O\&M,t}$ is determined from the SMR experience curve, and i_t is the annual percent increase in the cost of natural gas for the corresponding year. Future cumulative production levels of H_2 produced by SMR were extrapolated from data presented in Schoots et al. [80], in which SMR production increased by approximately 9.1% each year. The cost is projected starting in 2007, assuming costs of $\$3/kg$ for H_2 produced by SMR, and 2007 cumulative production of $4.18 \times 10^{10}\, kg$ [80]. The price of natural gas from now until 2030 has been predicted by the Energy Information Administration (EIA) [73], and these data are used to calculate i_t until 2030. The average annual increase from 2015 to 2030 in the EIA's predicted costs is used as i_t for 2030 and beyond.

Table 7.2: The required public and private investments and necessary cumulative H_2 production for the Zn/ZnO cycle to become economically competitive, given PR=0.77, 0.82, 0.87, $c_\circ$=\$14.75/kg, and $P_\circ$=100000 kg.

	Necessary cumulative production	Required public and private investment
$PR = 0.77$	$7.9 \times 10^6\, kg$	\$13 million
$PR = 0.82$	$3.0 \times 10^7\, kg$	\$28 million
$PR = 0.87$	$3.2 \times 10^8\, kg$	\$46 million

7.3 Results

7.3.1 Required level of carbon taxation

For hydrogen produced via the Zn/ZnO cycle to be economically competitive with that produced by SMR under a carbon tax policy only, the level of taxation must be sufficient to make up the difference in production costs. Assuming the lowest predicted H_2 cost for the Zn/ZnO cycle, \$5.02 [1], and the highest predicted cost of SMR, $\$3.60/kg$, the cost of carbon would need to be $\$119/tCO_2$. This level of carbon taxation is significantly higher than has been instituted in European countries or is likely to be instated elsewhere, including the U.S., China, and India. A more conservative assumption for the near term cost of H_2 produced by the Zn/ZnO cycle would be the cost of producing it in the small scale plant producing $50\, kg/hr$. Under this assumption, the cost of Zn/ZnO cycle hydrogen is $\$14.75/kg$, and the carbon tax would have to be $\$987/tCO_2$, assuming $\$3/kg$ for H_2 produced by SMR. A carbon tax alone will not be sufficient to make the Zn/ZnO cycle economically competitive.

7.3.2 Required public and private investments

The results of the experience curve analysis are shown in Fig. 7.2. The initial cost per kg of H_2 is taken to be $\$14.75\,/kg$, and the initial batch size is assumed to be $100000\, kg\ H_2$, both consistent with Charvin et al. [75]. The level of cumulative production at which the Zn/ZnO cycle becomes cost competitive with SMR is listed in Table 7.2 for $PR = 0.77$, 0.82, 0.87. If

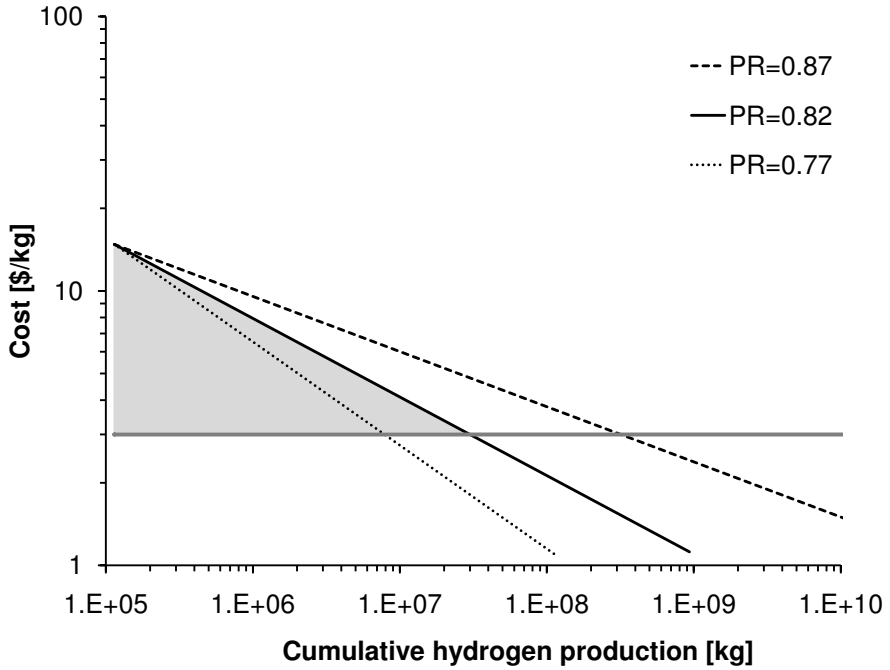

Figure 7.2: Learning curves for the production of hydrogen via the Zn/ZnO cycle assuming progress rates (PR) of 0.87, 0.82, and 0.77 and an initial cost of \$14.75/kg and initial batch size of 100000 kg.

the technology proves to have a lower progress ratio, corresponding to a higher learning rate, less cumulative production is needed to achieve economic competitiveness. The almost two orders of magnitude difference between the necessary cumulative production for $PR = 0.77$ and for $PR = 0.87$ illustrates the sensitivity of the required investment to the assumed value of PR.

The additional investment needed to bring the Zn/ZnO cycle down its experience curve is the integrated difference in the cost of producing H_2 by the Zn/ZnO cycle instead of SMR, i.e., the area between the experience curve and the SMR line in Fig. 7.2, shaded for $PR = 0.82$. The approximate required public and private investments needed to bring the cost down the learning curve, without inflation, and given our assumptions for the initial conditions and the progress ratio, are listed in Table 7.2. It should be noted that in their analysis, Charvin et al. [75] assumed a fair amount of technological improvements in order to estimate a reasonable cost of hydrogen produced by the Zn/ZnO cycle, and the experience curves in Fig. 7.2 do not include the public and private investments required to bring the

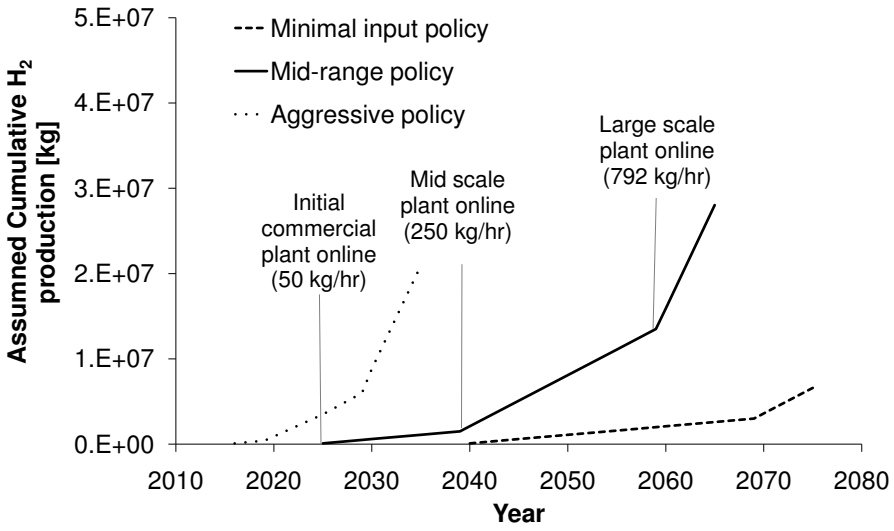

Figure 7.3: Assumed cumulative H_2 production under an aggressive policy scenario, a mid-range policy scenario, and a minimal policy scenario for the Zn/ZnO cycle technology assuming PR=0.82. Curves extend up to 5 years after initiation of the last assumed plant.

technology to that stage. They do show what additional investment would be needed to make the technology economically competitive with SMR starting when an initial, small scale plant begins operation (assuming current natural gas prices). However, we find that a public and private investment between 13 and 46 million dollars (neglecting inflation) would be sufficient to bring the price of hydrogen produced by the Zn/ZnO cycle from \$14.75 for the initial small scale commercial project to \$3.00. This level of investment would be a relatively small portion of total government energy-specific expenditures, which were \$16.6 billion in the U.S. in 2007 [73].

7.3.3 Break even year

To predict the year in which the H_2 produced via the Zn/ZnO cycle will become cost competitive with SMR, the learning curve for $PR = 0.82$ is combined with predicted implementation time-frames based on three policy scenarios—a minimal input policy, a mid-range policy, and an aggressive policy scenario. Fig. 7.3 shows the assumed cumulative H_2 production by the Zn/ZnO cycle with time under each of the three policy scenarios. The inflection

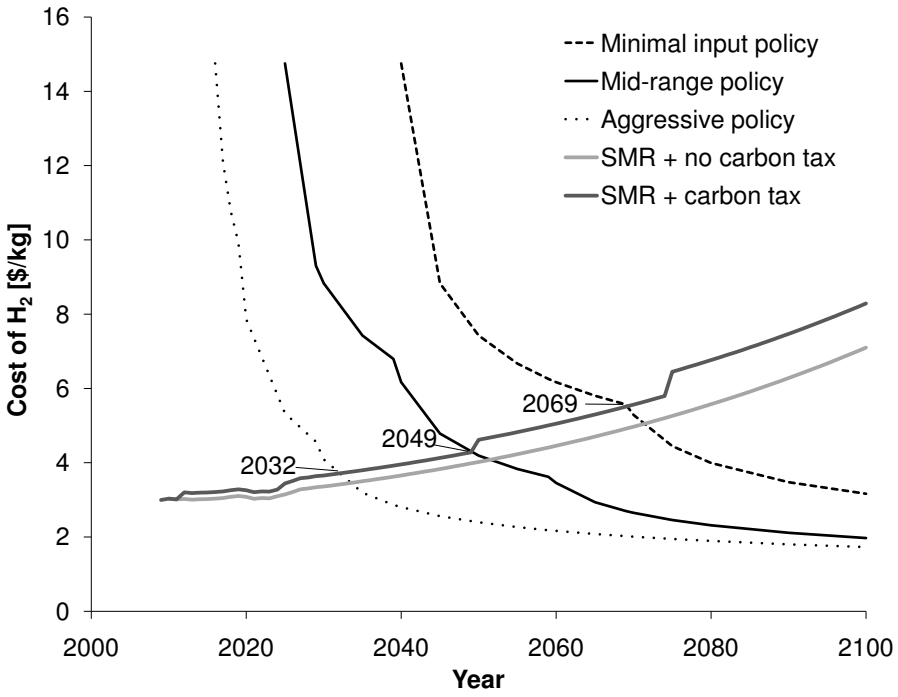

Figure 7.4: The cost of hydrogen produced via the Zn/ZnO cycle (assuming PR=0.82) under different policy scenarios and SMR with and without a carbon tax. The intersections of the cost curves for the two H_2 production methods indicate the year in which solar H_2 becomes competitive for each policy scenario combined with a gradually increasing carbon tax.

points correspond to the addition of the small, medium, and large scale plants, and are labeled for the mid-range policy scenario. The curves extend up to five years after initiation of the last assumed plant. It should be noted that these policy scenarios do not include assumptions about additional H_2 production plants, though they are likely to be built once the technology becomes economically competitive. Construction of additional plants will be motivated primarily by economic factors, not policy. The projected price of solar H_2 as a function of time under the three policy scenarios is plotted in Fig. 7.4. The initial steep decline in price results from the relatively frequent doubling in cumulative production at this early stage. The prices begin to level off around 2025 under the aggressive policy scenario, 2040 under the mid-range policy scenario, and 2055 under the minimal input policy scenario.

The intersections of the cost curves for H_2 produced by the Zn/ZnO cycle with the cost curves of H_2 produced by SMR indicate the break even year when solar H_2 becomes economically competitive. Figure 7.4 shows the cost of H_2 produced by both methods from

2010 through the end of the century. The cost of H_2 produced by the Zn/ZnO cycle is shown over time for each of the three policy scenarios. The cost of H_2 produced by SMR is shown without a carbon tax, and with a carbon tax that increases with time.The carbon tax is assumed to be $\$15\,/tCO_2$ starting in 2012, increasing to $\$25\,/tCO_2$ in 2025, $\$50\,/tCO_2$ in 2050, and $\$100\,/tCO_2$ in 2075. As can be seen in Fig. 7.4, an increasing carbon tax combined with the aggressive policy, results in solar H_2 becoming competitive in 2032. The carbon tax combined with the mid-range policy results in H_2 becoming competitive by 2049. The carbon tax combined with the minimal input policy results in the technology becoming competitive in 2069. Without the carbon tax, the corresponding dates are 2034, 2052, and 2072.

7.3.4 Sensitivity Analysis

Five major assumptions were made in the present analysis: the value of the Zn/ZnO progress ratio, the initial cost and batch size of H_2 produced by the Zn/ZnO cycle, the initial cost of H_2 produced by SMR, and the fraction of the cost of SMR H_2 that is due to the cost of natural gas. A sensitivity analysis of these assumptions was conducted in terms of the change in predicted break even year, and the results are summarized in Fig. 7.5.

The sensitivity analysis considers a 5% change in the progress ratio (or 0.82 ± 0.05), a 30% change in the initial cost of hydrogen produced by the Zn/ZnO cycle (or $\$14.75 \pm 4.42$), a 30% change in the initial production level of hydrogen produced by the Zn/ZnO cycle (or $100000 \pm 30000\,kg/yr$), a 20% change in the initial cost of hydrogen produced by SMR (or $\$3 \pm 0.6$), and a 15% change in the cost of hydrogen produced by SMR that is due to the cost of methane (or $60\% \pm 9\%$). These values were chosen to cover the reasonable range for each assumption. The break even year was found to be relatively consistent over the range of reasonable assumptions; generally varying by less than a decade.

A 5% increase in PR results in a predicted "break even" point six to ten years later, and a 5% decrease in PR results in the predicted break even point decreasing by five to ten years. The high degree of uncertainty in the initial cost of H_2 produced by the Zn/ZnO

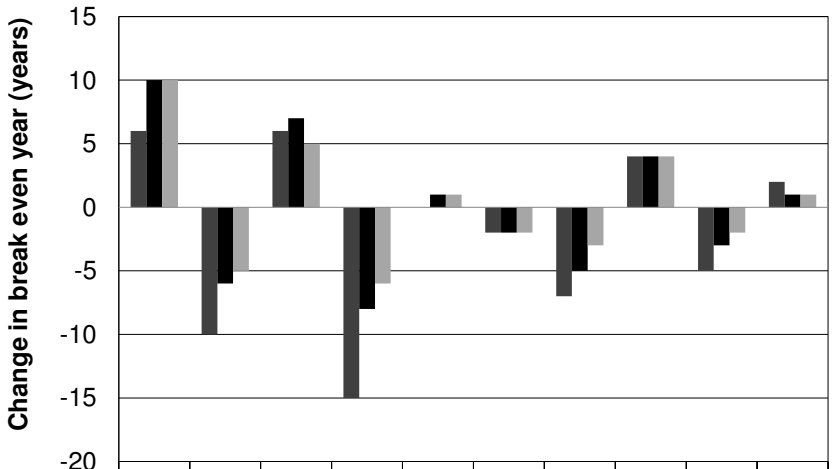

	5%	-5%	30%	-30%	30%	-30%	20%	-20%	15%	-15%
	Zn/ZnO progress ratio		Zn/ZnO initial cost		Zn/ZnO initial batch size		SMR initial cost		SMR cost from methane	
minimal input	6	-10	6	-15	0	-2	-7	4	-5	2
mid-range	10	-6	7	-8	1	-2	-5	4	-3	1
aggressive	10	-5	5	-6	1	-2	-3	4	-2	1

Figure 7.5: The sensitivity of the predicted "break even" year to the five major assumptions.

cycle results in changes of five to six years if the initial cost is 30% higher, and six to 15 years if the initial cost is 30% lower. The analysis is also relatively sensitive to the assumed value of the initial cost of hydrogen produced by SMR, with a 20% increase in price reducing the break even point by three to seven years, and a 20% reduction in price resulting in a four year increase in the break even point. The effect of a 30% change in the initial batch size or a 15% change in the SMR cost fraction due to natural gas result in changes in the predicted break even point of five years or less. In all but one case, the change in assumption results in a change in break even time within a decade, and in all cases, the change is within 15 years. Changing all variables in the Zn/ZnO cycle analysis at once results in changes in the break even by as little as nine years and no more than 24 years, while changing both variables from the SMR cost analysis at once results in changes of five to ten years. It should be noted that the likely hood of all, or even most, variables having values in the extremes of the range of likely values, all in a manner that favors one technology over the other, is very unlikely. Thus, this analysis is relatively robust, as changes representing the reasonable

range of assumptions do not result in significant changes in the predicted break even year.

7.4 Conclusion

Given the assumptions stated in this analysis and assuming appropriate technical advancement is achieved with ongoing research, hydrogen produced via the Zn/ZnO thermochemical cycle can become economically viable in the latter part of the century, even with a relatively modest public and private investment pace (i.e. the minimal input policy). A proactive approach (i.e. the mid-range policy) should help to ensure that the technology is economically competitive around mid-century. An aggressive investment pace (i.e. the aggressive policy) could result in a break even year significantly before mid-century. The time frames associated with the three policy scenarios effectively bracket the potential implementation rates under a range of incentive policies.

The year 2050 is often used as a bench mark for climate change policy, a time by which we should have stabilized the carbon in the atmosphere and after which we should start to reduce atmospheric concentrations of CO_2 and other greenhouse gases [69]. Thus, it would be prudent to invest in solutions like the solar H_2 process, so that when we reach 2050, we have a wide range of economically competitive renewable energy technologies. Direct government support for R&D, demonstration, and early commercialization will be required for the technology to reach economic competitiveness with hydrogen produced by SMR. Further commercialization will depend on incentive policies such as tax breaks, purchase guarantees, and low interest rate loans. To help ensure that additional experience has the expected effect on cost, incentive policies must be clearly defined and consistent and include a pathway for transition to a competitive market structure [72].

An aggressive policy scenario is the most successful at quickly making the Zn/ZnO cycle cost competitive, but it should be considered carefully. If an aggressive approach to this technology is at the expense of other potential renewable energy technologies, then it may be counter to the overall goal of reducing greenhouse gas emissions. However, in a scenario

in which renewable energy technologies are being pursued aggressively across the board, the aggressive policy may be appropriate. In that case, it would be important to consider that rapid investment and deployment of a technology can disrupt the experience curve effect, decreasing the learning rate or, in some cases, initially causing prices to increase rather than decrease with accumulated experience.

It is interesting to note the relatively small effect of the carbon tax on the time at which the solar H_2 process becomes economically competitive. The $0.0119\,tCO_2$ emitted per kg of hydrogen produced, combined with a tax of $\$50/tCO_2$ results in an additional \$0.60 added to the cost of a kg of H_2 produced by SMR. In contrast, the cost of solar H_2 is predicted to decrease from approximately \$15 in 2025 to approximately \$4 in 2050. Thus, the effect of experience on the price of solar H_2 is much more significant than the effect of the price of carbon on H_2 produced via SMR. This effect is due to the emergent nature of the Zn/ZnO technology. The cost of a more mature technology would decrease much more slowly, closer to the order of magnitude of the carbon tax.

This study focused on the economic viability of H_2 produced via the Zn/ZnO cycle under different policy scenarios. Under the assumptions used in this analysis and given policies that lead to an initial, small scale Zn/ZnO hydrogen production plant in operation in 2025 and a mid-sized plant in operation in 2040, hydrogen produced using this technology should be competitive by mid-century. At that pace, the Zn/ZnO cycle would be positioned to produce a solar fuel to help meet goals of reducing atmospheric greenhouse gas concentrations during the second half of the century. Under a slower policy scenario, in which a small scale plant is in operation by 2040, the Zn/ZnO cycle is estimated to be able to competitively produce hydrogen in 2069, just before initiation of a mid-sized plant. Thus, the Zn/ZnO thermochemical cycle has the potential to help reduce greenhouse gas emissions in the second half of the century.

Estimations of near term costs of hydrogen produced by SMR [76, 77] compared with projected costs of hydrogen produced by the Zn/ZnO cycle [1, 75] make clear that a politically feasible level of carbon taxation would not be sufficient to make the Zn/ZnO cycle competitive with SMR. Thus, for hydrogen produced by the Zn/ZnO cycle to become cost

competitive, public and private investment in the technology will be required to bridge the financial gap. Direct government support for research, development, and demonstration projects and early commercialization followed by policies that provide incentives for private investment in the Zn/ZnO cycle technology—such as tax breaks, purchase guarantees, and low interest rate loans—will be crucial in bringing the cost of H_2 produced via the Zn/ZnO cycle down. Incentive policies are often required for emerging energy technologies, in which the capital costs are high and the revenue stream may be uncertain, and many present day technologies initially relied on this type of government support. However, history also shows that if the most economically efficient path to cost competitiveness is desired, very rapid implementation of the technology or policies that result in non-competitive markets can undermine the learning effect for a technology [72]. Thus, in designing policies, the benefits of rapid implementation should be weighed against these potential economic inefficiencies.

The most striking conclusion that comes out of the experience curve analysis is the relatively low investment needed to bring the technology to cost competitiveness. Given the assumptions in the present analysis, the public and private investment needed to become cost competitive is $29 million (neglecting inflation), starting with construction of the first, small scale plant. This number does not include any investment in research, development and demonstration that occurred prior to the construction of the initial small plant, and it is only the investment above what it would have cost to produce the same amount of H_2 by SMR at $\$3/kg$. It is perhaps more intuitive to think about how many concentrating solar thermal Zn/ZnO plants need to be built in order to reach cost competitiveness. Under all three policy scenarios, the technology is projected to become cost competitive around the time that the second, mid-sized plant begins operation. The small and mid-sized plants are projected to cost $5.7 million and $16 million to build, and $0.42 million and $1 million for annual operation and maintenance, respectively [75]. This is a very hopeful conclusion for this, and other, solar thermochemical cycles as they reach technological maturity.

Chapter 8

Conclusions

8.1 Summary and Conclusions

Both technical and economic challenges of the Zn/ZnO two-step thermochemical hydrogen production cycle are investigated in this study. Technically, complete hydrolysis of Zn in the hydrogen production step remains a major barrier to implementation, and much attention has been given to Zn nano-scale reacting aerosols as a solution. Smaller particles favor faster reaction kinetics, and because they can be entrained and reacted in a gas flow, a continuous controllable process is possible. However, success of this continuous process depends on achieving high particle yields and high conversions in the aerosol, neither of which have yet been achieved in laboratory reactors.

A new reactor concept based on transverse jet flow fields is investigated. In the transverse jet reactor, evaporated Zn entrained in an Ar carrier gas issues vertically into the horizontal tubular reactor through which cooler H_2O and Ar flow. Particles are formed in the presence of steam at $\sim 450\,K$. Computational fluid dynamics (CFD) modeling was used in the reactor design stage to ascertain achievable quench rates in this type of reactor at expected operating conditions. The dominant feature of transverse jets, the counter-rotating vortex pair, is captured in the model and it drives mixing between the jet and quenching mixture of Ar and H_2O, resulting in the predicted quench rates of $10^4\,K/s$.

CFD modeling is also used in conjunction with experiments to demonstrate the success

of the transverse jet reactor at achieving three objectives: rapid quenching of the Zn vapor, well mixed reactants, and maximized particle yields on the filter through control of the jet trajectory. The jet trajectory depends on the effective velocity ratio, R, the square root of the ratio of the kinetic energy of the jet to that of the cross-flow. Experiments are conducted over $3.04 \leq R \leq 12.15$ for $y_{H_2O} = 0$ and 0.12 with matching numerical models for $R = 3.04$, 4.25, 4.50, and 5.81. The CFD models show that quench rates of $2{\times}10^4\, K/s$ are achieved and reactants are well mixed at all four effective velocity ratios modeled. Measured temperatures in the jet as it issues into the reactor agree well with temperatures predicted by the model, lending credence to the modeled quench rates. Furthermore, the models indicate that the trajectory of the jet can be controlled via R so that the majority of the Zn mass is directed down the center of the reactor, not near the reactor walls. The objective of keeping Zn away from the walls is to reduce particle deposition in the reactor and increase particle yields on the filter. In experiments, maximum particle yields of 93% of the mass entering the reactor are obtained for $R = 4.5$.

Hydrolysis experiments conducted in the transverse jet reactor with $R = 4.5$ at $418\, K$, $573\, K$, $603\, K$, and $713\, K$ are used to assess the mechanisms of particle growth and hydrolysis in the aerosol. Residence times in the reactor are $\sim 12\, s$ at $418\, K$ and $\sim 5\, s$ for experiments at $573\, K$ and above. Experiments are conducted with and without steam to assess the effect of the reacting gas on particle morphology. SEM images of particles collected on a filter downstream from the reaction zone indicate that particle growth is dominated by condensation, resulting in hexagonal particles generally with lengths across their hexagonal face of $300\, nm$ to $1\, \mu m$ in experiments with stream, and 1 to $3\, \mu m$ in experiments without steam. SEM images indicate that in hydrolysis experiments, a ZnO shell forms on the surface of particles early on, protecting them from re-evaporation. Hydrolysis experiments at higher temperatures show less evidence of evaporation, than at lower temperatures, which is attributed to the faster kinetics at higher temperatures that result in more ZnO on the particle surface. Filter deposits from an experiment above T_{sat} without steam are primarily Zn nanowires, which form on the filter from Zn vapor [67, 68].

The conversion in the aerosol is $< 7\%$ and decreases with reaction zone temperature. The

overall conversion ranges from 11% at 418 K to 49% at 713 K. The difference between overall conversion and conversion in the aerosol is attributed to heterogeneous Zn vapor hydrolysis on the walls of the reaction zone and near the jet inlet, as evidenced by characteristic deposits. Visual observation proves heterogeneous hydrolysis occurs on the reactor walls; it is inferred that the heterogeneous Zn vapor reaction also occurs on the surface of aerosol particles. Particle yield decreases with increasing reaction zone temperature due to the greater amounts of ZnO deposited on the reaction zone walls. However at all temperatures, high particle yields are attained—60 to 93% in all experiments, and 72 to 82% in hydrolysis experiments conducted in configuration B. Further, particle deposition on the walls of the reaction zone is eliminated for temperatures of 573 K and above. Thus, the transverse jet reactor significantly reduces particle deposition on the walls, an important step towards the success of the continuous aerosol process. However, complete conversion of particles in the aerosol remains a significant challenge.

In the economic and policy study of the Zn/ZnO cycle, the level of carbon taxation necessary to make the cycle competitive with hydrogen production via methane reforming is determined. In addition, the time frame for economic viability is assessed through the use of experience curves under minimal input, mid-range, and aggressive incentive policy scenarios. Prior work projects that hydrogen produced by the Zn/ZnO cycle will cost between 5.02/kg and 14.75/kg, compared with 2.40–3.60/kg for steam methane reforming. Overcoming this cost difference would require a carbon tax of \$119–\$987/$tCO2$, which is significantly higher than is likely to be implemented in most countries. For the technology to become cost competitive, incentive policies that lead to early implementation of solar hydrogen plants will be necessary to allow the experience effect to draw down the price. Under such policies, a learning curve analysis suggests that hydrogen produced via the Zn/ZnO cycle could become economically viable between 2032 and 2069, depending on how aggressively the policies encourage the emerging technology. Thus, once the technical challenges are realized, the Zn/ZnO cycle has the potential to be economically viable by mid-century if incentive policies—such as direct financial support, purchase guarantees, low interest rate loans, and tax breaks—are used to support initial projects.

8.2 Discussion

In Chapter 1, three technical objectives were laid out for this study: first, the design and implementation of a reactor that achieves high filter yields without sacrificing quench rates and mixing of the reactants; second, improved conversion in the aerosol; and third, characterizing the evolution of the aerosol as particles grow and react. The transverse jet reactor succeeds at achieving high particle yields and a quench rate of $2 \times 10^4\, K/s$. The vortical structures inherent in transverse jets, especially the counter-rotating vortex pair, drive mixing and quenching, despite $Re_D \approx 200$. However, the conversion in the aerosol is $< 7\%$.

Although particles were too large to sample with the SMPS, SEM images, data, and observations from the hydrolysis experiments do provide enough information to paint a picture of particle formation and evolution in the transverse jet reactor. From these data and observations, it is deduced that significant Zn vapor remains after the initial quench, resulting in particle growth that is dominated by condensation in a 2-D layer by layer growth mechanism [5, 66]. The resulting particles are hexagonal. Early on, possibly while still in the mixing zone or at the beginning of the reaction zone, ZnO forms on the surface of the particle either by direct hydrolysis of the particle or via heterogeneous Zn vapor hydrolysis. This ZnO layer impedes re-evaporation of particles, even when $T_{RZ} > T_{sat}$. As it enters the reaction zone, the aerosol still has some Zn vapor in it; how much depends on the temperatures in the reactor and the length of the mixing zone. This Zn vapor reacts with H_2O on the the walls of the reaction zone and the surface of the aerosol particles. The heterogeneous Zn vapor reaction ceases when temperatures drop below $\sim 600\, K$ or Zn vapor is no longer available. The presence of steam in the aerosol also impedes particle growth.

The promise of the Zn aerosol hydrolysis process is based on the idea that very small particles can be formed in a reactor, entrained in a reacting gas, and delivered fully reacted, as part of a continuous process, for dissociation into Zn and O_2 in the solar step of the cycle without significant particle deposition on reactor walls. Further, the success of the process relies on kinetics that are significantly higher than those measured via TGA [13, 24]. This

study makes stark the difficulty of producing small particles for this process, especially while balancing goals of high particle yields and long residence times. In fact, in all reactors in which Zn particles are nucleated and subsequently reacted, the reported morphologies of particles collected on the filter are either hexagonal particles around $500\,nm$ to $1\,\mu m$ [21, 22] or nanowires, often mixed with large, layered structures [19, 22, 25, 44]. Across the range of quench rates investigated, no study reported an experiment that produced agglomerate particles with small characteristic lengths. In each experiment in which nanowires were produced, total residence times in the reactor were approximately $1\,s$ or less. Hexagonal particles were produced in reactors with residence times of approximately $5\,s$. It is possible that in all cases, significant Zn vapor remained after the initial quenching process; in reactors with residence times of $\sim 5\,s$, hexagonal particles grew by condensation, while in reactors with residence times of $\sim 1\,s$, Zn nanowires formed from the vapor on the downstream filters. If this is the case, Zn vapor hydrolysis is likely to have played a role in measured overall and aerosol conversions in other reactors as well.

This study illustrates another challenge in aerosol reactors. When Zn vapor remains in the aerosol, it may react heterogeneously with H_2O on the surface of particles, increasing the thickness of the ZnO layer without reacting the particulate Zn. Any further conversion of particles would therefore have to happen via the diffusion limited reaction, and as long as there is Zn vapor in the aerosol, the heterogeneous vapor reaction will be more kinetically favorable than the diffusion limited conversion of Zn in the center of the particle. Complete conversion in this regime is very slow, even for nano-scale particles [13], and sufficient residence times may not be achievable in aerosol reactors.

8.3 Recommendations for Further Study

Smaller particles can theoretically be achieved with lower concentrations of Zn vapor entering the reactor, a faster quench rate, and a quench to a temperature farther below T_{sat}. There are opportunities for investigating ways to decrease particle size in the transverse jet reactor. An investigation of the effect of lower Zn evaporation rates on particle size, and

determination of the Zn concentrations required for small particle formation would be of interest. The theoretical maximum hydrogen production rate decreases with Zn concentration, so there are practical limitations to how low Zn concentration should be.

In addition to hydrogen formation via the Zn/ZnO cycle, researchers are also investigating carbon monoxide (CO) production:

$$Zn + CO_2 \rightarrow ZnO + CO \tag{8.1}$$

A quenching mixture of CO_2 and Ar could enter the transverse jet reactor at much lower temperatures, relative to the temperatures required for H_2O and Ar mixtures. Lower quenching gas temperatures should provide faster quench rate to a temperature farther below T_{sat}, resulting in a higher supersaturation ratio and the formation of smaller particles with less remaining Zn vapor [28].

That the overall hydrogen production in the transverse jet aerosol reactor was dominated by heterogeneous Zn vapor hydrolysis illustrates the potential of the heterogeneous vapor process. Unlike the aerosol process, complete and near complete conversion by heterogeneous Zn vapor hydrolysis has been demonstrated in current and past work at the University of Minnesota and elsewhere [21, 45]. However, it is also well established that ZnO produced via the heterogeneous vapor reaction is difficult to remove from the surface on which it forms, a significant challenge given the importance of cycling product ZnO back to the solar step of the thermochemical cycle. However, this study suggests an interesting way to potentially combine the benefits of the aerosol process with those of heterogeneous Zn vapor hydrolysis. An aerosol reactor could be designed with the goal of heterogeneous Zn hydrolysis on the surface of ZnO aerosol particles. The product particles would be pure ZnO, some of which would be cycled back to the solar step of the cycle and the rest could be re-used in the aerosol reactor. The design and investigation of this type of aerosol process is an exciting area for future research.

In terms of the economic and policy area of study, an elaboration of the comparison between hydrogen produced via the Zn/ZnO cycle and via other renewable processes is of interest. Specifically, an extension of the learning curve analysis to include the learning curve

for electrolysis using wind and photovoltaic electricity would provide an important point of comparison for the Zn/ZnO cycle. In addition, an investigation of the economics and policy implications of the production of synthesis gas (a mixture of CO and H_2) via metal oxide cycles compared to production by gasification processes or steam methane reforming would provide an interesting perspective on the future of solar fuels.

Bibliography

[1] Steinfeld, A. "Solar hydrogen production via a two-step water-splitting thermochemical cycle based on Zn-ZnO redox reactions." *Internation Journal of Hydrogen Energy*, 27: pp. 611–619, 2002.

[2] Steinfeld, A. "Solar thermochemical production of hydrogen: a review." *Solar Energy*, 78: pp. 603–615, 2005.

[3] Keunecke, M., Meier, A., and Palumbo, R. "Solar thermal decomposition of zinc oxide: an initial investigation of the recombination reaction in the temperature range 1100-1250 K." *Chemical Engineering Science*, 59: pp. 2695–2704, 2004.

[4] Muller, R., Haeberling, P., and Palumbo, R. D. "Further advances toward the development of a direct heating solar thermal chemical reactor for the thermal dissociation of ZnO(s)." *Solar Energy*, 80: pp. 500–511, 2006.

[5] Weidenkaff, A., Steinfeld, A., Wokaun, A., Auer, P., Eichler, B., and Reller, A. "Direct solar thermal dissocation of zinc oxide: condensation and crysallisation of zinc in the presence of oxygen." *Solar Energy*, 65: pp. 59–69, 1999.

[6] Gstoehl, D., Brambilla, A., Schunk, L. O., and Steinfeld, A. "A quenching apparatus for the gaseous products of the solar thermal dissociation of ZnO." *Journal of Materials Science*, 43: pp. 4729–4736, 2008.

[7] Delalu, H., Vingalou, J., Elkhatib, M., and Metz, R. "Kinetics and modeling of diffusion phenomena occuring during the complete oxidation of zinc powder: influence of

granulometry, temperature and relative humidity of the oxidizing fluid." *Solid State Sciences*, 2: p. 2, 2000.

[8] Alimenti, G., Gschaider, M., Bazan, J., and Ferreira, M. "Theoretical and experimental study of the interaction of O_2 and H_2O with metallic zinc - discussion of the initial step of oxide formation." *Journal of Colloid and Interface Science*, 276: pp. 24–38, 2004.

[9] Bazan, J., Gschaider, M., and Alimenti, G. "Gravimetric study of interaction of water vapour with metallic zinc." *Journal of Thermal Analysis and Calorimetry*, 55: pp. 569–579, 1999.

[10] Berman, A. and Epstein, M. "The kinetics of hydrogen production in the oxidation of liquid zinc with water vapor." *International Journal of Hydrogen Energy*, 25: pp. 957–967, 2000.

[11] Weidenkaff, A., Rellera, A., Wokaunb, A., and Steinfeld, A. "Thermogravimetric analysis of the ZnO/Zn water splitting cycle." *Thermochemica Acta*, 359: pp. 69–75, 2000.

[12] Vishnevetsky, I. and Epstein, M. "Production of hydrogen from solar zinc in steam atmosphere." *International Journal of Hydrogen Energy*, 32: pp. 2791–2802, 2007.

[13] Ernst, F. O., Steinfeld, A., and Pratsinis, S. "Hydrolysis rate of submicron Zn particles for solar H_2 synthesis." *International Journal of Hydrogen Energy*, 34: pp. 1166–1175, 2009.

[14] Park, K., Lee, D., Rai, A., Mukherjee, D., and Zachariah, M. "Size-resolved kinetic measurements of aluminum nanoparticle oxidation with single particle mass spectrometry." *Journal of Physical Chemistry*, 109: pp. 7290–7299, 2005.

[15] Rai, A., Park, K., Zhou, L., and Zachariah, M. "Understanding the mechanism of aluminium nanoparticle oxidation." *Combustion Theory and Modelling*, 10(5): pp. 843–859, 2006.

[16] Mahadevan, R., Lee, D., Sakurai, H., and Zachariah, M. "Measurement of condensed-phase reaction kinetics in the aerosol phase using single particle mass spectrometry." *Journal of Physical Chemistry A*, 106: pp. 11083–11092, 2002.

[17] Ma, X. and Zachariah, M. R. "Size-resolved kinetics of Zn nanocrystal hydrolysis for hydrogen generation." *Internation Journal of Hydrogen Energy*, 35: pp. 2268–2277, 2010.

[18] Clarke, J. and Fray, D. "Oxidation of zinc vapour by hydrogen-water vapour mixtures." *Transactions of the Institution for Mining and Metallurgy C*, 88: pp. C161–C166, 1979.

[19] Weiss, R. J., Ly, H. C., Wegner, K., Pratsinis, S. E., and Steinfeld, A. "H_2 production by Zn hydrolysis in a hot-wall aerosol reactor." *American Institue of Chemical Engineering: Particle Technology and Fluidization*, 51: pp. 1966–1970, 2005.

[20] Wegner, K., Ly, H. C., Weiss, R. J., Pratsinis, S. E., and Steinfeld, A. "In situ formation and hydrolysis of Zn nanoparticles for H_2 production by the 2-step ZnO/Zn water-splitting thermochemical cycle." *International Journal of Hydrogen Energy*, 31: pp. 55–61, 2006.

[21] Ernst, F. O., Tricoli, A., Pratsinis, S. E., and Steinfeld, A. "Co-synthesis of H_2 and ZnO by in-situ Zn aerosol formation and hydrolysis." *American Institute of Chemical Engineering*, 52: pp. 3297–3303, 2006.

[22] Melchior, T., Piatkowski, N., and A. Steinfeld, A. "H_2 production by steam-quenching of Zn vapor in a hot-wall aerosol flow reactor." *Chemical Engineering Science*, 64: pp. 1095–1101, 2009.

[23] Abu Hamed, T., Davidson, J. H., and Haltiwanger, J. F. "Hydrogen production via hydrolysis of zinc nanoparticles." In "Proceedings of the American Institute of Chemical Engineers Conference," 2007.

[24] Funke, H. H., Diaz, H., Liang, X., Carney, C. S., Weimer, A. W., and Li, P. "Hydrogen generation by hydrolysis of zinc power aerosol." *International Journal of Hydrogen Energy*, 33: pp. 1127–1134, 2008.

[25] Abu Hamed, T., Venstrom, L., Alshare, A., Brulhart, M., and Davidson, J. H. "Study of a quench device for synthesis and hydrolysis of Zn nanoparticles: modeling and experiments." *Journal of Solar Energy Engineering*, 131: pp. 031018–1–9, 2009.

[26] Ma, X. and Zachariah, M. R. "Oxidation Anisotropy and Size-Depended Reaction Kinetics of Zinc Nanocrystals." *Journal of Physical Chemistry C*, 113: pp. 14644–14650, 2009.

[27] Turker, M. "Effect of production parameters on the structure and morphology of Ag nanopowders produced by inert gas condensation." *Materials Science and Engineering A*, 367: pp. 74–81, 2004.

[28] Girshick, S. and Chiu, C. "Homogeneous Nucleation of Particles from the Vapor Phase in Thermal Plasma Snythesis." *Plasma Chemistry and Plasma Processing*, 9: pp. 355–369, 1989.

[29] Granqvust, C. and Buhrman, R. "Ultrafine metal particles." *Journal of Applied Physics*, 47: pp. 220–2219, 1976.

[30] Panda, S. and Pratsinis, S. E. "Modeling the synthesis of aluminum particles by evaporation-condesation in an aerosol flow reactor." *Nanostructured Materials*, 5: pp. 755–767, 1995.

[31] Pratsinis, S. "Simultaneous nucleation, condensation, and coagulation in aerosol reactors." *Journal of Colloid and Interface Science*, 124: pp. 416–427, 1988.

[32] Pratsinis, S. E. and Vemury, S. "Particle formation in gases: a review." *Powder Technology*, 88: pp. 267–273, 1996.

[33] Joshi, S. V., Liang, Q., Park, J. Y., and Batdorf, J. A. "Effect of quenchinig conditions on particle formation and growth in thermal plasma synthesis of fine powders." *Plasma Chemistry and Plasma Processing*, 10: pp. 339–358, 1990.

[34] Suryanarayana, C. and Prabhu, B. *Nanostructured Materials: Processing, Properties, and Applications*, chapter Synthesis of nanostructured materials by inert-gas condensation methods, pp. 47–90. William Andrew Publishing, 2007.

[35] Mahoney, W. and Andres, R. "Aerosol synthesis of nanoscale clusters using atmospheric arc evaporation." *Materials Science and Engineering*, A204: pp. 160–164, 1995.

[36] Backman, U., Jokiniemi, J., Auvinen, A., and Lehtinen, K. "The Effecf of Boundary Conditions on Gas-Phase Sythesised Silver Nanoparticles." *Journal of Nanoparticle Research*, 4: pp. 325–335, 2002.

[37] Backman, U. *Studies on nanoparticle synthesis via gas-to-particle conversion.* Ph.D. thesis, University of Helsinki, 2005.

[38] Tsantilis, S. and Pratsinis, S. E. "Soft- and hard-agglomerate aerosols made at high temperatures." *Langmuir*, 20: pp. 5933–5939, 2004.

[39] Wada, N. "Preparation of fine metal particles by means of evaporation in helium gas." *Japanese Journal of Applied Physics*, 6: pp. 553–556, 1967.

[40] Tsantilis, S. and Pratsinis, S. E. "Evolution of primary and aggregate particle-size distributions by coagulation and sintering." *Materials, Interfaces, and Electrochemical Phenomena*, 42: pp. 407–415, 2000.

[41] Ernst, F. O. *Co-synthesis of H_2 and nanocrystalline ZnO particles by Zn aerosol formation and In-situ hydrolysis.* Ph.D. thesis, ETH Zurich (Diss. No. 17272), 2007.

[42] Tsantilis, S., Pratsinis, S., and Haas, V. "Simulation of synthesis of palladium nanoparticles in a jet aerosol flow condenser." *Journal of Aerosol Science*, 30: pp. 785–803, 1999.

[43] Warren, D. and Seinfeld, J. "Nucleation and growth of aerosol from a continuously reinforced vapor." *Aerosol Science and Technology*, 3: pp. 135–153, 1984.

[44] Haltiwanger, J. F., Venstrom, L., and Davidson, J. H. "Hydrolysis of Zn Particles in the temperature range 360 to 465K." In "Proceedings of ES2009, Energy Sustainability 2009," 2009.

[45] Abu Hamed, T., Davidson, J. H., and Stolzenburg, M. "Hydrolysis of evaporated Zn in a hot wall flow reactor." *Journal of Solar Energy Engineering*, 130: pp. 0410101–0410107, 2008.

[46] McQuarrie, D. A. and Simon, J. D. *Physical Chemistry: A Molecular Approach.* University Science Books, 1997.

[47] Roine, A. "Outokumpu HSC Chemistry for Windows; Outokumpi Resarch." Pori, Finland, 1997.

[48] Ramsey, J. W. and Goldstein, R. J. "Interaction of a heated jet with a deflecting stream." *Journal of Heat Transfer*, pp. 365–372, 1971.

[49] Crabb, D., Durao, D. F. G., and Whitelaw, J. H. "A round jet normal to a crossflow." *Journal of Fluids Engineering*, 103: pp. 142–153, 1981.

[50] Andreopoulos, J. "Measurments in a jet-pipe flow issuing perpendicularly into a cross stream." *Journal of Fluids Engineering*, 104: pp. 493–499, 1982.

[51] Andreopoulos, J. and Rodi, W. "Experimental investigation of jets in a crossflow." *Journal of Fluid Mechanics*, 138: pp. 93–127, 1984.

[52] Fric, T. F. and Roshko, A. "Vortical structure in the wake of a transverse jet." *Journal of Fluid Mechanics*, 279: pp. 1–47, 1994.

[53] Margason, R. J. "Fifty years of jet in cross flow research." In "AGARD Symposium on a jet in cross flow, Winchester, UK, AGARD CP-534," 1993.

[54] Yuan, L. L. and Street, R. L. "Trajectory and entrainment of a round jet in crossflow." *Physics of Fluids*, 10: pp. 2323–2335, 1998.

[55] He, G., Guo, Y., and Hsu, A. "The effect of Schmidt number on turbulent scalar mixing in a jet-in-crossflow." *International Journal of Heat and Mass Transfer*, 42: pp. 3727–3738, 1999.

[56] Muppidi, S. and Mahesh, K. "Study of trajectories of jets in corssflow using direct numerical simulations." *Journal of Fluid Mechanics*, 530: pp. 81–100, 2005.

[57] Camussi, R., Guj, G., and Stella, A. "Experimental study of a jet in a crossflow at very low Reynolds number." *Journal of Fluid Mechanics*, 454: pp. 113–144, 2002.

[58] Kelso, M., Lim, T. T., and Perry, A. E. "An experimental study of round jets in cross-flow." *Journal of Fluid Mechanics*, 306: pp. 111–144, 1996.

[59] Magnusson, M., Deppert, K., Malm, J., Bovin, J., and Samuelson, L. "Gold nanoparticles: Production, reshaping, and thermal charging." *Journal of Nanoparticle Research*, 1: pp. 234–251, 1999.

[60] "ANSYS FLUENT 13.0 Users Manual.", 2010.

[61] Schlichting, K., H.; Gersten. *Boundary -Layer Theory.* Springer, 7th edition, 1979.

[62] McMurry, P. H. "A review of atmospheric aerosol measurements." *Atmospheric Environment*, 34: pp. 1959–1999, 2000.

[63] Hinds, W. C. *Aerosol Technology: properties, behavior, and measurement of airborne particles, 2nd ed.* John Wiley & Sons, 1999.

[64] Jenkins, R. and Snyder, R. *Introduction to X-ray Powder Diffractometry.* John Wiley and Sons, Inc., 1996.

[65] Cussler, E. L. *Diffusion Mass Transfer in Fluid Systems.* Cambridge University Press, 2nd edition, 1997.

[66] Wang, Z. and Harris, R. "Morphology if Zinc Deposited from Mixed Gas Streams at Reduced Pressures." *Materials Characterization*, 30: pp. 155–173, 1993.

[67] Yan, Y., Liu, P., Romero, M. J., and Al-Jassim, M. M. "Formation of metallic zinc nanowires." *Journal of Applied Physics*, 93: pp. 4807–4809, 2003.

[68] Khan, A. and Kordesch, M. E. "Large-scale fabrication of metallic Zn nanowires by thermal evaporation." *Physica E*, 33: pp. 88–91, 2006.

[69] Pacala, S. and Socolow, R. "Stabilization Wedges: solving the climate problem for the next 50 years with current technologies." *Science*, 305: pp. 968–972, 2004.

[70] IPCC. *Climate Change 2007: The Physical Science Basis. Contribution of Working Group I to the Fourth Assessment Report of Intergovernmental Panel on Climate Change*, chapter Summary for Policymakers. Cambrige University Press, New York, 2007.

[71] *Carbon Tax Center*. www.carbontax.org.

[72] Rai, V., Victor, D. G., and Thurber, M. C. "Carbon Capture and Storage at Scale: Lessons from the Growth of Analogous Energy Technologies." Technical report, Staford University Program on Energy and Sustainable Development, 2009.

[73] *United States Energy Information Administration*. http://www.eia.doe.gov/.

[74] Darmstadter, J. *New Approaches for Energy and the Environment: Policy Advice for the President*, chapter Stimulating Renewable Energy, pp. 28–33. RFF, 2004.

[75] Charvin, P., Abanades, S., Lemort, F., and Flamant, G. "Analysis of solar chemical processes for hydrogen production from water splitting thermochemical cycles." *Energy Conversion and Management*, 49: pp. 1547–1556, 2008.

[76] Padro, C. and Putsche, V. "Survey of the Economics of Hydrogen Technologies." Technical report, NREL, 1999.

[77] Doty, F. D. "A Realisitic Look at Hydrogen Price Projections." Technical report, Doty Scientific, Inc., 2004.

[78] Spath, P. L. and Mann, M. K. "Life cycle assessment of hydrogen production via natural gas steam reforming." Technical report, National Renewable Energy Laboratory, 2001.

[79] IEA. "Experience Curves for Energy Technology Policy." Technical report, International Energy Agency and the Organization for Economic Co-operation and Development, 2000.

[80] Schoots, K., Ferioli, F., Kramer, G., and van der Zwaan, B. "Learning curves for hydrogen production technology: An assessment of observed cost reductions." *International Journal of Hydrogen Energy*, 33: pp. 2630–2645, 2008.

[81] Rubin, E. S., Yeh, S., Antes, M., Berkenpas, M., and Davison, J. "Use of experience curves to estimate the future cost of power plants with CO_2 capture." *International Journal of Greenhouse Gas Control*, 1: pp. 188–197, 2007.

[82] Neij, L. "Cost development of future technologies for power generation–A study based on experience curves and complementary bottom-up assessments." *Energy Policy*, 36: pp. 2200–2211, 2008.

[83] Romero, M., Buck, R., and Pacheco, J. E. "An update on solar central receiver systems, projects, and technologies." *Journal of Solar Energy Engineering*, 124: pp. 98–108, 2002.

[84] Levenspiel, O. *Chemical Reaction Engineering*. John Wiley & Sons, 1999.

[85] Mehta, R. D. and Bradshaw, P. "Design rules for small low speed wind tunnels." *The Aeronautical Journal of the Royal Aeronautical Society*, 83: pp. 443–449, 1979.

[86] Farell, C. and Xia, L. "A note on the design of screen-filled wide-angle diffusers." *Journal of Wind Engineering and Industrial Aerodynamics*, 33: pp. 479–486, 1990.

Appendix A

Comparison of Kinetic Models

This section outlines the way the diffusion limited reaction and surface reaction described in Ernst et al. [13] were compared to the reaction model described in Funke et al. [24].

Ernst et al. Diffusion Limited Regime Because the rate constants calculated by Ernst are based on the shrinking core model, that model can be used to calculate the amount of time required for full conversion, t_{full}. In the shrinking core model,

$$t_{full} = \frac{\bar{\rho}_{Zn} a^2}{6 b D_e C_{Zn}}, \tag{A.1}$$

where a is the particle radius, D_e is the diffusion coefficient (for the Zn diffusion through the ZnO shell), $\bar{\rho}_{Zn}$, the molar density of Zn, is equal to C_{Zn}, the concentration of Zn, and b, the stoichiometic coefficient, is 1 for this process [84]. The diffusion coefficient, D_E, is related to the reaction rate, r_d, as [13]

$$D_E = \frac{r_d}{2} \frac{\bar{\rho}_{ZnO}}{\bar{\rho}_{Zn}} \frac{M_{Zn}}{M_{ZnO}}, \tag{A.2}$$

where M is the molar mass. The time required for anything less than full conversion can be calculated for the shrinking core model using [84]

$$t = t_{full} \left[1 - 3(1-\alpha)^{2/3} + 2(1-\alpha) \right]. \tag{A.3}$$

Ernst et al. Surface Reaction Regime The surface reaction measured by Ernst et al. [13] occurs until the ZnO layer formed on the surface reaches a critical thickness and

the reaction becomes diffusion limited. However, for the sake of comparing the surface reaction kinetics to the others that will be presented here, a model that is limited only by the chemical reaction rate is assumed in order to calculate the time for different conversions. In this model, the reaction proceeds from the surface of the particle through the core, so the time rate of change of the radius where the reaction is occurring, a_c, is

$$-\frac{da_c}{dt'} = \frac{r_s}{\rho}. \tag{A.4}$$

Thus,

$$t = \frac{\bar{\rho}_{Zn}}{k_s y_{H_2O}^{0.5}}(a - a_{core}), \tag{A.5}$$

where a is the radius of the particle. In this model, the reaction proceeds from the outside of the particle in, so the conversion, α, is related to a_{core} by

$$\alpha = \frac{a^3 - a_{core}^3}{a^3}. \tag{A.6}$$

Funke et al. Funke et al. [24] used traditional, non-isothermal TGA to determine the kinetic parameters for the hydrolysis of Zn nanoparticles ($d_{avg} = 158nm$). They conducted all experiments at $y_{H_2O} = 1.8\%$. They fit their TGA data to where α is the fractional conversion and $f(\alpha)$ is an empirical depletion term. The function that best fits the TGA data is $f(a) = (1-\alpha)^{1.73}$, and

$$\frac{d\alpha}{dt} = A_o e^{-E_A/RT} \cdot f(\alpha), \tag{A.7}$$

which can be used to predict the time required for different degrees of conversion by integrating Eq. A.7:

$$t = \frac{1}{k(1.73-1)}\left[(1-\alpha)^{(1-1.73)})\right]. \tag{A.8}$$

Comparison Equations A.6, A.3 and A.8 can be used to compare the reaction rates predicted by Ernst and Funke et al., provided that particle diameter is assumed to be $\sim 158nm$. Because the kinetic expression provided by Funke et al. has no physical meaning, the expression cannot be extended to particle sizes other than those analyzed. In addition, because Funke et al. do not explore the effect of the molar concentration of steam, their rather

low value of $y_{H_2O} = 1.8\%$ must be assumed for the surface reaction regime in calculations using the kinetic expressions from Ernst et al. [13].

Appendix B

Diffuser Design

B.1 Introduction

The reactor is designed with a relatively large diameter ($75.7\,mm$) to allow for residence times sufficient for significant conversion to ZnO and to enable the use of sampling probes of up to $25\,mm$ diameter within the reactor. Thus, the design must include a diffuser to ensure that the quenching gas fills that entire diameter (as opposed to entering the reactor as a slowly spreading jet). A conical diffuser with an expansion angle sufficiently small to avoid separation of the flow was considered, but the length required (as much as $0.5\,m$) made that design impractical. Instead, a screen-filled wide angle diffuser is used to achieve the desired flow field. Screens are used to create a pressure drop that forces the flow towards the wall, thereby providing a more uniform velocity profile at the exit of the diffuser section. Having a characterized velocity profile, especially a uniform velocity profile, at the exit of the diffuser would allow for more accurate modeling of the flow field in the reactor, especially because the trajectory of the jet is known to depend of the velocity profile of the cross-flow [56].

Information about designing screen filled wide angle diffusers is found in the literature on the design of wind tunnels [85, 86]. The literature provides design guidelines and rules of thumb based on extensive empirical data. The four most important parameters in the design of wide angle diffusers are the diffuser expansion angle, 2θ, the ratio between the

inlet and outlet areas, $\frac{A_{out}}{A_{in}}$, the pressure drop coefficient across the screens, K, and the number of screens, n. Wide angle diffusers are recommended for situations with $2\theta \leq 50°$ and $\frac{A_{out}}{A_{in}} \leq 5$. Initial design guidelines provided in the literature include :

- Use screens with the open area fractions, β, of more than 0.6, as instabilities in the flow can result from small open area fractions.
- For a given β, a finer mesh with smaller diameter wires is desirable because it better reduces variation in the flow, especially due to turbulence.
- A pressure drop coefficient, K, of about 2 across a screen is generally sufficient to remove variations in the longitudinal velocity and create a nearly uniform velocity profile.
- The area ratio between successive screens, $\frac{A_{i+1}}{A_i}$, should be constant and about 1.4 or less. A decreased successive area ratio results in more screens in a given diffuser, so the pressure drop across each screen can be less. For an area ratio of 1.4, a screen with $\beta \approx 0.7$ is reasonable.
- The approximate number of screens can be determined using

$$1.4^{n-1} = \frac{A_{out}}{A_{in}}. \tag{B.1}$$

The key to the design of these diffusers is the pressure drop across the screens. Based on the collection of over 100 wide angle diffuser designs, Mehta and Bradshaw [85] found a relationship between the overall area ratio ($\frac{A_{out}}{A_{in}}$) and required value of the sum of the pressure drop coefficients across all of the diffuser screens, $\sum_{i=1}^{n} K_i$:

$$\sum_{i=1}^{n} K_i \geq \frac{A_{out}/A_{in}-1}{1.14}. \tag{B.2}$$

Thus, the ability of a screen filled diffuser to avoid separation can be predicted for a given geometry if the pressure drop coefficients are known. The pressure drop coefficient is equal to the pressure drop across the screen divided by the dynamic pressure of the approaching

gas. Though there is not a completely satisfactory way to predict K_i, Wieghardt's 1953 formula is generally acceptable for $Re_{d.screen} \leq 600$ [85]. Wieghardt's formula is:

$$K = 6.5 Re_d^{-1/3} \frac{1-\beta}{\beta^2} \tag{B.3}$$

In this expression, the Reynolds number is given by:

$$Re_d = \frac{u d_{wire} \rho}{\beta \mu} \tag{B.4}$$

where u is the approach velocity, and d_{wire} is the diameter of the mesh wire. Comparing the sum of the pressure drops calculated using equations B.3 and B.4 to the minimum needed to avoid separation (equation B.2) allows for more detailed design.

B.2 Analysis

Equations B.3 and B.4 are used to calculate K_i for the range of likely operating conditions and for a variety of different screen options. Three potential meshes were identified, with $\beta = 0.65$, 0.7, and 0.73. Each of these mesh options was evaluated for all six combinations of $T = 353\,K$, $373\,K$, and $473\,K$ and Ar flow rates of $10^{L}/_{min}$ and $20^{L}/_{min}$. To minimize the overall area ratio, an inlet pipe with an outer diameter of $25.4\,mm$ and an inner diameter of $23.6\,mm$ was used. This results in $\frac{A_{out}}{A_{in}} = 10.3$, which is larger than recommended for this type of diffuser. Comparison of the sum of calculated K_i to the minimum required value and modeling of the flow field using the computational fluid dynamics software, FLUENT, are both used to ensure that separation is avoided despite the larger overall area ratio. By equation B.2, $\sum_{i=1}^{n} K_i \geq 8.1$ should avoid separation.

For $\frac{A_{out}}{A_{in}} = 10.3$, equation B.1 predicts that the number of screens, n, must be eight for the successive area ratio to be no more than 1.4. Thus, for each of the three potential meshes, K_i is calculated using equations B.3 and B.4 for each of the eight screens under each of the six temperature and flow rate combinations. The sum of these pressure drop coefficients is compared to the minimum required value (8.1) to determine if avoidance of separation is predicted. When sum of the pressure drop coefficients is significantly higher than 8.1, we explore designs with fewer screens, and thus a larger successive area ratio.

To complete the design process, the selected geometry was modeled using in FLUENT using the 2D equations for the conservation of mass, momentum, and energy. Two-dimensional modeling is sufficient, as the geometry is axi-symmetric. I modeled the flow of a mixture of Ar and H_2O with $y_{H_2O} = 0.3$ for $373\,K$ and $473\,K$ and Ar flow rates at the mass flow controller of $10^{L}/_{min}$ and $20^{L}/_{min}$. The walls were assumed to be the same temperature as the inlet gas. The screens were modeled using the porous jump model, which allows for modeling a thin porous media (like a screen) on a 2D face in the 3D model or a 1D edge in the 2D model. Because the diffuser is axi-symmetric, the 2D model was more efficient. This porous jump formulation is considered more robust than the porous zone model, and is highly recommended for porous media such as screens and filters. In the porous-jump model, the pressure drop is calculated form the Darcy equation with the Forchheimer extension. The model requires a permeability, thickness, and coefficient for the Forchheimer term for each screen. At the low velocities in this diffuser, the Forchheimer term can be neglected. Permeability was calculated from the pressure drop coefficients (from equation B.3) and Darcy's equation.

B.3 Results

The calculations of the pressure drop coefficients and comparisons with the minimum required sum of them indicated that using eight screens made out of all three meshes was more than sufficient to avoid separation. Because higher open area fractions are considered desirable in the literature, the mesh with $\beta = 0.65$ was eliminated. The mesh with $\beta = 0.7$ provided more then enough total pressure drop to avoid separation with as few as five meshes and the mesh with $\beta = 0.73$ successfully avoided separation with as few as six total meshes, as can be seen in Table B.1. The mesh with $\beta = 0.7$ had the added benefit of being made from finer wires, which is also considered desirable, and it was readily available commercially in the small quantity needed. Thus, the mesh with $\beta = 0.7$ is used in the diffuser. In order to gain confidence that the flow will not separate, a conservative approach to the design was taken, and the number of screens used is six rather than five. The radii and axial location

Table B.1: Sum of pressure drop coefficients for $\beta = 0.7$ with 8, 6, and 5 screens and for $\beta = 0.73$ with 8 and 7 screens.

	$\beta = 0.7$	$\beta = 0.73$
8	17.0 to 23.1	13.2 to 18.0
7	14.9 to 20.2	11.4 to 15.6
6	12.0 to 16.4	9.8 to 13.3
5	9.9 to 13.5	–

Table B.2: Radii, axial locations, and length between each screen for the six screens in the diffuser.

screen number	radius [mm]	axial location [mm]	length between [mm]
1	11.6	0	–
2	14.9	11.6	11.6
3	18.8	26.2	14.6
4	23.8	44.6	18.4
5	30.0	67.8	23.3
6	37.8	97.2	29.4

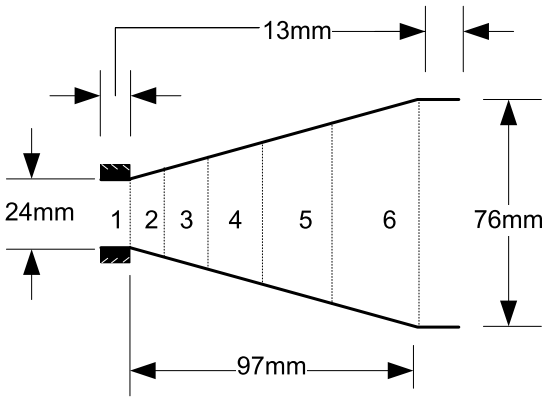

Figure B.1: Schematic of the designed screen filled wide angle diffuser.

of the six screens are listed in Table B.2, and Figure B.1 is a schematic of the diffuser with screens.

The results of the model predict a relatively uniform velocity profile, as can be seen in Figure B.2. In addition, the diffuser is modeled with an extra screen $25.4\,mm$ from the exit

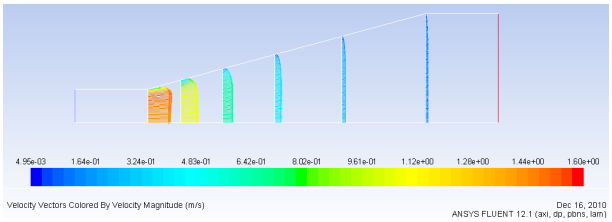

(a)

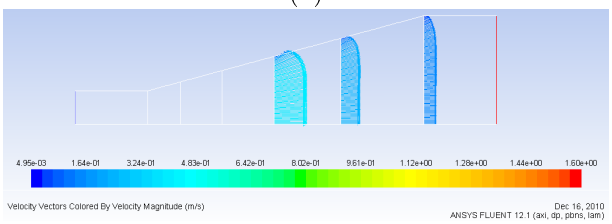

(b)

Figure B.2: Vectors of velocity magnitude for (a) all six screens and (b) the last three screens (lengths multiplied by 5 for better visibility, for $T = 373K$ and Ar flow rate of $20^{L}/_{min}$.

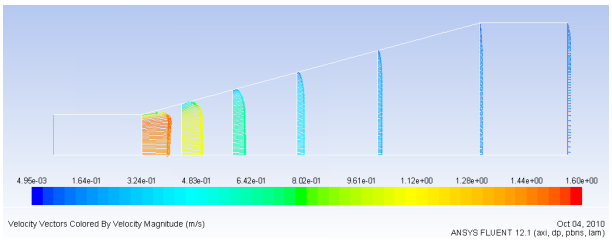

(a)

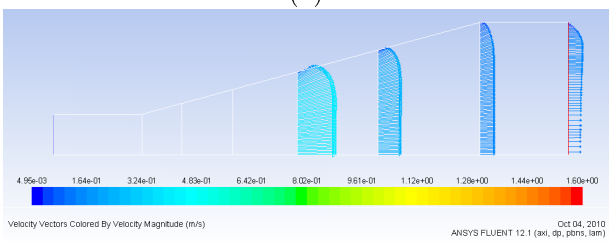

(b)

Figure B.3: Vectors of velocity magnitude for the outlet and (a) all seven screens and (b) the last four screens (lengths multiplied by 5 for better visibility, for $T = 373K$ and Ar flow rate of $20^{L}/_{min}$ and the geometry with the additional screen $1\,cm$ after the end of the diffuser.

of the diffuser to further reduce variations in the velocity profile, as seen in Figure B.3. The velocity profile after that extra screen is extremely uniform, with a small boundary layer of less than 10% of the radius. Figure B.4 shows the velocity profiles at the exit of the last screen in the diffuser for the range of operating conditions. In all cases, separation is avoided

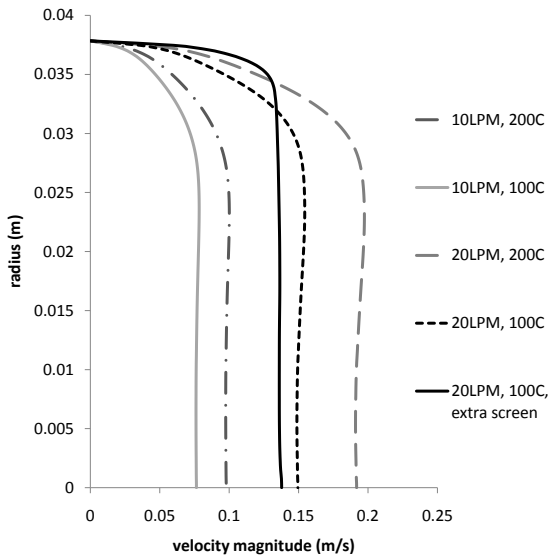

Figure B.4: Velocity profiles at the exit of the last screen of the diffuser for the likely range of operating conditions.

and the velocity profile is nearly uniform.

Appendix C

Evaporation Rate Measurements

Jacob West, an undergraduate student participating in the Research Experience for Undergraduates (REU) program, spent his summer in the lab on a careful study of the evaporation rate of Zn in the experimental set-up used in the present study as the evaporation zone. Flow rates through the evaporation tube were varied from $100\,mL/min$ to $1\,L/min$, and temperatures (measured next to the crucible, as in the present study) were recorded with a Type-K thermocouple and varied from $773\,K$ to $1173\,K$. He observed no significant dependence on the flow rate of Ar over the crucible below $1100\,K$. The scatter in data at $1173\,K$ is primarily attributed to the difficulty in achieving the measurements; at this high temperature, Zn evaporated so quickly that the amount of Zn initially in the crucible had a strong effect on the measured average evaporation rate. Jacob's data is shown in Figure C.1. He fit his data to the exponential curve

$$\dot{m}_{Zn} = 1.694 \times 10^{-8} \exp(0.01261T) \tag{C.1}$$

which closely agrees with the data below $1100\,K$.

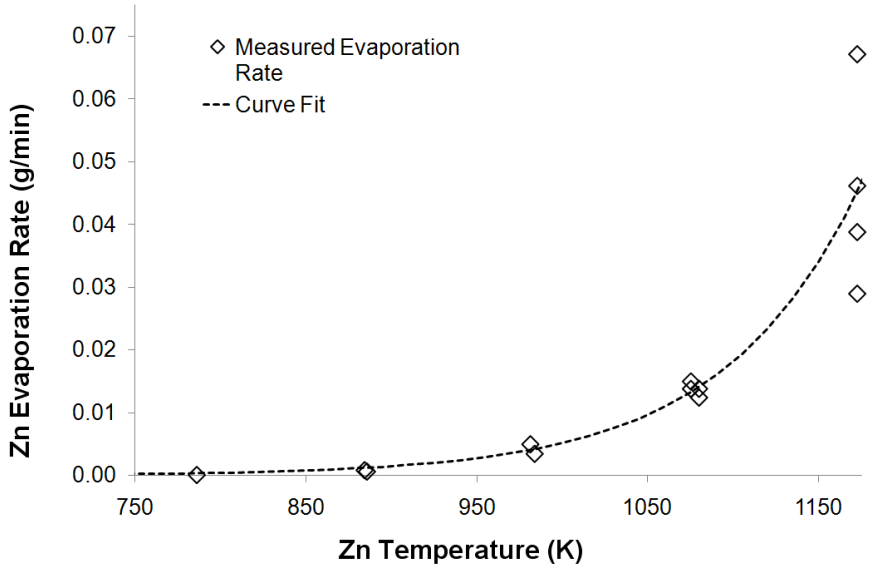

Figure C.1: Evaporation rate vs temperature

Appendix D

Probe Sampling Efficiency

The ejection dilution probe was tested using a known sample of NIST traceable particles with mean diameters of $30\,nm$ and $60\,nm$. A nebulizer was used to produce an aerosol with these particles, which was sampled with the ejection dilution probe and measured by the Scanning Mobility Particle Sizer (SMPS). The aerosol was also measured directly by the SMPS. In the nebulizer, water containing different amounts of the NIST traceable particles was subjected to a high pressure ($15psi$) flow of N_2, which entrained water droplets that contained the particles. The water was removed from the aerosol by flow through a desiccant dryer, producing the test aerosol. A particle distribution associated with either the nebulizer or the water dominated the measured distribution, with a peak diameter of $50\,nm$ and concentration of approximately $5 \times 10^4/cm^3$. Particle sizes ranged from10 to $200\,nm$. The addition of NIST particles resulted in predictable changes in the distribution, which were captured by the probe measurements, as well as the direct measurements by the SMPS.

A major potential mechanism for failure to sample larger particles is at the probe inlet. Small particles universally follow the gas streamline, but larger particles with more inertia don't respond as quickly to changes in the gas flow. The Stokes number can be used to characterize how well particles of various sizes follow gas streamlines in response to various obstacles or changes. It is defined as

$$Stk = \frac{\tau u_\circ}{L} \tag{D.1}$$

Table D.1: Transmission Efficiencies (%) in the Probe

d_p	η_{inlet}	η_{diff}	η_{bend}
$10\,nm$	99.97	74.7	100
$100\,nm$	99.8	98.4	99.7
$1\,\mu m$	98.5	99.8	87.6
$10\,\mu m$	74.4	99.96	0

where L is a characteristic length scale for the disturbance in the flow field, $u_\circ$ is the undisturbed gas velocity, and τ is the relaxation time

$$\tau = \frac{\rho_p d_p^2 C_c}{18\mu} \tag{D.2}$$

where C_c is the slip correction factor. When $Stk \ll 1$, particles follow the streamline perfectly [63]. For a reactor temperature of $713\,K$ and pressure of $1.07\,atm$ and reactor gas velocity approximately $0.1\,m/s$, Stk for the inlet of the sampling probe is less than 10^{-4} for particles up to $100\,nm$. $Stk = 10^{-3}$ for $1\,\mu m$ particles and 10^{-2} for $2\,\mu m$ particles, and ~ 0.1 for $10\,\mu m$ particles. Thus, particles as big as $1 - 2\,\mu m$ should generally follow the gas streamline into the probe.

The sampling efficiency at a probe inlet parallel to the gas flow can be calculated directly

$$\eta_{inlet} = 1 + \left(\frac{u_s}{u_p} - 1\right)\left(1 - \frac{1}{1 + (2 + 0.62^{u_s}/_{u_r})\mathrm{Stk}}\right) \tag{D.3}$$

where $u_s$is the velocity in the probe inlet, u_r is the velocity in the reactor [63]. The sampling efficiency at the inlet is listed in Table D.1 for a range of particle sizes, given $^{u_s}/_{u_p} = 0.0075$. Losses due to diffusion, η_{diff}, in $5\,m$ of hose from the probe to the SMPS are also listed, assuming $20\,L/min$ through the hose (with diameter $67\,mm$).

Loss in a bend is calculated for a 90° bend with a tube diameter of of $8\,mm$ as

$$\eta_{bend} = exp(-2.88 \cdot Stk \cdot \phi) \tag{D.4}$$

where ϕ is the bend angle and Stk is based on the tube diameter [63]. Thus, while the probe can efficiently sample particles up to $\sim 2\,\mu m$, particles bigger than $1\,\mu m$ will impact in elbows and bends downstream of the probe.

Appendix E

Quantitative Analysis with XRD

To obtain accurate measurements of ZnO at the low concentrations expected at the filter, we use the internal standard method [64] to calibrate the XRD using samples of known concentration. The calibration samples are prepared in our laboratory by packed bed conversion of Zn particles prepared in the transverse jet aerosol reactor. These particles are generated in the transverse jet reactor without steam and are collected from the filter after the reactor has cooled. An initial XRD peak measurement is taken to ensure that there is no ZnO peak prior to oxidation. The mass of the calibration samples are recorded and then a sample is loaded into a packed bed reactor. With $300\,sccm$ of Ar flowing over the sample, the reactor temperature is allowed to stabilize at $350°C$. At that point, the Ar flow is reduced to $150\,sccm$ and $150\,sccm$ of carbon dioxide, CO_2, is added to the flow. The molar concentration of CO in the effluent gas is measured at $1\,s$ intervals using the RLGA. Due to the stoichiometry of the reaction ($Zn + CO_2 \longrightarrow ZnO + CO$), the molar production of ZnO is equal to the molar production of CO. Thus, the total molar conversion to ZnO is determined using equations 4.2-4.4, for CO instead of H_2. CO_2 was used as the oxidizer in these experiments because we can obtain more accurate measurements of the flow rate of CO_2 than the flow rate of H_2O, and thus more accuracy in the conversion values. These calibration samples with known ZnO molar conversions were then analyzed via XRD (Bruker-AXS D5005 Diffractometer) with three scans. A long scan covering $25° \leq 2\theta \leq 90°$ to get the majority sample spectrum was obtained so that RIR analysis could be done for comparison.

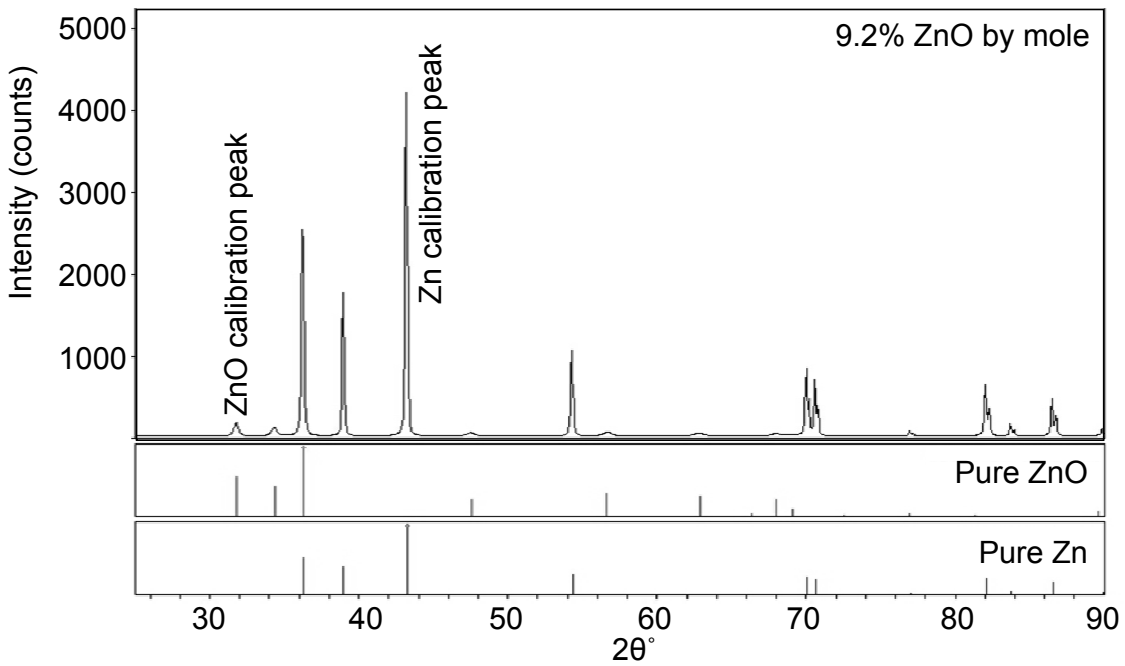

Figure E.1: XRD spectrum for the calibration sample that is 9% ZnO by mole, compared to the pure Zn and ZnO spectra.

The primary Zn peak ($2\theta = 43.3°$) and the second largest ZnO peak ($2\theta = 31.8°$) of the XRD spectrum (see Figure E.1) are used for the calibration because they are the largest peaks attributable solely to Zn and ZnO, respectively. The analysis is completed using long dwell times ($10\,s$) at each 2θ step to obtain high signal to noise ratios. This approach allows for clear detection of the ZnO peak even at very low concentrations ($> 1\%$). The calibration uses the ratio of the area under the ZnO peak to the area under the Zn peak. Peak area is chosen because it is relatively robust across most crystallite sizes. The Zn and ZnO peaks for the calibration sample with 9.2% ZnO and 0.74% ZnO are shown in Figures E.2 and E.3, respectively. The Zn and ZnO peaks for Experiment H are shown in Figure E.4.

The data and regression curve are shown inFigure E.5. The resulting calibration is

$$Z = 201.14\frac{A_{ZnO}}{A_{An}} - 1.09 \tag{E.1}$$

where Z is the molar conversion in percent and the uncertainty in Z is $\pm 0.58\%$ (absolute). A_{ZnO} and A_{Zn} are are the areas under the ZnO peak and Zn peak, respectively. The

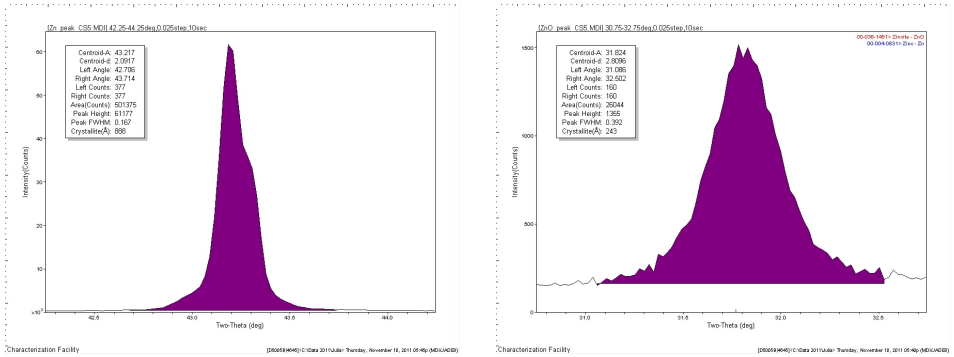

(a) (b)

Figure E.2: (a)Zn peak and (b)ZnO peak for a calibration sample with 9.2% ZnO.

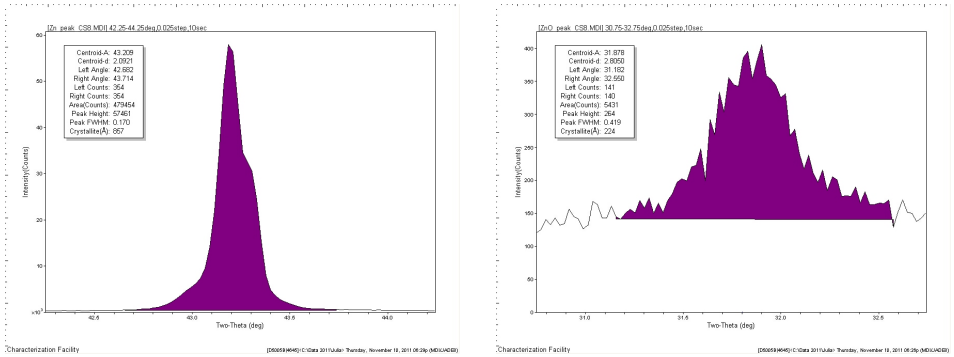

(a) (b)

Figure E.3: (a)Zn peak and (b)ZnO peak for a calibration sample with 0.74% ZnO.

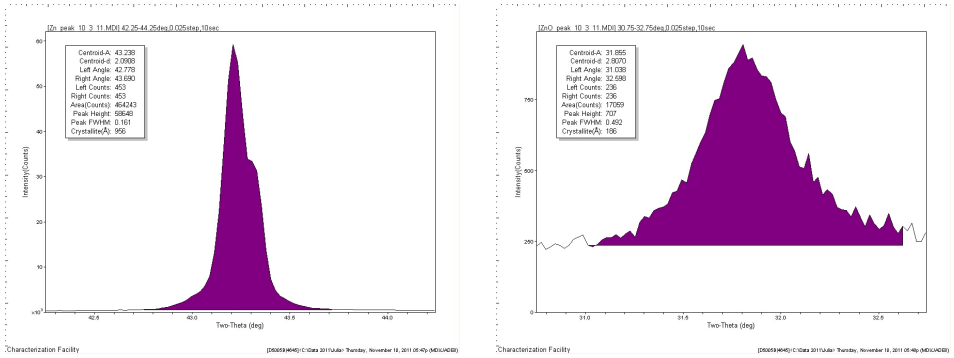

(a) (b)

Figure E.4: (a)Zn peak and (b)ZnO peak for particles from experiment H.

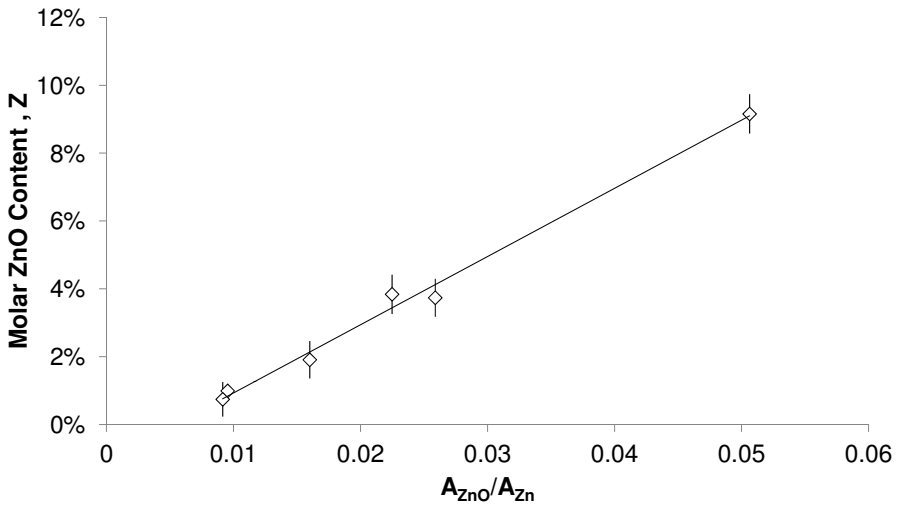

Figure E.5: Calibration curve for quantitative XRD analysis of ZnO molar composition.

calibration is for $0.5\% \leq Z \leq 10\%$. The internal standard method was chosen over the RIR and Rietveld methods because both of these more conventional peak-fitting methods over-predict the ZnO content of known samples. At the maximum level of refinement achieved using the Rietveld and RIR fitted patterns, the height and area of all peaks attributed exclusively to Zn are under-predicted. As evidence of this problem, RIR and Rietveld predict $30 - 50\%$ ZnO in a calibration sample that is 10% ZnO. Table E.1 lists the known sample concentrations, the molar concentration predicted by the calibration, the corresponding mass content of ZnO based on the calibration, the mass content predicted by the RIR peak fitting method, and the mass content predicted by an older calibration that relied on commercial Zn and ZnO powders that were not of the same size or morphology as the aerosol particles. RIR over-predicts the ZnO content of known samples by a factor of 2 to 5. Traditional peak fitting methods as a means to measure the ZnO content of Zn/ZnO particles should therefore be used with caution, or, better yet, not at all. In addition, a calibration based on particles made in the experimental reactor is superior to one relying on commercial powders. Table lists the ZnO content of filter particles in experiments D, F, H, and I (hydrolysis experiments with the goal of ZnO production) determined by the internal standard calibration (ZnO content by mole and mass) and by the RIR peak fitting method.

Table E.1: ZnO content by the calibration described in this study compared to ZnO measured by RIR and by an older calibration using mixtures of commercial particles.

sample #	Measured conversion to ZnO by moles	ZnO content by moles: Calibration	ZnO content by mass: Calibration	ZnO content by mass: RIR	ZnO content by mass: Older calibration [44]
1	0.74%	0.75%	0.93%	5.4%	0.52%
2	0.99%	0.83%	1.03%	13%	0.69%
3	1.91%	2.12%	2.64%	7.6%	0.83%
4	3.74%	4.12%	5.07%	14%	1.28%
5	3.84%	3.43%	4.24%	12.7%	1.12%
6	9.16%	9.09%	11.07%	22.1%	2.4%

Table E.2: ZnO content of filter particles in experiments D, F, H, and I (hydrolysis experiments with the goal of ZnO production) determined by the internal standard calibration (ZnO content by mole and mass) and by the RIR peak fitting method.

	T_{RZ}	T_{EZ}	y_{H_2O}	config.	ZnO content by moles: Calibration	ZnO content by mass: Calibration	ZnO content by mass: RIR
D	$573\,K$	$1000\,K$	0.12	B	1.5%	1.8%	8.4%
F	$603\,K$	$1000\,K$	0.12	B	2.2%	2.7%	8.8%
H	$723\,K$	$1000\,K$	0.12	A	6.3%	7.7%	18.2%
I	$723\,K$	$1000\,K$	0.12	B	6.8%	8.3%	17%

Appendix F

Residence Time Calculations

The average gas residence time, τ_{av}, is determined by integrating the average gas velocity in the reactor, $\bar{u}(x)$ over the length of the reactor.

$$\tau_{avg} = \int_0^L \frac{1}{\bar{u}(x)} dx \tag{F.1}$$

Because the temperature data is not continuous, the summation version of Equation F.1 must be used:

$$\tau_{avg} = \sum_{i=1}^{L} \frac{1}{\bar{u}(x)} \Delta x \tag{F.2}$$

The velocity is a function of the flow rate, q, which depends on temperature. Assuming ideal gas, the volumetric flow rate at location 1 with temperature T_1 can be compared to a volumetric flow rate at location 2 with temperature T_2as

$$q_2 = q_1 \frac{T_2}{T_1} \tag{F.3}$$

When the cross-sectional area is constant, as it is in the transverse jet reactor, the velocity at location 1, $\bar{u}_1$, can be related to the velocity at location 2, $\bar{u}_2$, similarly:

$$\bar{u}_2 = \bar{u}_1 \frac{T_2}{T_1} \tag{F.4}$$

Using this relationship, experimental temperature data at various x locations is combined with temperature and average velocity from the numerical model at the modeling domain

outlet, $\bar{u}_M$ and T_M, respectively:

$$\bar{u}(x) = \bar{u}_M \frac{T(x)}{T_M} \tag{F.5}$$

This method of estimating $\bar{u}(x)$ has the benefit of also being applicable to other information characterizing the velocity field. For example, the maximum velocity can be estimated from the maximum velocity modeled at the outlet, the velocity at the $75th$ percentile (by mass) can be estimated based on that from the model.

Appendix G

Impact Length and Other Deposition Patterns in the Transverse Jet Reactor

G.1 Impact Length

The measured impact length can also be compared to the numerical model through predicted Zn vapor concentrations on the top part of the tubular reactor wall. The molar fractions of Zn along the line at the top of the reactor (see the line labeled "Top Line" in Figure 5.3) are retrieved from the model to compare to impact lengths. For direct comparison, the molar fraction of Zn that corresponds to the onset of visible deposition would need to be known—it is not. However, as will be discussed later in this section, the total fraction of evaporated mass that is deposited on the upper part of the mixing zone wall is generally $< 1\%$ of the total evaporated mass. Zinc molar fractions of 10^{-6} approximately 0.1% of the maximum (jet centerline) Zn molar fraction. Thus, Table G.1 lists the modeled x location when Zn molar fractions reached 10^{-6} as a comparison to the measured impact length and the impact length predicted by the generalized scaling law. These lengths are similar to the measured l_i.

Table G.1: Measured, modeled, and scaling law impact lengths for experiments with varying R and y_{H_2O}, all in mm. No reported value (–) for the model data indicates that y_{ZnO} did not reach the indicated level before the end of the modeling domain.

	R	y_{H_2O}	Measured	Model reaches 10^{-6}	Scaling Law
1	12.15	0	-12 ± 12		6
2	6.38	0	43 ± 12.5		40
3	5.81	0.12	53 ± 17.5	63	53
4	4.91	0	115 ± 15		89
5	4.49	0	125 ± 15		118
6	4.50	0.11	125 ± 25	110	117
7	4.25	0	135 ± 15		139
8	4.24	0.12	135 ± 15	123	140
9	3.04	0.12	170 ± 15		388
10	3.04	0.12	none	–	388

G.2 Other Deposition Patterns

Deposition patterns on the evaporation tube liner, the mixing/reaction/collection zone liner, and the filter have several common elements across experiments 2 through 9. Some elements are present regardless of the steam concentration, while others change significantly with the presence of H_2O. In general, approximately 30% of the evaporated Zn re-condenses on the wall of the evaporation tube from $y = -6\,mm$ to $y = 0$. The tape heater at the tip of the evaporation zone (TH2) is used to reduce this condensation, and in fact without TH2, 50 to 60% of evaporated mass re-condenses. However, the uppermost $6\,mm$ of the evaporation tube liner coincides with the walls of the outer stainless steal reactor shell and the quartz reactor liner, where it is not possible to directly control the temperature.

The mixing zone has some of the most interesting deposition patterns in the reactor. Particle deposits begin just after the jet inlet on the bottom of the evaporation tube in a narrow ($\sim 10\,mm$ wide tail that extends between 20 and $120\,mm$ before it rapidly widens. The widening pattern strongly resembles a whale's tail—as the deposition pattern widens,

it breaks into two paths which swoop up the walls of the quartz liner in both directions. In experiments without steam, particle deposition is strongest just after the jet. At lower R experiments, the deposition right around the jet inlet is very significant. In experiments with steam, the region just after the jet inlet is covered in the white, cloudy depositions that are characteristic of the heterogeneous vapor-phase reaction between Zn and H_2O. The pattern can be explained by the development of the CRVP in in the tubular reactor—mass is drawn up from the bottom of the reactor by entrainment into the CRVP along the line that deposits are observed. The length before the "whale tail" depends on how far the jet penetrates into the mixing zone before being deflected into the stream-wise direction. In jets that penetrate farther into the mixing zone, that length is shorter, as the Zn mass is moving away from the bottom part of the reactor at an earlier x location.

The initial depositions are very light—they darken and become wider with increasing axial distance. Eventually (by $180 - 240\,mm$) these depositions spread to cover the top half of the quartz tube liner. Then, throughout the reaction zone and cooling zone, the particle depositions slowly become lighter. Regardless of the "darkness" of the deposition, the amount of mass in the first $0.15\,m$ of the reaction zone is always less than 3% of the total evaporated mass, and often less than 1% . The measured mass in the particle collection zone is always $< 1\%$.

Appendix H

Thermophoretic Calculations

The thermophoretic velocity, u_{th}, for particles with $d_p \gg \lambda$ is [63]

$$u_{th} = \frac{-3\mu C_c H \nabla T}{2\rho_g T_p} \tag{H.1}$$

where k_g and k_p are the thermal conductivities of the gas and particle, respectively, C_c is the slip correction factor, μ is the viscosity of the gas, ρ_g is the density of the gas, ∇T is the thermal gradient, T_p is the temperature of the particle, and H is

$$H \cong \left(\frac{1}{1+6\lambda/d_p}\right) lambda \left(\frac{k_a/k_p + 4.4\lambda/d_p}{1+2k_a/k_p + 8.8\lambda/d_p}\right) \tag{H.2}$$

In experiments A and B, temperatures in the reaction zone are slightly cooler than those in the mixing zone, and wall temperatures are held as constant as possible along the heated length of the reactor (mixing and reaction zones). In contrast, the reaction zone is heated above the mixing zone temperatures in experiments C through I. The walls in these experiments are thus hotter than the entering gas, creating a temperature gradient in the reactor. Assuming a temperature gradient of $20\,K/mm$ near the wall, u_{th} is $0.18\,mm/s$ away from the wall for a $500\,nm$. Thus, particles have a slight velocity away from the wall until near the start of the cooling zone, when the wall begins to cool. At that point, the walls are cooler than the gas. Given a temperature gradient of $30\,K/mm$ near the wall, $u_{th} = 0.36\,mm/s$ towards the wall. In this section, thermophoresis results in the observed increased deposits in the cooling zone.

Appendix I

Additional SEM Images

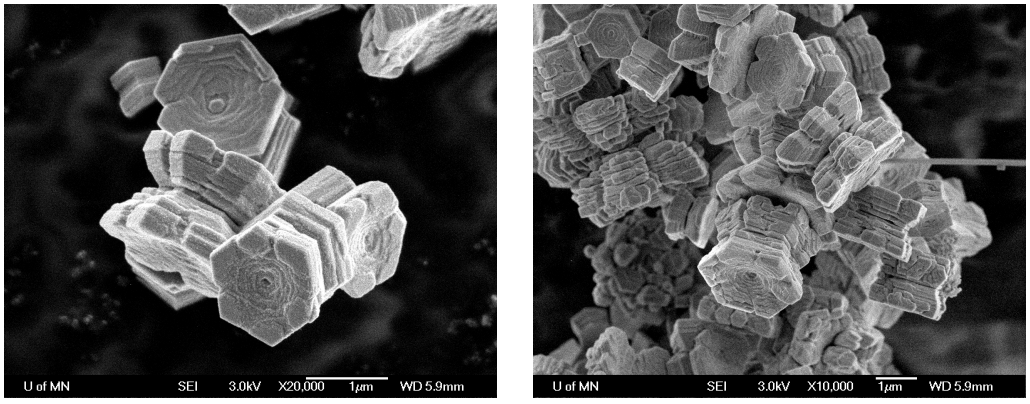

Figure I.1: Additional SEM images from Experiment A ($T_{sat} = 418\,K$ and $y_{H_2O} = 0$).

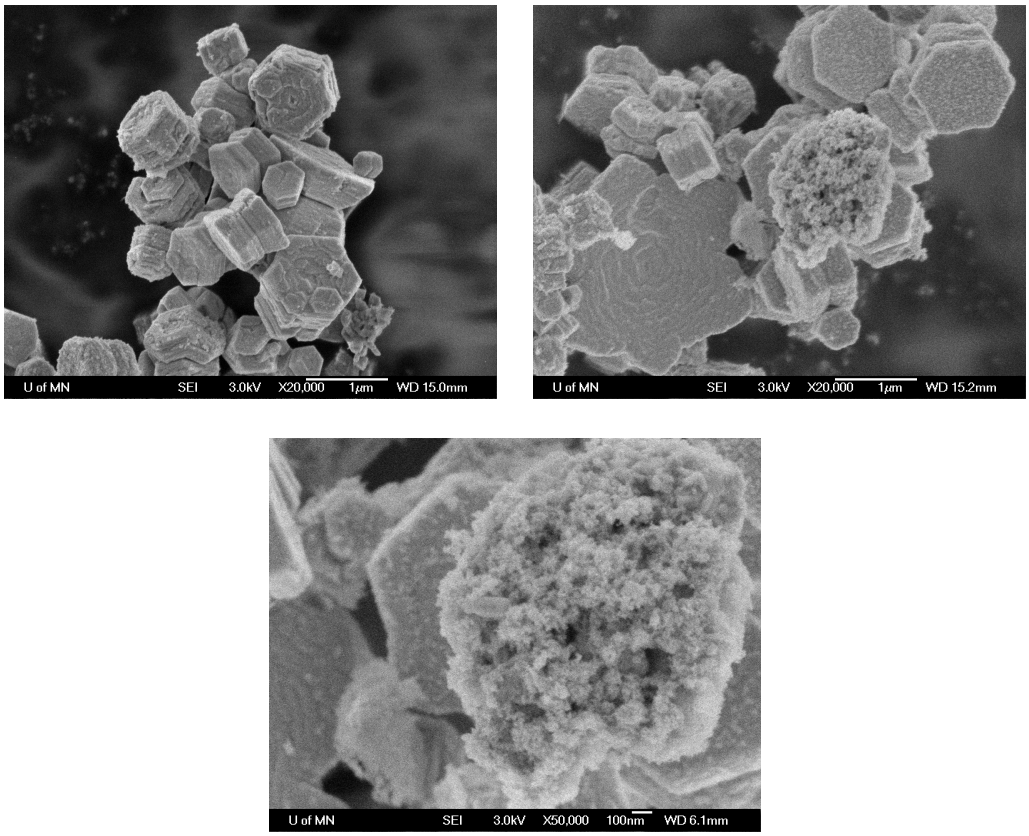

Figure I.2: Additional SEM images from Experiment B ($T_{sat} = 418\,K$ and $y_{H_2O} = 0.12$).

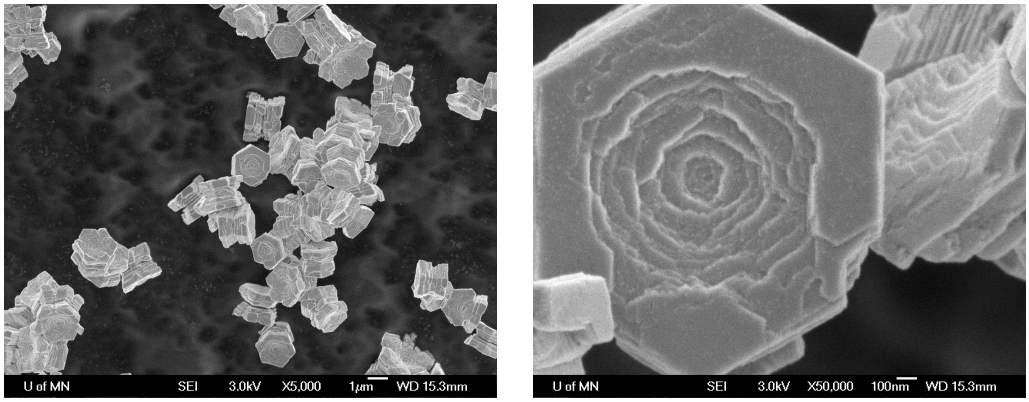

Figure I.3: Additional SEM image from Experiment C ($T_{sat} = 573\,K$ and $y_{H_2O} = 0$).

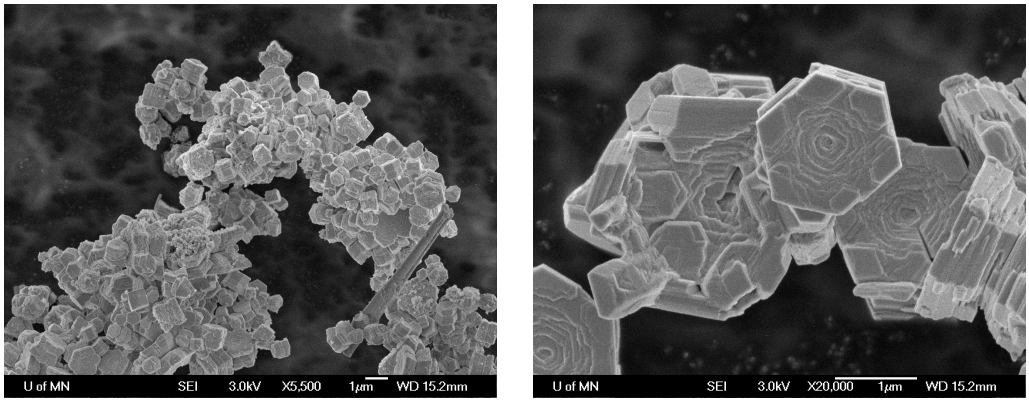

Figure I.4: Additional SEM images from Experiment D ($T_{sat} = 573\,K$ and $y_{H_2O} = 0.12$).

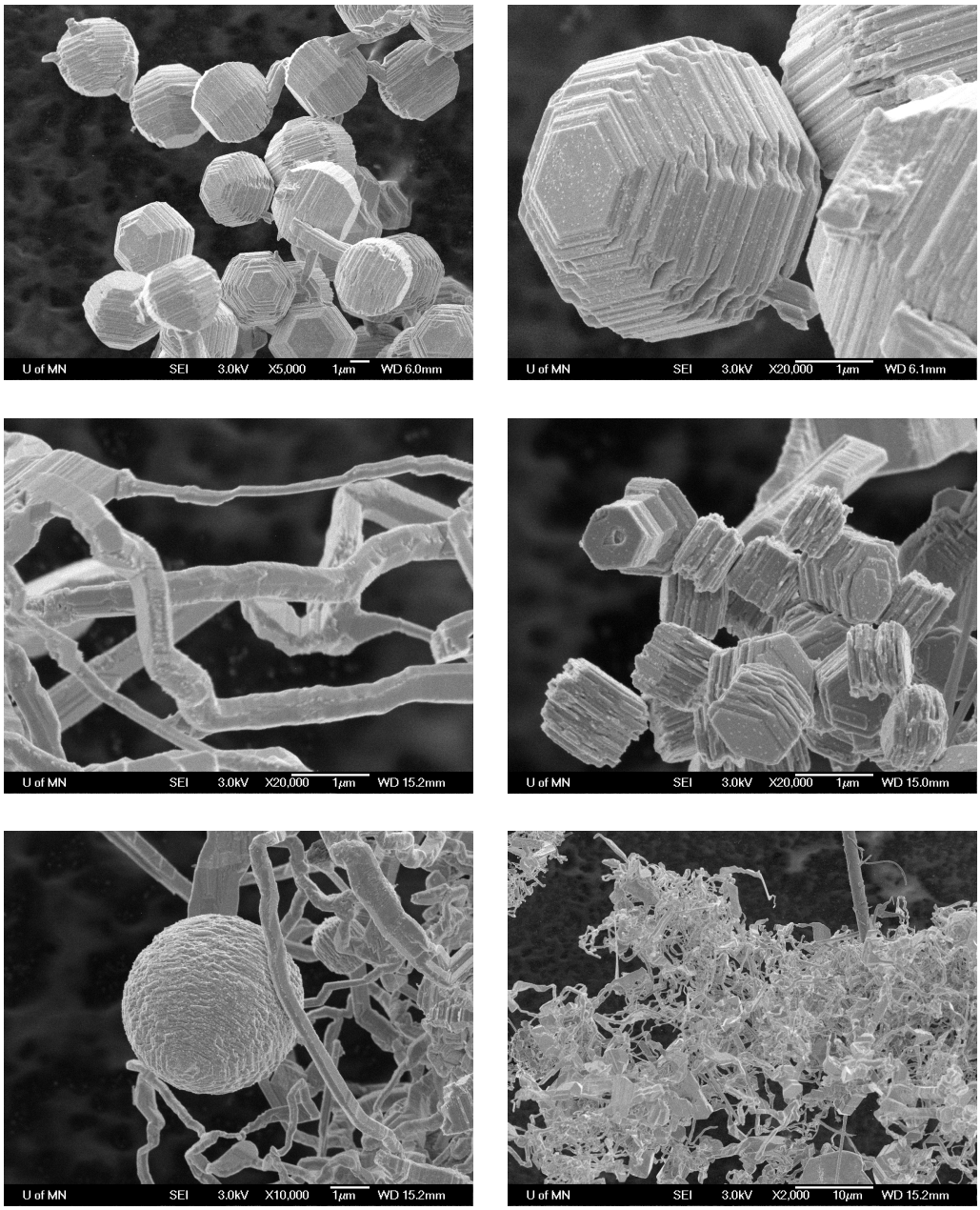

Figure I.5: Additional SEM images from Experiment G ($T_{sat} = 713\,K$ and $y_{H_2O} = 0$).

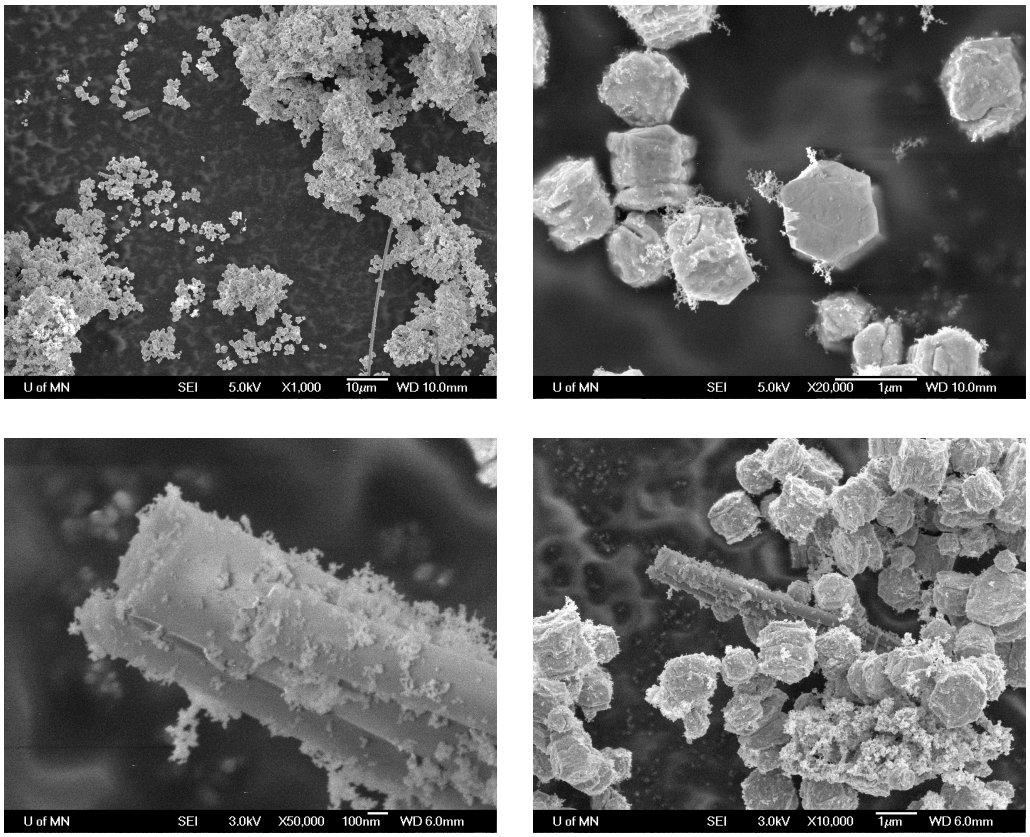

Figure I.6: Additional SEM image #1 from Experiment H ($T_{sat} = 713\,K$ and $y_{H_2O} = 0.12$). The long rod is believed to be fiber from the filter.